# Unlocking Sulfur-Containing Polymers as Cathodes in Room-Temperature Rechargeable Sodium–Sulfur Batteries

Zur Erlangung des akademischen Grades eines

DOKTORS DER NATURWISSENSCHAFTEN
(Dr. rer. nat.)

von der KIT-Fakultät für Chemie und Biowissenschaften
des Karlsruher Instituts für Technologie (KIT)
genehmigte

DISSERTATION

von
M. Sc. Liwen Yang
aus Sichuan, China

KIT-Dekan: Prof. Dr. Martin Bastmeyer

Referent: Prof. Dr. Helmut Ehrenberg

Korreferentin: Prof. Dr. Sonia Dsoke

Tag der mündlichen Prüfung: 21.04.2026

# Contents

# Abbreviation, Constants, Symbols

| | |
|---|---|
| C65 | Conductive carbon super 65 |
| CE | Coulombic efficiency |
| CMC | Sodium Carboxymethyl Cellulose |
| CS | Carbon-sulfur composite |
| CV | Cyclic Voltammetry |
| DOD | Depth of Discharge |
| DSC | Differential Scanning Calorimetry |
| E/S ratio | Electrolyte/sulfur ratio |
| EIS | Electrochemical impedance spectroscopy |
| FT-IR | Fourier-transform infrared spectroscopy |
| GFD | Glass fiber-D |
| LA133 | Aqueous dispersion of acrylonitrile multipolymer |
| Li-S batteries | Lithium-Sulfur batteries |
| NaPS | Sodium polysulfide |
| PAA | Poly(acrylic acid) |
| PVDF | Polyvinylidene fluoride |
| RT Na-S batteries | Room temperature sodium-sulfur batteries |
| S-DIB@NC | A kind of sulfur-containing polymer |
| SEI | Solid Electrolyte Interphase |
| SEM | Scanning Electron Microscope |

| | |
|---|---|
| S@h-p | A kind of sulfur-containing polymer |
| SPAN | Sulfurized polyacrylonitrile |
| S-PAs | Sulfur Rich Polyamide |
| TEGDME | Tetraethylene glycol dimethyl ether |
| TGA | Thermogravimetric analysis |
| XPS | X-ray photoelectron spectroscopy |
| XRD | X-ray Diffraction |

# List of Figures

# List of Tables

# Abstract

Room-temperature sodium-sulfur (RT Na-S) batteries have emerged as a promising energy storage technology capable of meeting the demands of future large-scale energy storage systems, owing to their high theoretical energy density (1274 $Wh \cdot kg^{-1}$), abundant sodium resources, and low cost of raw materials. Nevertheless, the practical deployment of room-temperature sodium–sulfur batteries is hindered by several critical challenges, including the intrinsically low electrical conductivity of sulfur, the dissolution and shuttle effect of sodium polysulfide intermediates during electrochemical reactions, pronounced volume expansion, and irreversible redox processes. These issues collectively lead to poor cycling stability and low coulombic efficiency.

Sulfur-containing polymers are capable of forming stable covalent bonds with sulfur species, thereby enhancing electrochemical performance while maintaining high sulfur loading. This thesis investigates the application of sulfur-containing polymers as cathode materials for sodium–sulfur batteries to overcome the aforementioned challenges. On this basis, the potential applications of novel sulfur-containing polymer that tailored specifically to meet the requirements of Na-S batteries are explored, along with a detailed examination of their underlying electrochemical mechanisms. Furthermore, functionalized separators are employed to further improve the capacity and stability of sulfur-containing polymer cathodes. Sulfurized polyacrylonitrile (SPAN) was used against a Na metal anode to attempt to solve the shuttle effects. SPAN is a structurally stable and highly conductive covalent sulfur polymer. In this polymer, sulfur is embedded in a chain-like form into the carbon nitrogen framework, forming an amorphous and chemically bonded composite cathode material. This structure not only effectively avoids the formation of long-chain polysulfides, thereby suppressing shuttle effects, but also significantly enhances the overall electronic/ion conductivity of the electrode and improves interface reaction kinetics. In addition, SPAN

materials exhibit low volume expansion and good structural reversibility during charge and discharge processes, providing a new approach for achieving high cycling stability. However, the decay mechanism of SPAN positive electrode in ether-based electrolyte RT Na-S batteries remains poorly understood. In this study, sulfurized polyacrylonitrile (SPAN) was applied as a cathode material in ether-based electrolyte, the structural evolution of the SPAN cathode during the first few cycles was explained and the variations in the structure of SPAN and reaction in SPAN//Na cells within different depths of discharge (DOD) was explored. The first part of the results (chapter 5.1) deals with the impact effect of deep discharge below 1.0V on the structure of SPAN, and its impact on the equilibrium of polysulfides in the electrolyte and on the growth of sodium dendrites at the negative electrode. On this basis, to further enhance the cycling stability and rate performance, carbon-coated functionalized separators are incorporated in the cell.

Additionally, a new type of sulfur rich polyamide (**P1**) is used as the positive electrode for sodium sulfur batteries. Rich sulfur polyamide has the dual advantages of high sulfur content and polymer skeleton. On the one hand, the covalently bonded sulfur atoms effectively increase the theoretical capacity and are expected to significantly reduce the shuttle effect caused by the dissolution of polysulfides. On the other hand, the amide groups in the polyamide backbone not only endow the material with excellent structural stability, but are also promising to enhance the synergistic effect of sodium ion and electron conduction. The second part of this work (chapter 5.2) explores the electrochemical performance and working mechanism of **P1** in sodium-metal batteries and explains the irreversible electrochemical behavior of the **P1**. The nucleophilic reaction between polysulfides and active nitrogen in amide groups leads to irreversible bond type conversion from C-N to C-S/S-N/C(=S)-N, resulting in chemical fixation of sulfur and inability of sulfur chains to regenerate during charge process, leading to irreversible loss of active sulfur and low coulombic efficiency. It

provides valuable insights in polymers containing highly active nitrogen sites (amide groups in **P1**) about working and failure mechanism in sodium-metal batteries. On this basis, $MoS_2$ functional separator was used to improve capacity, stability and kinetics by chemical anchoring ability and catalytic activity of molybdenum metal sites.

Inspired by the uniform covalent distribution of sulfur atoms in sulfur-containing polymers that can improve electron conduction pathways and reaction reversibility, solvent method was used for synthesis sulfur-carbon composite material that attempted to combine sulfur and carbon as sulfur-carbon composite, which attempt to design sulfur-carbon composite with uniform sulfur distribution. This method can enhance the interface contact between sulfur and carbon to improve electron/ion transfer efficiency and further improve electrochemical reaction kinetics and cycling stability. Meanwhile, the conductive carbon matrix should provide a robust framework to enhance electronic conductivity and accommodate the volume changes during cycling. Moreover, $MoS_2$ functional separator was applied to cell with CS cathode to improve capacity and stability by molybdenum metal sites, which can inhibit shuttle effects by chemical anchoring ability, and catalytic reaction between sulfur and sodium by catalytic activity. At the same time, the insight of the sodium storage behavior and electrochemical mechanism of the CS cathode is explored by cyclic voltammetry.

These discoveries not only provide new insights into the application of sulfur-containing polymers as positive electrodes for RT Na-S batteries, but also provide new insights into the electrochemical mechanism of these materials in metal batteries (such as Li-metal batteries and K-metal batteries). On this basis, these results provide new solutions to overcome the challenges of RT Na-S batteries.

# Zusammenfassung

Natrium-Schwefel-Batterien (RT-Na-S) bei Raumtemperatur gelten aufgrund ihrer hohen theoretischen Energiedichte (1274 $Wh \cdot kg^{-1}$), der reichlich verfügbaren Natriumressourcen sowie der niedrigen Rohstoffkosten als eine vielversprechende Energiespeichertechnologie, die den Anforderungen zukünftiger großskaliger Energiespeichersysteme gerecht werden kann. Dennoch wird der praktische Einsatz von Natrium-Schwefel-Batterien bei Raumtemperatur durch mehrere entscheidende Herausforderungen eingeschränkt. Dazu gehören die intrinsisch geringe elektrische Leitfähigkeit von Schwefel, die Auflösung und der Shuttle-Effekt von Natriumpolysulfid-Zwischenprodukten während der elektrochemischen Reaktionen, eine ausgeprägte Volumenexpansion sowie irreversible Redoxprozesse. Diese Probleme führen gemeinsam zu einer schlechten Zyklusstabilität und einer niedrigen coulombischen Effizienz.

Schwefelhaltige Polymere sind in der Lage, stabile kovalente Bindungen mit verschiedenen Schwefelarten auszubilden und dadurch die elektrochemische Leistung zu verbessern, während gleichzeitig eine hohe Schwefelladung beibehalten wird. In dieser Dissertation wird der Einsatz solcher schwefelhaltigen Polymere als Kathodenmaterialien für Natrium-Schwefel-Batterien untersucht, um die oben genannten Herausforderungen zu adressieren. Auf dieser Grundlage werden die möglichen Anwendungen neuartiger, speziell auf die Anforderungen von Na-S-Batterien zugeschnittener schwefelhaltiger Polymere sowie eine detaillierte Analyse ihrer zugrunde liegenden elektrochemischen Mechanismen erforscht. Darüber hinaus werden funktionalisierte Separatoren eingesetzt, um die Kapazität und die Stabilität der schwefelhaltigen Polymerkathoden weiter zu verbessern.

Sulfurisiertes Polyacrylonitril (SPAN) wurde in Kombination mit einer Natriummetall-Anode eingesetzt, um den Shuttle-Effekt zu unterdrücken. SPAN ist ein strukturell stabiles und hochleitfähiges kovalentes Schwefelpolymer. In diesem Polymer ist Schwefel in kettenartiger

Form in das Kohlenstoff-Stickstoff-Gerüst eingebettet, wodurch ein amorphes und chemisch gebundenes Verbund-Kathodenmaterial entsteht. Diese Struktur verhindert nicht nur effektiv die Bildung langkettiger Polysulfide und unterdrückt dadurch den Shuttle-Effekt, sondern verbessert auch signifikant die elektronische und ionische Leitfähigkeit der Elektrode sowie die Grenzflächenreaktionskinetik. Darüber hinaus weisen SPAN-Materialien während der Lade- und Entladeprozesse eine geringe Volumenausdehnung und eine gute strukturelle Reversibilität auf, was einen neuen Ansatz zur Erreichung einer hohen Zyklenstabilität bietet. Allerdings ist der Degradationsmechanismus der positiven SPAN- Elektrode in RT-Na-S-Batterien mit etherbasiertem Elektrolyten bislang nur unzureichend verstanden. In dieser Arbeit wurde sulfurisiertes Polyacrylonitril (SPAN) als Kathodenmaterial in einem etherbasierten Elektrolyten eingesetzt. Die strukturelle Evolution der SPAN-Kathode während der ersten Zyklen wurde analysiert, und die strukturellen Veränderungen von SPAN sowie die Reaktionsprozesse in SPAN//Na-Zellen bei unterschiedlichen Entladetiefen (Depth of Discharge, DOD) wurden systematisch untersucht.

Der erste Ergebnisteil der Arbeit (Kapitel 5.1) befasst sich mit den Auswirkungen einer Tiefentladung unterhalb von 1,0 V auf die Struktur von SPAN sowie mit deren Einfluss auf das Polysulfid-Gleichgewicht im Elektrolyten und auf das Wachstum von Natriumdendriten an der negativen Elektrode. Auf dieser Grundlage werden zur weiteren Verbesserung der Zyklenstabilität und der Ratefähigkeit kohlenstoffbeschichtete funktionalisierte Separatoren in die Zelle integriert.

Darüber hinaus wurde ein neuartiges schwefelreiches Polyamid (**P1**) als positives Elektrodenmaterial für Natrium-Schwefel-Batterien eingesetzt. Schwefelreiche Polyamide vereinen die doppelten Vorteile eines hohen Schwefelgehalts und eines polymeren Gerüsts. Einerseits erhöhen die kovalent gebundenen Schwefelatome effektiv die theoretische Kapazität und sollen die durch die Auflösung von Polysulfiden verursachten Shuttle-Effekte

deutlich reduzieren. Andererseits verleihen die Amidgruppen im Polyamid-Rückgrat dem Material nicht nur eine ausgezeichnete strukturelle Stabilität, sondern versprechen auch eine verbesserte synergistische Natriumionen- und Elektronenleitung.

Der zweite Teil dieser Arbeit (Kapitel 5.2) untersucht die elektrochemische Leistungsfähigkeit und den Arbeitsmechanismus von **P1** in Natriummetall-Batterien und erläutert das irreversible elektrochemische Verhalten von **P1**. Die nukleophile Reaktion zwischen Polysulfiden und aktivem Stickstoff in den Amidgruppen führt zu einer irreversiblen Umwandlung der Bindungstypen von C-N zu C-S, S-N bzw. C(=S)-N. Dies resultiert in einer chemischen Fixierung des Schwefels und der Unfähigkeit der Schwefelketten, sich während des Ladevorgangs erneut zu bilden, was zu einem irreversiblen Verlust an aktivem Schwefel und einer niedrigen Coulomb-Effizienz führt.

Diese Ergebnisse liefern wertvolle Erkenntnisse über den Arbeits- und Versagensmechanismus von Polymeren mit hochaktiven Stickstoffzentren (z.B.Amidgruppen in SA33) in Natriummetall-Batterien. Auf dieser Grundlage wurde ein mit $MoS_2$ funktionalisierter Separator eingesetzt, um durch die chemische Ankerfähigkeit und die katalytische Aktivität der Molybdän-Metallzentren Kapazität, Stabilität und Reaktionskinetik weiter zu verbessern.

Inspiriert von der gleichmäßigen kovalenten Verteilung von Schwefelatomen in schwefelhaltigen Polymeren, die zur Verbesserung der Elektronenleitpfade und der Reversibilität elektrochemischer Reaktionen beitragen kann, wurde eine Lösungsmethode zur Synthese eines Schwefel-Kohlenstoff-Verbundmaterials (CS) angewandt. Ziel war es, Schwefel und Kohlenstoff in Form eines Verbundmaterials zu kombinieren und eine homogene Schwefelverteilung innerhalb der Kohlenstoffmatrix zu realisieren. Diese Methode verbessert den Grenzflächenkontakt zwischen Schwefel und Kohlenstoff, erhöht die Effizienz des Elektronen- und Ionentransfers und fördert somit die elektrochemische Reaktionskinetik

sowie die Zyklenstabilität. Gleichzeitig stellt die leitfähige Kohlenstoffmatrix ein robustes Gerüst bereit, das sowohl die elektronische Leitfähigkeit verbessert als auch die Volumenänderungen während des Lade-/Entladeprozesses effektiv puffert.

Darüber hinaus wurde ein mit $MoS_2$ funktionalisierter Separator in Zellen mit CS-Kathode eingesetzt, um Kapazität und Stabilität durch die Molybdän-Metallzentren weiter zu verbessern. Diese können den Shuttle-Effekt durch chemische Ankerwirkung unterdrücken und gleichzeitig durch ihre katalytische Aktivität die Reaktion zwischen Schwefel und Natrium beschleunigen. Parallel dazu wurden das Natriumspeicherverhalten und der elektrochemische Reaktionsmechanismus der CS-Kathode mittels zyklischer Voltammetrie systematisch untersucht.

Diese Ergebnisse liefern nicht nur neue Erkenntnisse für die Anwendung schwefelhaltiger Polymere als positive Elektroden in RT-Na-S-Batterien, sondern eröffnen auch ein vertieftes Verständnis der elektrochemischen Mechanismen dieser Materialien in Metallbatterien (z. B. Lithium-Metall- und Kalium-Metall-Batterien). Auf dieser Grundlage bieten die vorliegenden Resultate neue Lösungsansätze zur Überwindung der zentralen Herausforderungen von RT-Na-S-Batterien.

# Chapter 1 Introduction and Motivation

## 1.1 Background

Nowadays, energy has become an urgent issue at the world level. The next round of high-quality and sustainable global economy is based on the premise of reasonably addressing climate challenges and the correct direction of green energy development. Under the requirements of the times, "carbon neutrality" has become the goal of energy planning. In addition to intermittent energy sources such as wind and solar energy, secondary batteries as a sustainable and stable energy storage system are an inevitable requirement. This will be a necessary condition for advancing the transition from conventional fossil-based energy to renewable energy systems. At present, the mainstream energy storage method is to use lithium-ion batteries. But lithium resources have started to be scarce. According to the International Energy Agency the lithium demand should increase about 40 times by 2040, in order to sustain the expansion of green technologies and keep the global average temperature increase within 1.5 degrees. Therefore, The increase in energy demand and the shortage of lithium resources lead to the requirements for high energy density post-lithium batteries[1]. Room Temperature Sodium-sulfur batteries (RT Na-S batteries) with high capacity (1675 mAh $g^{-1}$) can meet the future energy demand due to the advantages of rich reserves for sodium and sulfur, low cost, and environment-friendliness[2] (Figure 1.1). In this light, RT Na-S batteries are prospective candidates for a new energy storage system in the future.

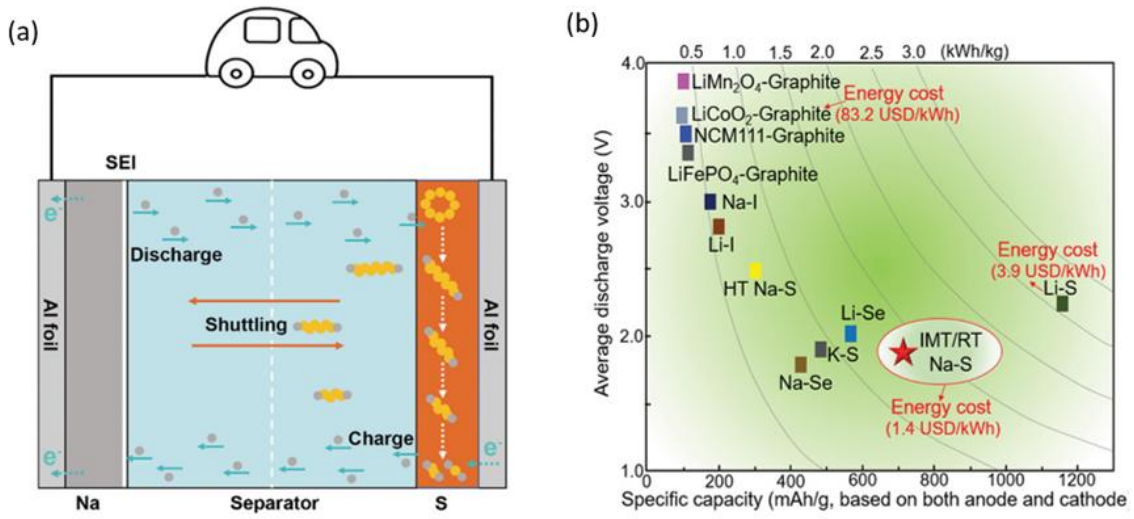


Figure 1.1 (a) Schematic diagram of a typical sodium-sulfur batteries. (b) Energy density and cost comparison of different batteries systems[3].

## 1.2 Mechanisms of Room-Temperature Sodium–Sulfur Batteries

Sodium-sulfur batteries provide energy by the reversible chemical reaction between sulfur and sodium (Reaction 1). It starts from discharge process, in which sodium ions transfer from the negative electrode to the positive electrode to have a multi-step electrochemical reaction with the sulfur to form sodium sulfide ($Na_2S$). Then during the charging process, sodium sulfide is re-oxidized to form sulfur or $Na_2S_8$ (Figure 1.2a)[4].

$$2Na+S \rightarrow Na_2S$$

The composition of polysulfides in Na-S batteries varies at different operating temperatures. Figure 1.2b illustrates the phase diagram of the Na-S system, showing the relationship between temperature and sulfur composition (wt.%). Several phase regions can be observed, including $Na_2S$, $Na_2S_2$, $Na_2S_4$, $Na_2S_5$, and $Na_2S_6$, as well as their coexistence with liquid sulfur or liquid phases at elevated temperatures. At high temperatures (HT region), the system mainly exhibits liquid-phase behavior, where $Na_2S_5$ and sulfur coexist as two liquids

or as a single $Na_2S_5$ phase. In the intermediate-temperature region (IMT), solid-liquid coexistence dominates, such as $Na_2S_4$+ liquid or $Na_2S_3$ + liquid. At room temperature (RT region), multiple solid phases (e.g., $Na_2S$, $Na_2S_2$, $Na_2S_4$, $Na_2S_5$) coexist, indicating limited ionic mobility and sluggish redox kinetics. Given these distinct temperature-dependent phase behaviors, this work specifically focuses on RT Na-S batteries.

As the operating temperature directly influences the phase composition, ion transport, and reaction dynamics within the Na-S batteries, it also determines the type and stability of polysulfide intermediates formed during cycling. In addition to temperature, the nature of the electrolyte plays a crucial role in dictating the reaction pathway, interfacial chemistry, and overall redox reversibility. Depending on the solvation structure and chemical compatibility of the electrolyte, different discharge-charge mechanisms can occur, leading to different polysulfide species and reaction kinetics. In ether-based electrolytes, there are following solid-liquid-solid process during discharge process of RT Na-S batteries:

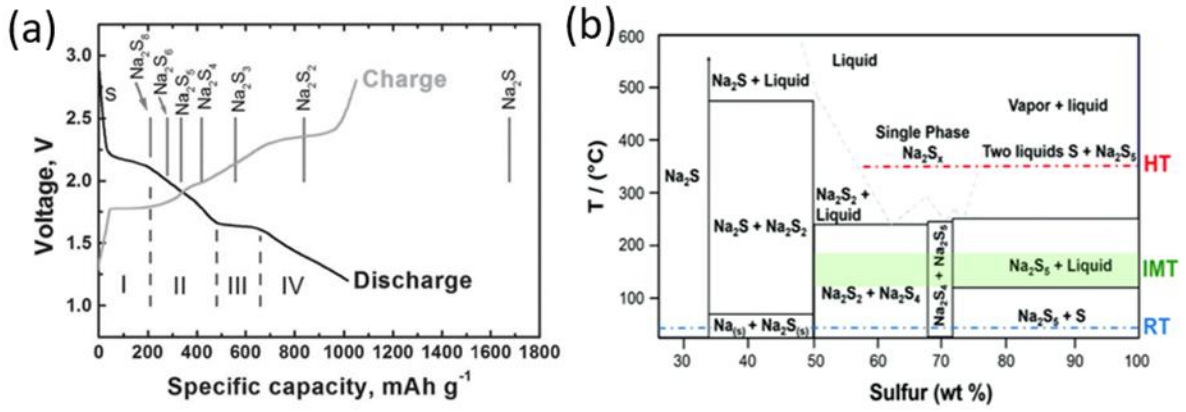


Figure 1.2 (a) Charge-discharge curve of sodium-sulfur batteries, (b) Phase diagram of polysulfide at different temperature[5].

**I: First step (at 2.20V, solid-liquid process).**

Sulfur ($S_8$) undergoes a ring-opening reaction and then reacts with sodium ion to form $Na_2S_8$.

$$S_8+2Na^++2e^-\rightarrow Na_2S_8$$

**II: Second step (between 2.20 and 1.65 V, liquid-liquid process).**

The sulfur chain becomes shorter due to the reduction reaction of $Na_2S_8$ to $Na_2S_4$, also form some $Na_2S_6$ and $Na_2S_5$.

$$Na_2S_8+2Na^++2e^-\rightarrow 2Na_2S_4$$

$$Na_2S_8+2/3Na^++2/3e^-\rightarrow 4/3Na_2S_6$$

$$Na_2S_8+6/5Na^++6/5e^-\rightarrow 8/5Na_2S_5$$

**III: Third step (1.65V, liquid-solid process).**

$Na_2S_4$ reduces to form some insoluble short-chain polysulfide ($Na_2S_3$ and $Na_2S_2$), also form some final product ($Na_2S$) in this process.

$$Na_2S_4 + 2/3Na^+ + 2/3e^- \rightarrow 4/3Na_2S_3$$

$$Na_2S_4 + 2Na^+ + 2e^- \rightarrow 2Na_2S_2$$

$$Na_2S_4 + 6Na^+ + 6e^- \rightarrow 4Na_2S$$

**IV: Fourth step (between 1.65 and 1.20 V, solid-solid process): the short chain polysulfide become $Na_2S$.**

$$Na_2S_2 + 2Na^+ + 2e^- \rightarrow 2Na_2S$$

In carbonate-based electrolyte, the working principle of RT Na-S batteries is really different from ether-based electrolytes. There is no typical multiple-step reaction and no plateau is observed in the discharge-charge curve; instead, there are parasitic reactions between S species and electrolyte solvents, which induce the formation of cathode electrolyte

interphases (CEI). Sulfur undergoes a quasi-solid-state conversions or solid–liquid–solid reactions similar to those in ether-based electrolytes, which will reduce the form of soluble polysulfide. In this case, the charge-discharge curve is a long slope[6]. However, carbonate-based electrolytes are generally unsuitable for RT Na-S batteries due to their intrinsic chemical incompatibility with sulfur species and sodium polysulfides. The strong nucleophilicity of polysulfide anions leads to severe side reactions with carbonate solvents, resulting in electrolyte decomposition and the formation of electrochemically inactive products such as $Na_2CO_3$ and $Na_2SO_3$. These reactions not only consume active sulfur species but also cause the degradation of the electrolyte and electrode interface. In addition, carbonate electrolytes exhibit poor solubility for sodium polysulfides and fail to form a stable solid electrolyte interphase (SEI) on the sodium anode, leading to continuous parasitic reactions and dendrite growth. Consequently, Na-S batteries with carbonate-based electrolytes suffer from rapid capacity fading, low coulombic efficiency, and poor cycling stability, highlighting the necessity of adopting ether-based or alternative stable electrolyte systems.

### 1.3 Challenges of RT Na-S Batteries

**(1) The electronic insulation of sulfur and sodium sulfide.** $S_8$ (active material of positive electrode at initial stage) and $Na_2S$ (electrochemical reduced product of sulfur) are insulators, which significantly hinders the electronic conduction of the positive electrode (cathode)[7].

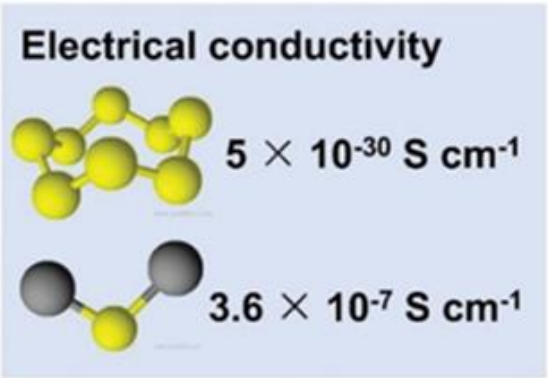


Figure 1.3 Structure and conductivity of sulfur and sodium sulphide.[8]

**(2) Shuttle effect.** Polysulfides are chemical intermediates in the charge discharge reactions of sulfur-metal batteries, which are formed by the combination of sulfur atom chains ($S_x^{2-}$) and metal cations (such as $Na^+$, $K^+$, $Li^+$). Polysulfides have high solubility in various electrolytes, which can dissolve in electrolyte and then shuttle to the metal negative electrode during the charge-discharge process. They can react with metal negative electrodes to form metal sulfide, which has low electrochemical activity and cannot migrate back to positive electrodes during the next cycle. It can lead to sulfur loss, which will cause cell capacity decay, and the partly inactive metal anode will cause dendrite growth. This phenomenon is called the shuttle effect of polysulfides[9]. However, repeated dissolution and deposition of polysulfide can make the surface of the sulfur positive electrode continuously renewed, and the sulfur can gradually fully contact with the electrolyte and conductive matrix as the reaction proceeds to continue to react [10] (Figure 1.4). Therefore, polysulfide needs to be properly regulated as a double-edged sword of sulfur conversion reaction [11].

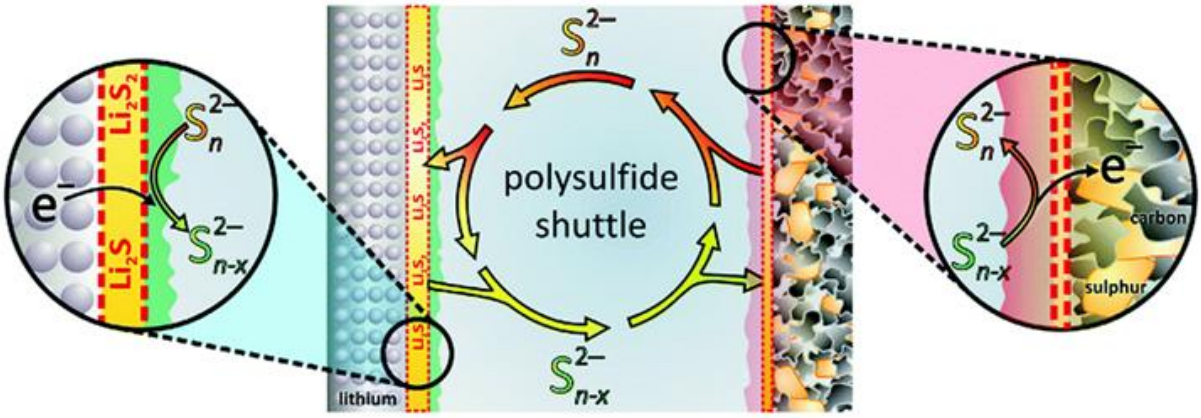


Figure 1.4 Schematic diagram of shuttle effect[12].

**(3) Volume change effect.** The volume expansion occurs due to the density difference of sulfur and sodium sulfide (The density of sodium sulfide is 1.86 g $cm^{-3}$, and the density of sulfur is 2.07 g $cm^{-3}$). A smaller density of sodium sulfide leads to volume expansion during the sulfur electrode converts to sodium sulfide, which may lead to the separation of active material from the current collector and lead to the electrode degradation[13].

**(4) Sodium dendrites growth.** During repeated deposition-stripping, due to the uneven surface current density, there may be a sodium ion concentration gradient difference at the electrode-electrolyte interface, which leads to excessive and irregular deposition of sodium at certain sites to the formation of dendrites. Sodium dendrites can lead to short circuits and safety hazard [14]. In addition, repeated deposition-stripping can cause significant volume changes in metallic sodium, resulting in repeated rupture of the solid electrolyte interphase (SEI). It will lead to the continuous reaction between the active sodium and electrolyte to form dead sodium(Figure 1.5) [15]. In addition, the shuttle effect of polysulfides can cause the surface of metal sodium to be covered by $Na_2S$ to failed with further reaction[16].

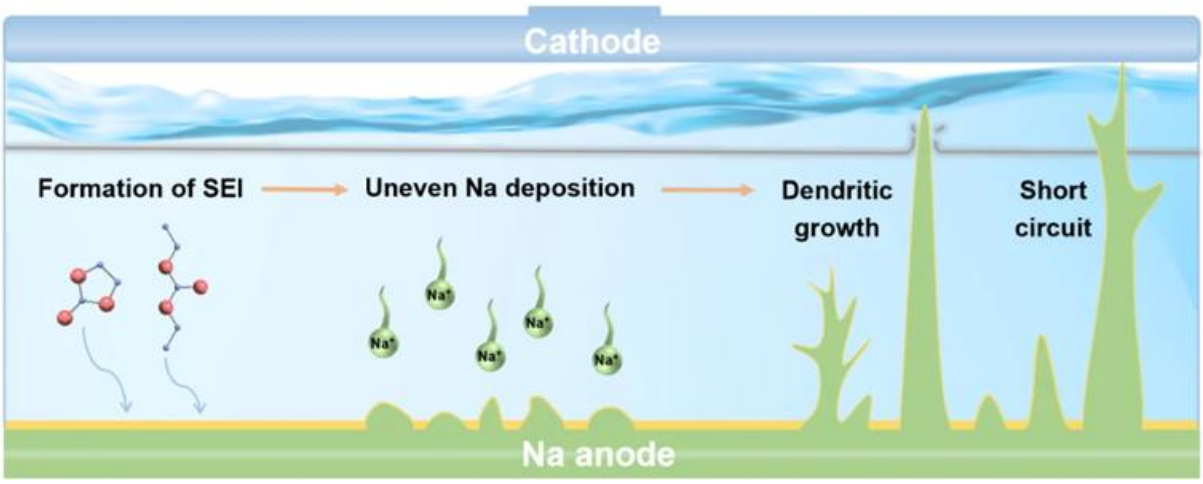


Figure 1.5 Formation mechanism of sodium dendrite[17].

### 1.4 Motivation

Sulfur-containing polymers are promising as positive electrode candidates for RT Na-S batteries due to the following advantages (Figure 1.6):

**(1) Sulfur-sulfur bonds:** sulfur-containing polymers can activate dead sulfur and stabilize active sulfur by forming sulfur-sulfur bonds with polysulfide, subsequently enhance electrochemical kinetics and improve liquid-phase reaction uniformity.

**(2) Stable SEI formation with sodium :** sulfur-containing organics can form stable SEI by reacting with sodium during the electrochemical process (such as free radical polymerization) to build stable electrolyte/sodium negative electrode interfaces[18] .

**(3) Sulfur distribution at a molecular level:** the polysulfide generated in the electrochemical reaction process can be limited at the molecular level by the chemical bond or polymer chain network, which is more stable and effective than the anchoring ability of sulfur hosts to elemental sulfur /polysulfide[19].

**(4) Elastic frames:** The elastic frames of polymers can provide more electrode space than elemental sulfur for the volume expansion in the conversion reaction between sulfur and sodium, thereby alleviating problems such as bad interface contact, charge transfer failure, and active coating detachment caused by volume expansion.

**(5) Network structure:** The network structure can provide high specific surface area and porous channels, which means abundant reaction interfaces, thereby accelerating the redox reaction rate of polysulfides. On this basis, the porous network structure can suppress the migration of sodium polysulfide molecules in the electrolyte through physical confinement, thereby alleviating the shuttle effect. The network structure of conductive polymers can also provide continuous conductive pathways, facilitating rapid electron transfer and improving the electrochemical utilization of sulfur.

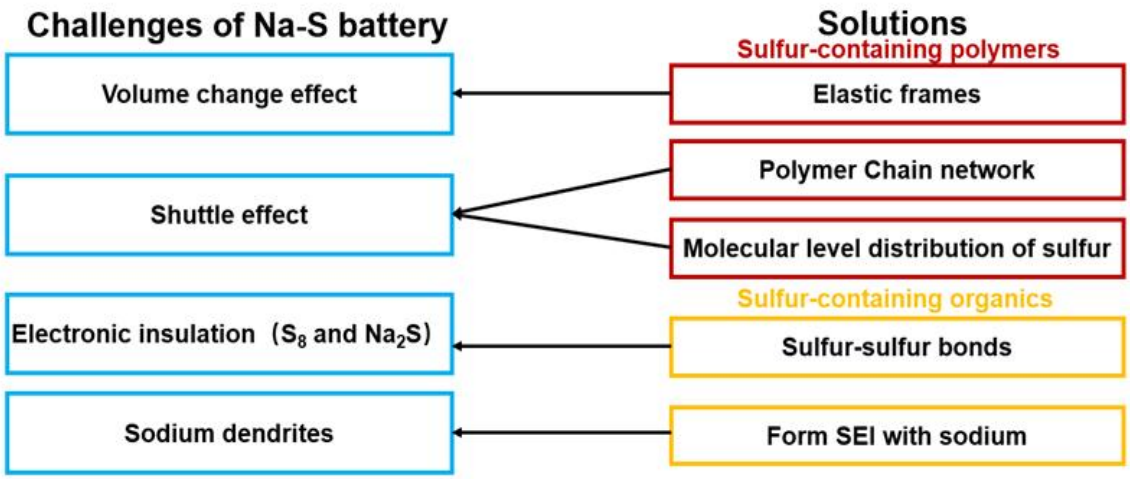


Figure 1.6 Challenge of Sodium-sulfur batteries and how to use sulfur-containing polymer to solve it.

At present, many sulfur-containing polymers have been used as positive electrode of Li-S batteries[20]. Therefore, sulfur-containing polymers have been proved to play a fundamental role in solving the challenges of Li-S batteries. However, there are few studies on sulfur-containing polymers for Na-S batteries. Compared with lithium-sulfur batteries, sodium

sulfur batteries produce sodium polysulfide with higher solubility in the electrolyte, which can diffuse to the sodium metal anode side to cause more severe "shuttle effect" and resulting in stronger capacity fade. Meanwhile, sodium polysulfide is thermodynamically more stable than lithium polysulfide, which leads to slower reaction kinetics. Another key-challenge is the less stable SEI layer and more severe dendrite growth on sodium anode than lithium anode in ether-based electrolytes. The high reactivity between the sodium surface and the electrolyte results in the formation of an SEI of different nature as for the analog lithium SEI. This fragile SEI layer is probe to breakdown, resulting in continues side reactions, sodium dendrites formation, and ultimately a shortened cycle life[21]. Therefore, sulfur-containing polymers for Na-S batteries is urged to be explored. In addition, the reaction mechanism of sulfur containing polymers in sodium systems remains poorly understood, particularly regarding their structural evolution during the initial electrochemical cycles. An understanding of these processes is crucial for the rational design of stable and high-capacity Na-S batteries.

### 1.5 Thesis Overview

This PhD thesis consists of six chapters. Chapter 1 describes the background and motivation of the whole work. Chapter 2 gives a brief information of research status of sulfur-containing polymers as positive electrodes for sulfur-metal batteries. Chapter 3 provides the core research questions and research plan. Chapter 4 introduces the experimental sections such as materials synthesis, materials characterization, and electrochemical measurement. Chapter 5 presents the detailed results, discussion, and conclusions of research. Chapter 6 summarizes the conclusion of this thesis and recommends the strategy for further studies.

# Chapter 2 State of the Art

Research of sulfur-containing polymer in RT Na-S batteries remain relatively limited due to the differences in challenges between Li-S batteries and Na-S batteries, which are caused by different properties of lithium and sodium. Compared with Li-S batteries, Na-S batteries produce sodium polysulfide with higher solubility in the electrolyte, which can diffuse to the sodium metal anode side to cause more severe "shuttle effect" and resulting in stronger capacity fade[22]. Meanwhile, sodium polysulfide is thermodynamically more stable than lithium polysulfide, which leads to slower reaction kinetics[23]. Another key-challenge is the more unstable SEI layer and more severe dendrite growth on sodium anode than lithium anode in ether-based electrolytes[24]. The high reactivity between the sodium surface and the electrolyte results in the formation of an SEI of different nature as for the analog lithium SEI. This fragile SEI layer is probe to breakdown, resulting in continues side reactions, the sodium dendrite formation, and ultimately a shortened cycle life[21]. This not only leads to self-discharge and low coulombic efficiency, but also causes severe capacity fading over time[25]

To address these challenges, insights from the more mature Li-S batteries field are instructive. In Li-S batteries, sulfur-containing polymers have been systematically explored to suppress polysulfide dissolution and stabilize redox reactions. Due to the similar conversion mechanisms of Li-S and Na-S batteries, the design principles and structure-property relationships established in Li-S batteries provide valuable guidance for the development of sulfur-containing polymer cathodes in Na-S batteries. Therefore, this chapter highlights recent advances in sulfur-containing polymers for Li-S batteries, focusing on how different molecular structures govern electrochemical behavior. These understandings can offer inspiration for polymer design strategies to Na-S batteries. In addition, the concept of “functional separators” is briefly introduced in this chapter as a widely applied method to improve capacity and stability.

## 2.1 Sulfur-containing Polymers Positive Electrodes in Lithium-sulfur batteries

Sulfur-containing polymers are composed of polymeric molecular chains and sulfur segments. The number of sulfur atoms in sulfur chain can determine the sulfur content of the polymer and also can come out different electrochemical behavior of polymer. The number of sulfur atoms in sulfur chain can be controlled by amount of the reactants. For lithium-sulfur batteries, there are two typical reaction mechanisms: conventional redox chemistry and solid-phase conversion.

### 2.1.1 Sulfur-containing polymer with conventional redox chemistry mechanism

Sulfur-containing polymers with 6 or more than 6 sulfur atoms in sulfur chain should undergo a similar reaction as elemental sulfur (Figure 2.1) that is considered conventional redox chemistry mechanism.

The electrochemical process can be described as follows: (I) the breaking of sulfur chains within the polymer (solid phase); (II) the reaction of sodium with these sulfur chains to form sodium polysulfides (solid-liquid transition); (III) the progressive shortening of the sulfur chains, leading to the formation of sodium sulfide (liquid-solid transition).

In this case, the charge-discharge profile resembles that of elemental sulfur (Figure 1.2a), exhibiting two distinct voltage plateaus at approximately 2.2 V and 2.0 V.

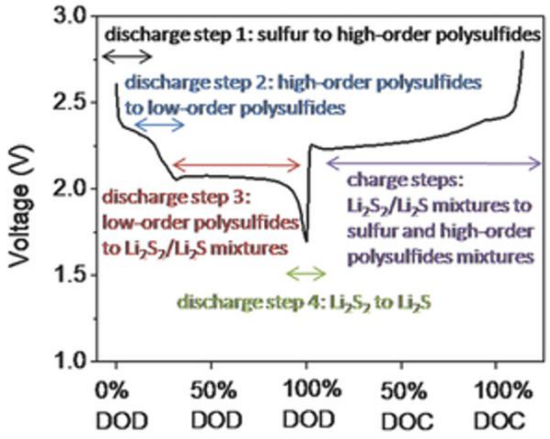


Figure 2.1 Reaction principle of elemental sulfur cathode in lithium sulfur batteries[26].

Upon heating, the cyclic $S_8$ molecules undergo ring-opening to generate diradical sulfur segments, which subsequently copolymerize with unsaturated hydrocarbons. This process produces a highly crosslinked sulfur-organic copolymer with an exceptionally high sulfur content of up to ~95 wt. %. The resulting polymers typically feature sulfur chains containing more than six sulfur atoms, exhibiting electrochemical behavior analogous to that of elemental sulfur. Owing to their robust covalently bonded network structure, these copolymers can effectively anchor polysulfide species and thereby mitigate the shuttle effect during electrochemical cycling.

For example, Chung et al. reported poly(S-r-DIB) as cathode material for Li-S batteries[27]. As shown in Figure 2.2a, poly(S-r-DIB) was synthesized through free-radical copolymerization between 1,3-diisopropenylbenzene (DIB) and diradical sulfur segments at 185 °C. By adjusting the feed ratio of DIB to elemental sulfur, the sulfur content in the resulting copolymer could be precisely tuned from 50 wt.% to 90 wt.%. When employed as a cathode material for Li-S batteries, the copolymer with 90 wt.% sulfur exhibited remarkable electrochemical activity, delivering a reversible capacity of 800 mAh $g^{-1}$ after 100 cycles at 0.1 C (Figure 2.2b). These results indicate that the covalently bonded sulfur-polymer

framework enables both high sulfur utilization and enhanced cycling stability in Li-S batteries.

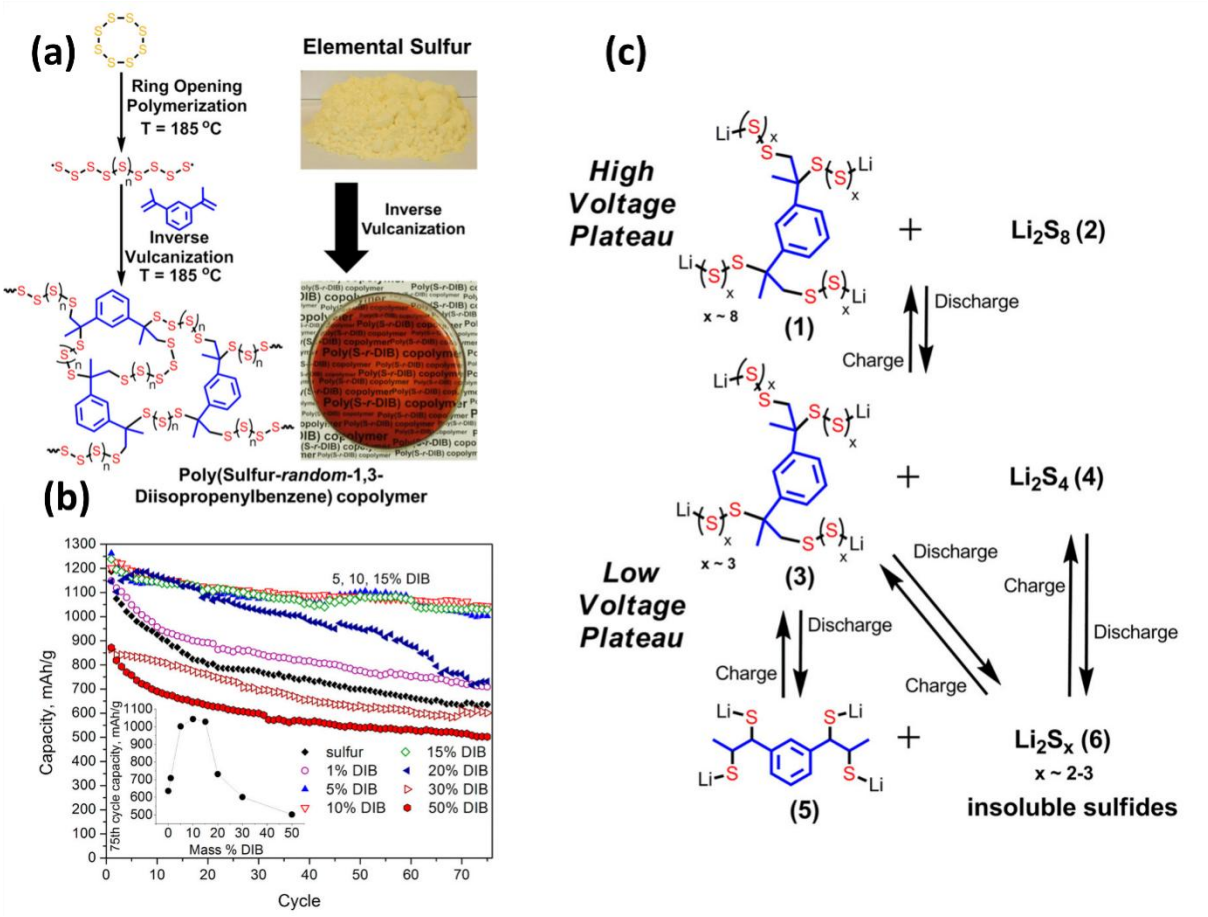


Figure 2.2 (a) Synthesis of poly(S-r-DIB); (b) Cycling performance of sulfur copolymers of varying composition (0–50% by mass DIB); (c) Proposed electrochemisty of poly(S-r-DIB) copolymers in Li–S batteries[27].

Building on these insights, first-principles calculations have been utilized to guide the rational design of sulfur-containing polymer cathodes. Specifically, vinyl-functionalized polymers have been shown to strengthen sulfur-polymer crosslinking, thereby enhancing structural stability during electrochemical cycling. Moreover, incorporating such polymers with conductive frameworks can simultaneously improve electron transport, increase capacity, and promote superior kinetic stability[28].

According to first-principles calculations, aromatic and vinyl groups are often employed to achieve high conductivity and structural robustness in polymer cathodes. Interestingly, azulene has been identified as a promising building block for designing benzene-free and vinyl-free sulfur-containing functional polymers. Azulene is a non-alternant aromatic hydrocarbon consisting of an electron-rich five-membered ring fused with an electron-deficient seven-membered ring, endowing it with a unique electronic structure and a large dipole moment of 1.08 D (Figure 2.3a). The copolymerization of sulfur and azulene was achieved by direct heating at 185 °C under a nitrogen atmosphere. In this process, molten sulfur containing abundant sulfur diradicals reacts with azulene without any additional initiator, forming a black solid product after purification with $CS_2$ and ethanol at room temperature. When employed as the cathode material in Li-S batteries, the resulting azulene-sulfur copolymer delivered an initial discharge capacity of 1036 mAh $g^{-1}$ at 0.3 C and retained 515 mAh $g^{-1}$ after 100 cycles (Figure 2.3b)[29].

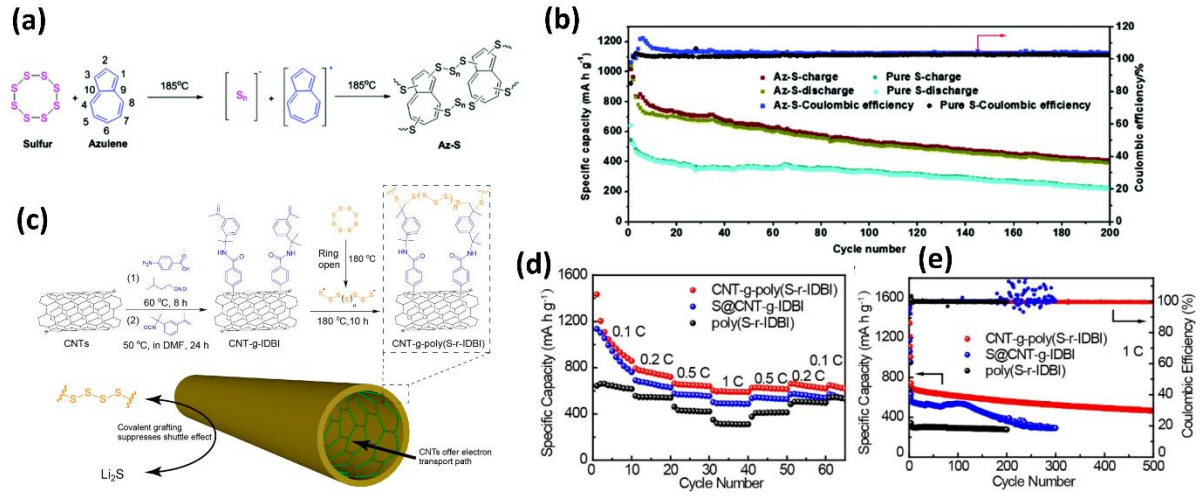


Figure 2.3 (a) Synthesis of azulene-sulfur cathode; (b) Cycling performance of azulene-sulfur cathode[29]; (c) Synthesis and working principle of CNT-g-poly(S-r-IDBI) cathode; (d) Rate performance and (e) Cycling performance of CNT-g-poly(S-r-IDBI) cathode[30].

Moreover, carbon materials can also be introduced into polymers to increase conductivity. Geng et al. used sulfur to react with carbon nanotubes (CNTs) that are functionalized with isopropenyl groups to come out the CNT-g-poly(S-r-IDBI). This material retains the one-dimensional structure of carbon nanotubes (CNTs), which enhances electron transport and facilitates the formation of a porous interwoven network that effectively accommodates the volume change during cycling (Figure 2.3c). The CNT-g-poly(S-r-DIB) composite provides an excellent initial capacity of 1368 mAh $g^{-1}$ at 0.05 C and outstanding cycling stability, with a low-capacity decay rate of 0.074% per cycle at 1 C over 500 cycles. Moreover, electrochemical impedance spectroscopy (EIS) confirms the high ionic conductivity of the composite, which originates from the covalent bonding between CNTs and sulfur-containing polymer chains.[30]. Such covalent coupling strengthens the interfacial interactions between the cathode material and the electrolyte.

In addition to improving the electrical conductivity of sulfur-containing polymers through carbon-based composites, enhancing the intrinsic safety of Na–S batteries is equally critical. One of the major safety challenges in sodium-based systems stems from the high reactivity of metallic sodium and the flammability of conventional organic electrolytes. Therefore, the incorporation of flame-retardant polymers represents a promising strategy to enhance the thermal stability and overall safety of polymer–sulfur cathodes, while maintaining favorable electrochemical performance.

To this end, polyphosphate-based materials have been explored as flame-retardant components for the design of safe sulfur cathodes. Polyphosphates can react with elemental sulfur via inverse vulcanization to form covalently bonded sulfur-containing polymers. Rezan Demir-Cakan et al.synthesized a series of polymers by reacting poly[bis(2-acrylamidoethoxy)phosphazene] (poly(AAE)) with sulfur, obtaining materials with varying

sulfur contents. The incorporation of polyphosphate not only enhances the thermal safety of the cathode but also provides abundant polar amide groups capable of strongly anchoring polysulfides (Figure 2.4a). Among these materials, the poly (AAE)-55S copolymer, containing 55 wt. % sulfur, exhibited the best electrochemical performance, as higher sulfur contents (80–90 wt.%) led to reduced electrical conductivity. When employed as the cathode material in Li-S batteries, poly(AAE)-55S delivered an initial capacity of 1181 mAh $g^{-1}$ at 0.5 C and maintained excellent stability over 200 cycles at 0.2 C (Figure 2.4b and c)[31]. Furthermore, poly(S-r-p) was synthesized via inverse vulcanization of elemental sulfur with

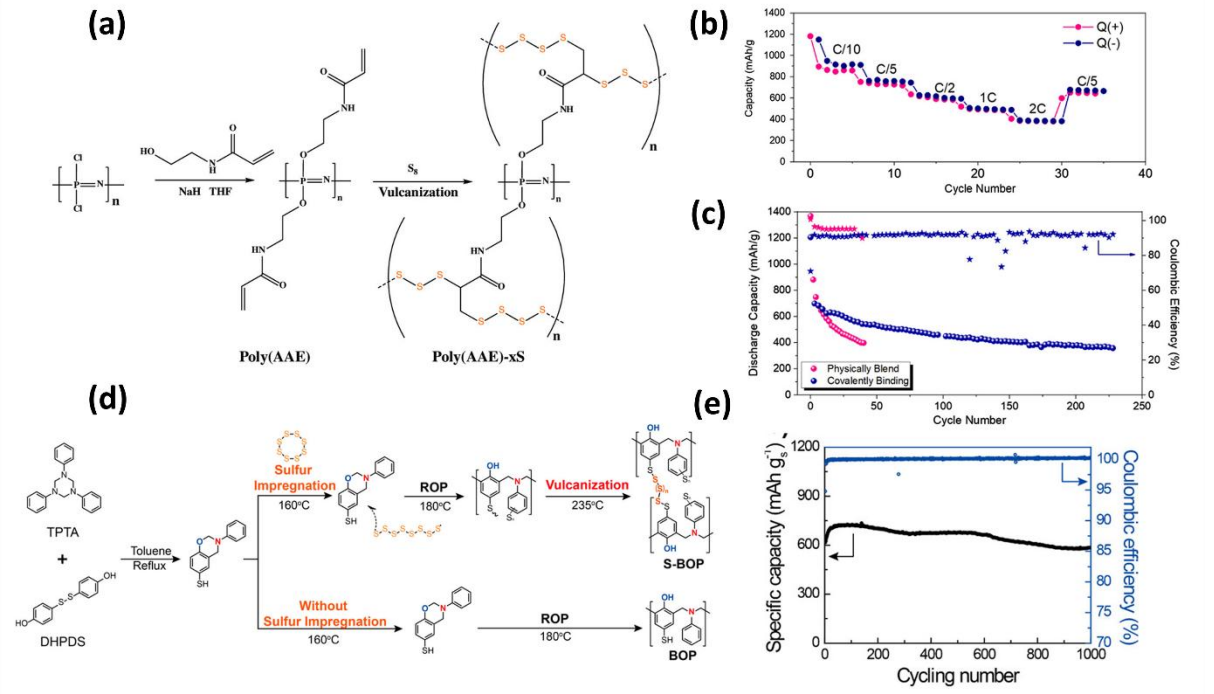


Figure 2.4 (a) Synthesis of poly (AAE); (b) Rate performance and (c) Cycling performance of poly (AAE) in lithium-sulfur cell; (d) Synthesis of S-BOP; (e) Cycling performance of S-BOP in lithium sulfur cell.

hexakis(styreneoxy)cyclotriphosphazene. Benefiting from its robust crosslinked network, the poly(S-r-p) cathode exhibited stable cycling for over 100 cycles at 0.2 C, whereas the conventional sulfur cathode suffered from severe capacity decay after approximately 20 cycles.[32].

Jang Wook Choi et al. developed an orthogonal “one-pot” synthetic strategy to prepare sulfur-embedded polybenzoxazine (S-BOP) with a high sulfur content of 72 wt.%. In this approach, sulfur is incorporated into the polymer framework through a vulcanization reaction involving the thiol functionality of benzoxazine (Figure 2.4d). This unique internal structure endows S-BOP with an exceptionally high initial coulombic efficiency (ICE) of 96.5% and outstanding cycling stability, retaining 92.7% of its capacity after 1000 cycles when employed as a sulfur cathode[33] (Figure 2.4e).

Covalent triazine framework (CTF) is a type of high conductivity microporous polymer with narrow distributed pore size and high specific surface[34]. CTFs incorporated with sulfur exhibit high sulfur content and have emerged as promising cathode materials for lithium-sulfur and sodium-sulfur batteries. To date, a variety of monomers (e.g., 1,4-dicyanobenzene[35], perfluorinated aromatic nitrile[36], 2,2′((perfluoro-1,4-phenylene) bis(methanyl-ylidene)) dimalononitrile[37]) have been utilized to copolymerize with sulfur, forming sulfur-CTF (S-CTF) copolymers. The S-CTF frameworks offer strong chemical binding to effectively suppress the polysulfide shuttle effect, while their porous structure provides sufficient space to accommodate the volume expansion during cycling. Furthermore, the uniformly distributed sulfur species and the good electronic/ionic conductivity of S-CTF enable a stable discharge capacity of approximately 500 mAh $g^{-1}$ over 50 cycles.

The sulfur content of S-CTF can be further increased by introducing electron-withdrawing substituents to functionalize the aromatic monomers, thereby enhancing their electron deficiency and promoting the nucleophilic addition of sulfur chains[38]. As shown in Figure 2.5a, perfluorinated aryl cyanide was employed as the monomer to synthesize sulfur-containing CTFs with a high sulfur loading of 86 wt.%. The fluorine substituents create abundant active sites for sulfur species, facilitating strong covalent interactions. Consequently,

the resulting polymer exhibits a stable capacity of 500 mAh $g^{-1}$ at 1 A $g^{-1}$, attributed to the highly reversible S-S and C-S bond transformations during cycling (Figure 2.5b).

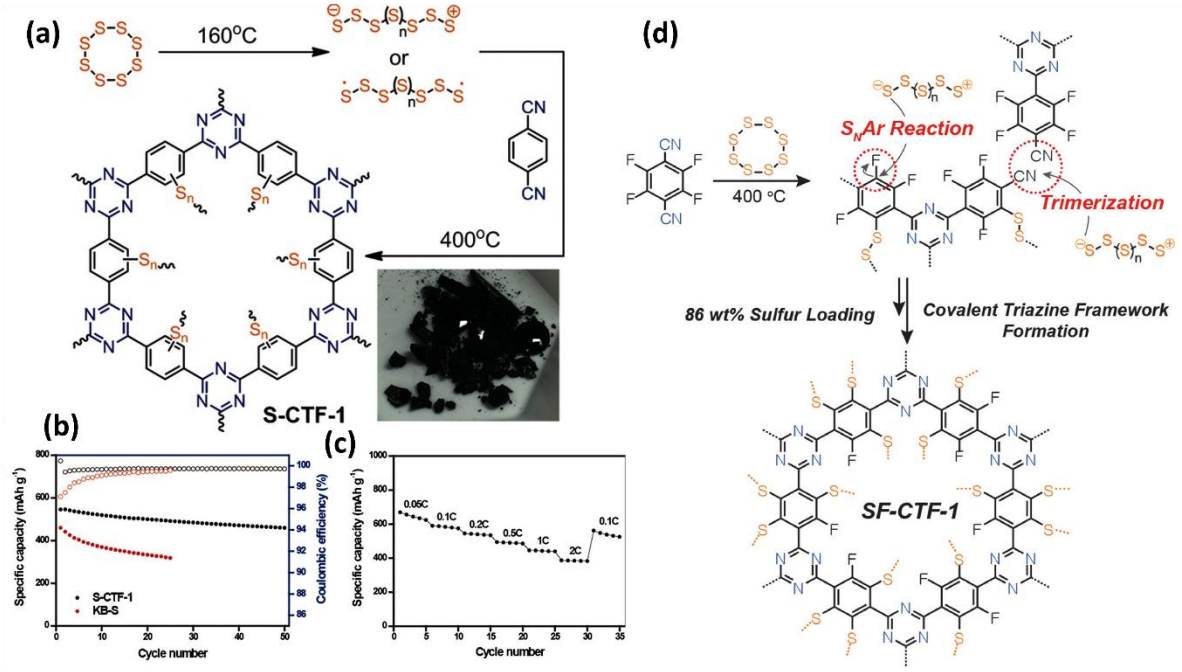


Figure 2.5 (a) Synthesis and structure of S-CTF; (b) Cycling performance and (c) Rate performance of S-CTF; (d) Synthesis scheme of sulfur-CTF copolymer from elemental sulfur and perfluorinated aryl cyanides.

### 2.1.2 Sulfur-containing polymer with solid-phase conversion mechanism

**Solid-solid phase reaction mechanism**

Sulfur-containing polymers with short sulfur chains (four or fewer sulfur atoms) undergo a solid-solid conversion reaction with alkali metals, forming solid $Li_2S_4$/$Na_2S_4$ intermediates instead of soluble lithium/sodium polysulfides, and ultimately converting to $Li_2S$ or $Na_2S$. The entire electrochemical process proceeds within the solid phase. During the initial discharge, these polymers experience an activation process at higher voltages, leading to the formation of a cathode–electrolyte interphase (CEI) layer on the sulfur surface. Consequently, the discharge profile exhibits a sloping curve between 2.2 and 1.5 V without a distinct plateau.

Doping or modifying the polymer with chalcogen elements (from the same group as sulfur) can lower the bond dissociation energy, thereby facilitating the formation of short-chain polysulfides and suppressing the dissolution of long-chain species in the electrolyte. As illustrated in Figure 2.6a, a selenium-doped polymer (PDATtSSe) containing four sulfur atoms and one selenium atom was designed[39]. The Se-S bonds possess lower binding energy than S-S bonds, allowing them to break more readily during electrochemical cycling and promote the generation of short-chain polysulfides, which effectively mitigate the shuttle effect. Moreover, selenium contributes additional capacity due to its electrochemical activity. In addition, the unique molecular configuration of PDATtSSe enables a solid-solid

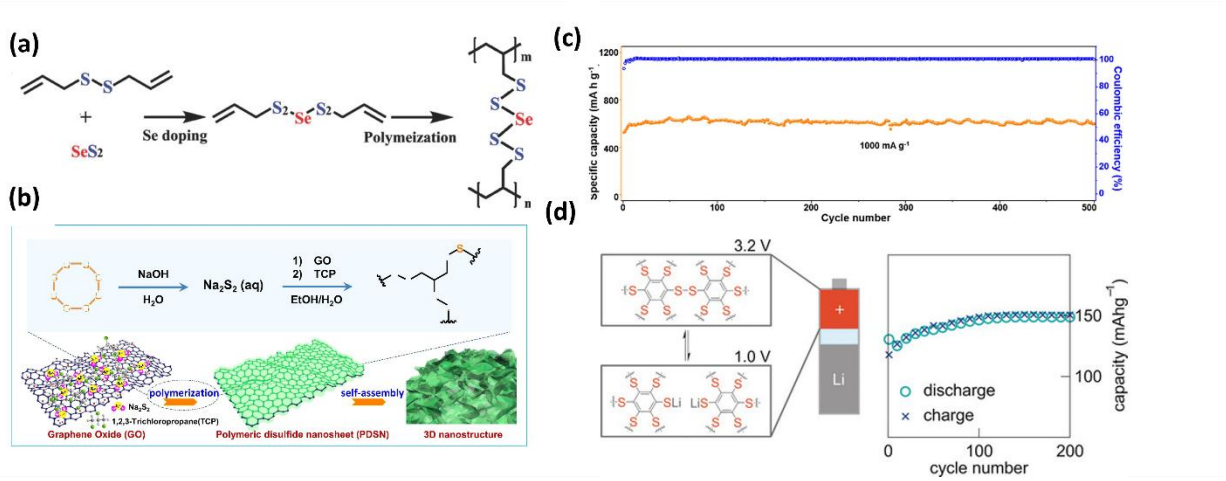


Figure 2.6 (a) Synthesis of PDATtSSe[38]; (b) Synthesis of polymer by interfacial polymerization and self-assembly with graphene, (c) Cycling performance of polymer by interfacial polymerization and self-assembly with graphene[39], (d) Structure and cycling performance of $C_6S_6$[40].

conversion mechanism throughout the reaction. As a result, Li-S cells employing PDATtSSe cathodes deliver a high specific capacity of 700 mAh $g^{-1}$, approaching the theoretical value, and exhibit excellent cycling stability with 92% capacity retention after 400 cycles.

Furthermore, to address the inherently low electrical conductivity of sulfur, a sulfur–polyacrylonitrile composite (S@pPAN) with a sulfur content of 41 wt.% was designed as the

cathode material for Li-S batteries. In S@pPAN, each sulfur atom is covalently bonded to the carbon atoms adjacent to nitrogen within the polymer backbone[40]. During lithiation, $Li^+$ ions coordinate with negatively charged sites in the conjugated framework through a lithium-coupled electron transfer process, resulting in enhanced electrochemical performance. Additionally, surface carbonyl (C=O) groups can react with dissolved polysulfides in the ester-based electrolyte to form a stable cathode-electrolyte interphase (CEI), effectively suppressing polysulfide dissolution and mitigating the shuttle effect. Moreover, the heterocyclic structure of pPAN provides well-organized electronic pathways at the molecular level, thereby reducing polarization during electrochemical cycling[41].

Graphene oxide (GO), characterized by its high charge-transport capability and three-dimensional porous architecture, further facilitates ion diffusion and electron conduction. Qiang et al. developed a polymer-graphene composite via interfacial polymerization and self-assembly, enabling abundant active sites for lithium adsorption and redox reactions (Figure 2.6b). Owing to the synergistic effect of conductive graphene and active polymer chains, the composite cathode exhibited an initial discharge capacity of 805 mAh $g^{-1}$ and maintained 600 mAh $g^{-1}$ at 1000 mA $g^{-1}$ after 500 cycles (Figure 2.6c)[42].

In summary, the solid- solid phase conversion can be designed by using different sulfur content during synthesis to adjust the number of sulfur atom in sulfur chain. The short sulfur chain leads to the less step of electrochemical reaction, which leads to low amount of polysulfide to inhibit the shuttle effect. Preefer et al. [43]designed a kind of crosslink disulfide cathode in lithium sulfur batteries that has six carbon atoms and six sulfur atoms ($C_6S_6$), which can bond with six lithium ions during the reaction (Figure 2.6d). The process of electrochemical reaction was explored by Raman spectrum, the signal of S-S bond was decrease while the signal of Li-S bond was increase during discharge to show the lithium ion

was react with the disulfide bond in crosslink of polymer in $C_6S_6$ [43]. Due to the such stable network, $C_6S_6$ can provide 150 mAh $g^{-1}$ capacity during 200 cycles. It is worth noting that the capacity of this polymer is significantly lower than other polymers mentioned below. It is indicating that although short sulfur chains effectively prevent the formation of long-chain polysulfides and thereby suppress the shuttle effect, this structural advantage comes at the cost of reduced capacity, as the limited sulfur-chain length restricts the number of electrons that can participate in the redox process.

In addition, sulfur chains of different lengths not only exhibit distinct electrochemical reaction mechanisms but also result in different specific capacities. Gomez et al. investigated the correlation between sulfur chain length and electrochemical capacity using a series of poly(anthraquinonyl sulfide) (PAQS)-based polymers with varying sulfur chain lengths [44]. As shown in Figure 2.7, the Li-storage mechanisms differ significantly depending on the sulfur chain length. Polymers containing long sulfur chains deliver higher specific capacities due to the formation of soluble polysulfide intermediates; however, they suffer from poor cycling stability as a result of the polysulfide shuttle effect. In contrast, short sulfur chain polymers exhibit more stable electrochemical behavior without the generation of soluble polysulfides, but their capacities are limited because of the absence of sulfur-polysulfide redox conversion. Therefore, achieving an optimal balance between sulfur chain length and capacity is crucial. Rational molecular design-particularly through functional crosslinking-offers an effective strategy to realize high-capacity and stability.

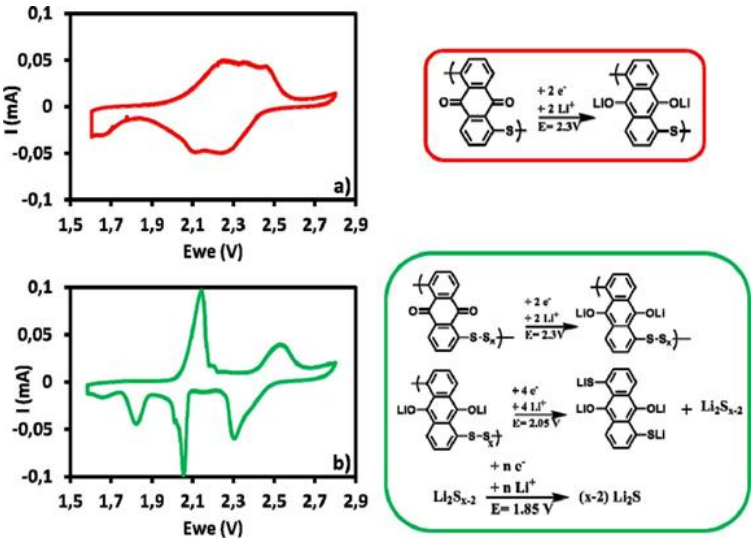


Figure 2.7 Li storage mechanism of PAQS with different length of sulfur[44].

### 2.1.3 Quasi solid–solid reaction mechanism

Sulfur-containing polymers with sulfur chain lengths between four and six atoms can generate low-order polysulfide intermediates during the discharge process. This behavior is typically reflected in the cyclic voltammetry (CV) profile as several reduction peaks appearing between 2.0 and 2.3 V. However, in the corresponding discharge curve, these multiple redox processes overlap, resulting in a single broad discharge plateau.

Polyphenylene tetrasulfide (PPTS) is a kind of polymer with four S atoms in one monomer that is synthesized by utilizing 1, 4-benzenedithiol and elemental sulfur via condensation reaction (Figure 2.8a and Figure 2.8b). PPTS has high theoretical capacity in Li-metal cells (1217 mAh $g^{-1}$) and excellent mechanical ductility, which shows stretch rate high as 334%. PPTS shows small reaction peaks at 2.24, 2.2, 2.06 and 1.97 V, which lead to the multi-step reduction at low rates cycle (C/20) (Figure 2.8c)[45].

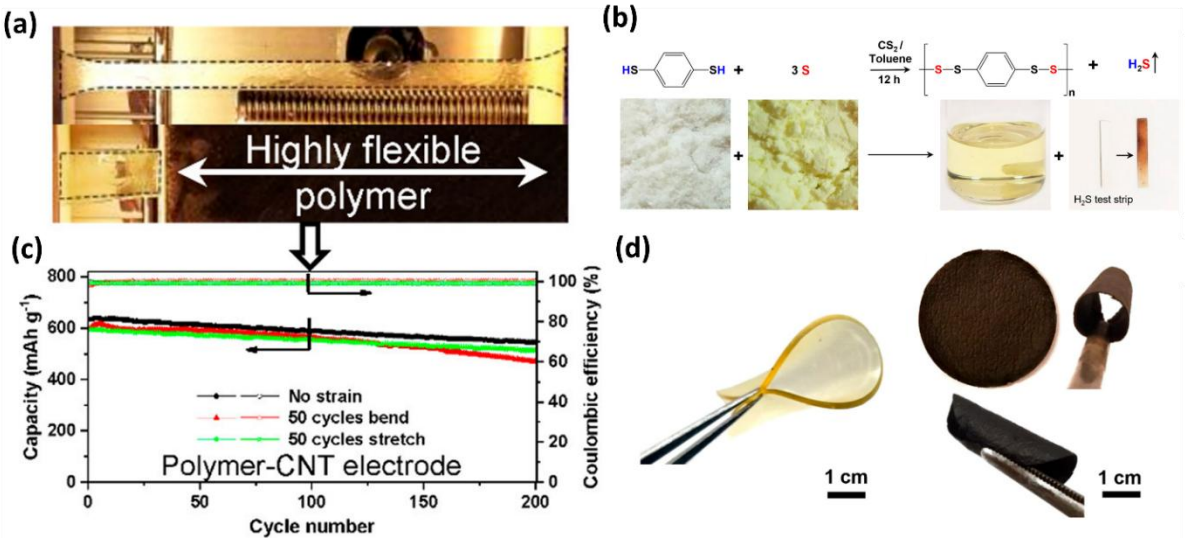


Figure 2.8 (a)High flexible of PPTS; (b) Synthesis of PPTS; (c) Cycling performance of PPTS; (d) Optical images of the PPTS-CNT cathode membrane showing its flexible nature.

### 2.1.4 Solid–solid reaction mechanism under particular conditions

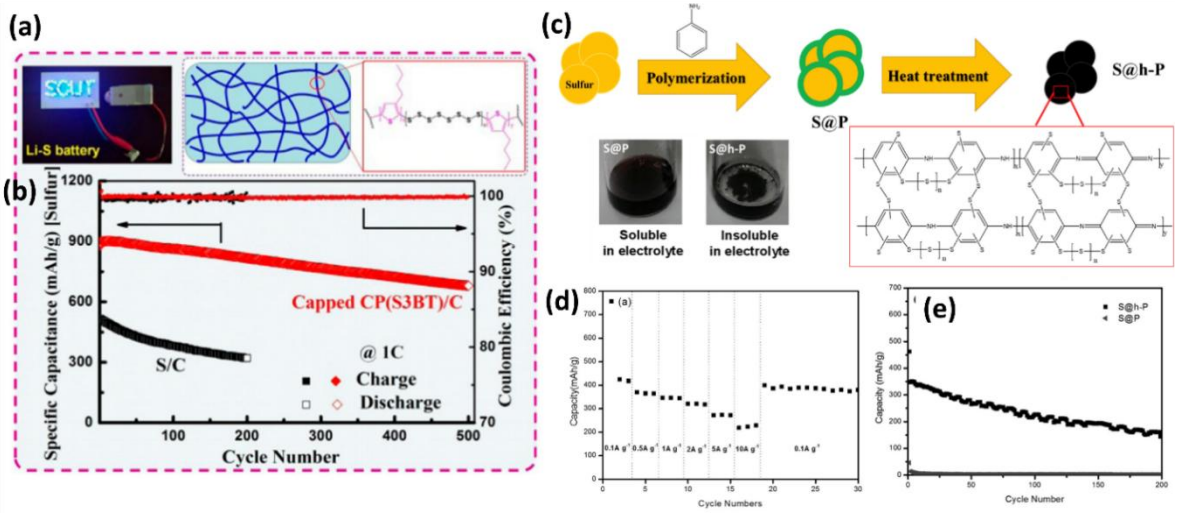


Figure 2.9 (a) Structure of CP(S3BT); (b) Cycling performance of CP(S3BT); (c) Synthesis and structure of S@h-p; (d) Rate performance and (e) cycling performance of S@h-p.

Under certain conditions, the electrochemical reaction may proceed via a solid-solid mechanism even when the sulfur chains contain more than six sulfur atoms. This phenomenon can be attributed to structural changes during cycling or the gradual detachment

of sulfur atoms from the polymer backbone, which shortens the sulfur chains and alters their electrochemical behavior. Such behavior may also occur in systems with specific functional layers. For example, 3-butylthiophene can copolymerize with sulfur upon heating to form a crosslinked copolymer (CP($S_3$BT)). The conjugated structure in 3-butylthiophene can provide high conductivity, which is really helpful for the electrochemical kinetics (Figure 2.9a)[46]. With the PEDOT: PSS capping layer, the CP(S3BT) cathode can achieve initial discharge capacity of 1362 mA h $g^{-1}$ at 0.1 C and a reversible capacity of 631 mA h $g^{-1}$ even at 5 C, the PEDOT: PSS layer not only can provide additional capacity, but also can act as a functional layer for anchoring polysulfide on the positive side to only show one platform in discharge curve. In addition, CP(S3BT) cathode showed a capacity of 682 mA h $g^{-1}$ even after 500 cycles at 1C, while the S/C electrode can only provide 321 mA h $g^{-1}$ after only 200 cycles (Figure 2.9b).

Moreover, polyaniline (PANI) is a highly conductive polymer that can serve as an effective matrix for sulfur incorporation. During synthesis, the PANI backbone can undergo partial bond cleavage, allowing carbon atoms to be replaced by sulfur atoms to form new covalent bonds, thereby generating a sulfur-containing polymer with enhanced electrical conductivity (Figure 2.9c). The unique network structure of PANI not only suppresses the polysulfide shuttle effect but also provides efficient electron and ion transport pathways, leading to excellent battery performance. The S@h-p cathode is obtained by heat-treating the S@P precursor at 300 °C. Owing to the short sulfur chains and the crosslinked polymer framework, S@h-p undergoes a solid–solid conversion process and exhibits an additional reduction peak at approximately 1.65 V, corresponding to the reduction of $S_2^{2-}$ to $2S^{2-}$[47].

## 2.2 Polymer/carbon composites in Sodium-Sulfur batteries

Sodium–sulfur (Na-S) batteries generally exhibit slower reaction kinetics and more pronounced side reactions compared to lithium-sulfur (Li-S) batteries. Consequently, many polymer cathodes effective in Li-S systems fail to operate properly in Na-S cells. In particular, polymers synthesized via inverse vulcanization can react with metallic sodium, leading to "under-voltage failure" (a condition where the cell cannot reach the designed cut-off voltage) along with severe polarization and reduced capacity (Figure 2.10).

To address this issue, Zou et al. employed nitrogen-doped carbon (NC) as a conductive host for sulfur–DIB copolymers, forming the S-DIB@NC composite[48]. The porous NC framework provides physical confinement to suppress polysulfide diffusion and effectively prevents direct reactions between the polymer and sodium metal. Simultaneously, covalent confinement through C-S bonds further mitigate the shuttle effect. As a result, Na-S cell with S-DIB@NC cathodes provide a high reversible capacity of 795.1 mAh $g^{-1}$ at 0.1 A $g^{-1}$ and maintain 457 mAh $g^{-1}$ after 1300 cycles, demonstrating outstanding long-term stability.

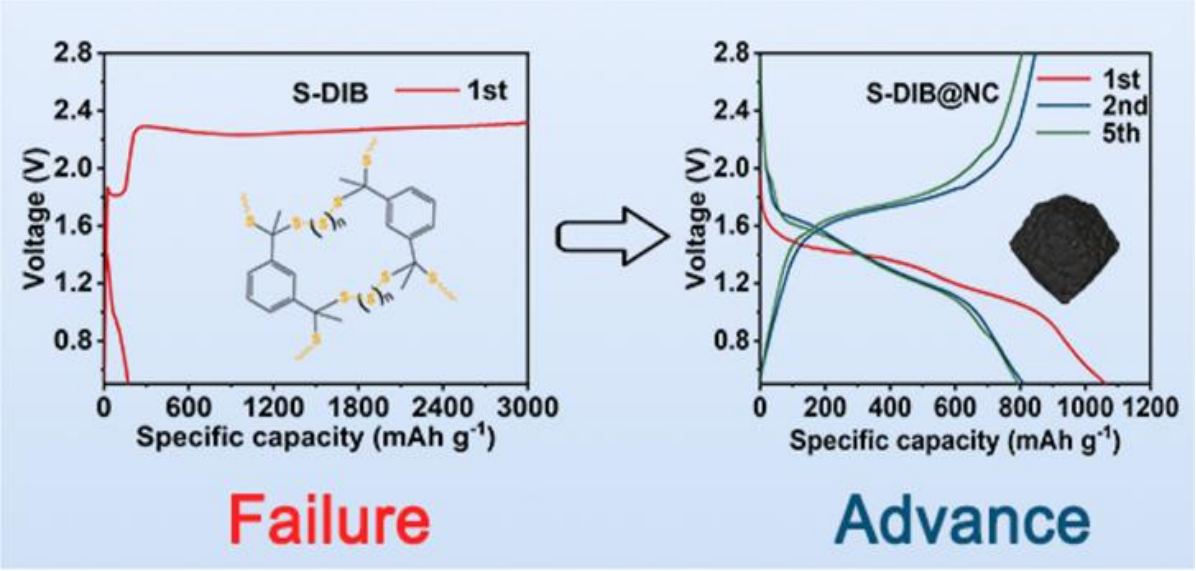


Figure 2.10 Compare between S-DIB and S-DIB@NC in sodium-sulfur cell.

### 2.3 Application of Functional separator in Lithium/Sodium-sulfur batteries

In lithium/sodium-sulfur batteries, much work was focused on positive electrode materials[49], [50], [51], [52]. With the development of research, the understanding of polysulfides is becoming increasingly profound. Polysulfides is a double-edged sword: the dissolution of polysulfide can expose internally sulfur to react and let sulfur and polysulfide redistributed evenly on the electrode[10]. In addition, the dissolution and diffusion of polysulfides are thermodynamically advantageous so it cannot be completely suppressed. Therefore, functional separators can effectively hinder between polysulfide and anode and to build a stable interface[11]. The functional interface can promote the transport of electrons and act as catalyst of electrochemical reaction. Separator as an indispensable component of the cell can directly contact the positive and negative electrode and effectively regulate the external environment by functional materials on separator.

Functional materials that have been proven effective in the cathode of lithium-sulfur batteries can be applied to functional separators, such as multidimensional carbon materials and metallization compounds, etc. Various carbon materials have been used for separator functional layers, such as CNT[53], GO[54] and rGO[55], which can construct three-dimensional (3D) networks to hinder polysulfide, and by doping nitrogen to chemical anchor polysulfide[56].

Metal single atoms/compounds with metal sites and anions can effectively adsorb polysulfide and catalyze the sulfur-lithium reactions, which can effectively promote internal dynamics, achieving excellent rate and long cycle performance[57].

In addition, some organic materials with polar functional groups can be used in separators, such as metal organic frameworks (MOFs), covalent organic frameworks (COFs), and organic polymers. Among them, the metal organic framework is composed of metal ions/metal clusters coordinated and bridged with organic ligands, which has extremely

attractive characteristics as a porous crystalline material. MOFs have highly adjustable pore structure and morphology and designed polar, functional groups, such as carbonyl (C=O), hydroxyl (-OH), amine (-$NH_2$), amide (-CONH-), nitrile (-C≡N), sulfonic (-$SO_3H$), and ether (-O-) possess strong polarity or electron-donating/withdrawing capabilities, enabling them to form dipole-ion interactions or even covalent bonds with polysulfide species. In particular, carbonyl and amide groups can coordinate with $Li^+$, while amine and hydroxyl groups can form hydrogen bonds with terminal sulfur atoms ($S_n^{2-}$), effectively immobilizing polysulfides and reducing their diffusion across the separator. Moreover, MOFs can provide considerable specific surface area and uniformly distributed metal sites, which shows promising candidates for functionalization materials in lithium sulfur batteries.

For example, UiO-66-SO3Li is used to prepare mixed matrix membranes (MMMs) to improve the electrochemical performance of lithium sulfur batteries. This material has anion channels of appropriate size (<6 Å), which can provide physical barriers and electrostatic repulsion to polysulfides. At the same time, these regularly arranged anion channels can also guide the uniform deposition of lithium ions and inhibit the growth of lithium dendrites[58] . This study highlights the effective confinement capability of metal-organic frameworks (MOFs) with tailored pore sizes for trapping polysulfides. However, significant interfacial and grain-boundary challenges arise during the fabrication of MOF-based membranes. The inherent incompatibility between inorganic MOF particles and organic polymer matrices often leads to uneven particle dispersion and the formation of large interfacial voids, which inevitably create non-selective permeation pathways.

In order to minimize the intrinsic defects, the researchers selected MOFs with proper pore size through theoretical calculation and then used the sol-gel process to prepare self-supporting MOF gel membrane without matrix or adhesive. This preparation strategy combines the high permeability and selectivity of main MOF particles with the density and

integrity of dry gel, which can introduce the least non-selective defects and effectively block polysulfides from going to the negative electrode. This study underscores the strong confinement capability of metal–organic frameworks (MOFs) with precisely tailored pore sizes for trapping polysulfides. Nevertheless, the fabrication of MOF-based membranes still faces significant interfacial and grain-boundary challenges. The intrinsic incompatibility between inorganic MOF particles and organic polymer matrices often results in nonuniform particle dispersion and the formation of interfacial voids, which in turn generate non-selective permeation pathways and deteriorate the overall membrane selectivity.

A double-sided coating SAZ-AF Janus separator was prepared by two kinds of MOFs: (1) high catalytic layer: derived from MOFs that has single atom catalysts with activity towards lithium polysulfides (LiPSs) (2) inhibition of lithium dendrite layer: derived from anionic MOFs with rapid lithium-ion conduction that can avoid growth of lithium dendrite. The SAZ-AF Janus separator produced exhibited excellent performance in different Li-S batteries coated with single atom catalysts (with a capacity decay rate of 0.05% after 2C and 1000 cycles) and also demonstrated excellent performance in protecting the lithium negative electrode (stable cycling for 2800 hours at 10 mAh $cm^{-2}$). In addition, the separator shows excellent performance also in Li-$SeS_2$ and Li-Se batteries[59].

Benefiting from the multiscale tunability of MOFs, a wide range of functional MOF-derived metal compounds have been designed. The uniformly distributed metal active sites within these materials can strongly anchor soluble polysulfides through Lewis acid-base interactions, effectively preventing their migration to the anode. Moreover, these metal centers act as efficient electrocatalytic sites that accelerate the redox conversion between long-chain and short-chain polysulfides, thereby enhancing reaction kinetics. For instance, He et al. achieved the in-situ growth of MOFs on polypropylene (Celgard) separators and subsequently converted them into $Co_9S_8$-Celgard separators via a solvothermal sulfurization process. The

resulting separators enabled cells to deliver high capacity and stable cycling performance over a wide current range (0.1-2 C), demonstrating that they not only effectively suppressed the shuttle effect but also accelerated the redox kinetics of polysulfides [60].

Similarly, Wang et al. synthesized nitrogen-doped carbon-cobalt (N-C-Co) thin films derived from MOFs as functional interlayers. This coating effectively restricted the migration of $Li_2S_x$ species from the cathode during cycling. Moreover, the hierarchical porosity and nitrogen-doped carbon framework provided both physical confinement and chemical adsorption of polysulfides, thereby further mitigating the shuttle effect [61].

In addition, various MOF-derived metal composites combine with carbon/polymer (such as MnS/N-C@ CNT derived from MOF as a precursor[62], $NiCo_2S_4$@C[63], Co/NCNS/CNT[64], $Co_3O_4$/PI/LLZO[65], NiO@ZnO[66], N-$Ti_3C_2$/C[67], $CoS_2$-LBLCN[68], NSPCF@$CoS_2$[69]) have been successfully employed as functional layers. The integration of MOF-derived metal compounds with conductive frameworks not only enhances the electrical conductivity but also ensures a homogeneous dispersion of catalytic active sites. These materials effectively anchor polysulfides through strong chemical adsorption on exposed metal or polar surfaces, while the open metal sites catalyze the reversible redox conversion of polysulfides, accelerating the reaction kinetics. Moreover, the interconnected carbon or polymer networks facilitate rapid electron and ion transport, further reducing polarization during cycling. As a result, such MOF-derived hybrid structures provide synergistic physical confinement, chemical anchoring, and catalytic activation, thereby achieving efficient shuttle suppression and long-term electrochemical stability.

Currently, there are four typical ways to make functional separator:

(1) Doctor-blade coating: Functional materials are first dispersed into a slurry and then uniformly coated onto the separator using a doctor blade. This method is widely used for powder-based materials due to its simplicity and controllable film thickness.

(2) Dip-coating: The separator is immersed in a slurry containing the functional materials for a controlled period, allowing for surface adsorption or infiltration. This technique is suitable for small- to medium-scale industrial production.

(3) Solution casting: Functional materials are dissolved or dispersed in a suitable solvent, and the separator is subsequently immersed in the solution to form a thin functional film. This method is often applied when solution-phase reactions or uniform film coatings are required.

(4) Vacuum filtration: Functional materials dispersed in a solvent are filtered under vacuum to deposit a uniform coating layer on the separator surface. This technique is particularly effective for producing thin, compact, and well-adhered functional layers.

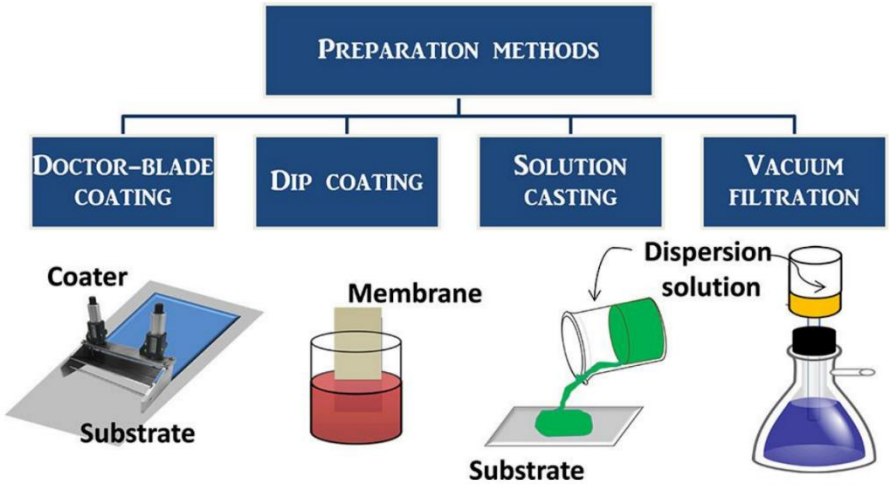


Figure 2.11 Schematic diagram of preparation method for functional separator[70].

In summary, the rational design of sulfur-containing polymers and functional separators has provided effective strategies to overcome the long-standing challenges of sulfur-based batteries, including polysulfide shuttle, poor conductivity, and sluggish redox kinetics. These materials integrate multiple to achieve enhanced electrochemical capacity and long-term stability, such as chemical anchoring, catalytic conversion, and conductive confinement.

Building upon these advances, the next chapter outlines the research statement and hypotheses that form the conceptual framework of this study. It proposes testable hypotheses

regarding how structural design, interfacial engineering, and catalytic regulation influence the electrochemical behavior of sulfur-based polymer systems.

# Chapter 3 Research Statement & Hypothesis

In this thesis, sulfur-containing polymers are used as cathode materials to solve the challenge in shuttle effect of RT Na-S batteries by the special crosslink structure and covalent bonding. The thesis aims to investigate the electrochemical behavior and structural evolution of sulfur containing polymer cathodes in Na-S batteries, identify the key redox processes occurring during the initial charge-discharge cycles and understand how the polymer structure interacts with sodium ions and sulfur species. On this basis, inspired by the distribution of sulfur atoms in polymers, a new method for synthesizing uniformly sulfur distributed sulfur-carbon composite cathodes by solvent method was explored.

It is hypothesized that the chemical environment of sulfur and the type of heteroatomic linkages within the polymer backbone critically determine the reversibility and stability of sulfurized polymer cathodes in Na-S batteries. Specifically, polymers with covalently bonded sulfur chains, such as sulfurized polyacrylonitrile (SPAN), may undergo irreversible structural rearrangements under deep discharge, resulting in shortened sulfur chains and reduced electrochemical activity. At same time, the absence of a polar functional group of SPAN may limit its ability to effectively anchor sodium polysulfides, leading to capacity fading during long-term cycling. In contrast, sulfur-containing polymers enriched with polar functional groups are expected to form stronger chemical interactions with polysulfides, thereby suppressing their diffusion and improving stability. However, the polar functional groups containing highly active nitrogen or oxygen are expected to exhibit strong chemical interactions with sodium polysulfides, which can initially enhance anchoring but eventually lead to irreversible bond reconstruction and capacity decay.

To further optimize the electrochemical performance, it is proposed that constructing sulfur-carbon composites via solution-based synthesis are expected to promote homogeneous sulfur

distribution. It is hypothesized that the homogeneous sulfur distribution in carbon material can facilitate charge transfer and ion diffusion during electrochemical reactions, thereby enhancing the reaction kinetics and cycling stability. In summary, this research aims to validate the hypothesis that there is a relationship between the molecular structure of sulfurized polymers, their redox reversibility, failure mechanisms, and overall electrochemical stability.

The main research contents of this thesis are as follows:

**(1) Materials design and synthesis.** According to the requirement of RT sodium-sulfur batteries, the materials with high conductivity and excellent structure are designed, which used inverse vulcanization method to synthesize materials with high sulfur content. The reverse vulcanization method can make the polymer have a sulfur content of more than 90%, which is far higher than the traditional vulcanization method. In addition, the reverse vulcanization method can directly use elemental sulfur ($S_8$) as one of the reaction monomers, avoiding the complex precursor synthesis steps, reducing costs and improving sustainability. Most importantly, the reverse vulcanization method can regulate the cross-linking density of the polymer by selecting different small molecules as co-monomers, thereby optimizing the mechanical properties, conductivity and stability of the material. In addition, the reverse vulcanization method can use sulfur from industrial by-products as a reactant (such as sulfur produced during petroleum refining), which helps to reduce the accumulation of sulfur waste and is in line with the concept of green chemistry.

**(2) Electrochemical characterization.** The materials are electrochemically characterized by using different techniques. The interfacial reaction, mesophase state, stability of the interface, and electrochemical kinetics is provided by cyclic voltammetry (CV). The electrochemical kinetics of interface reaction is studied by electrochemical impedance spectroscopy (EIS).

The stability and capacity are test by rate performance test and long cycle test under different specific current.

**(3) Analyze the working mechanism of the cathode.** The working mechanism of cathode is analyzed to get the principle of the polymer in the sodium-sulfur cell. The phase change and intermediate compounds during the electrochemical reactions is observed by *in-situ* Raman spectra. The changes in the internal chemical composition of the electrode and detailed information on interface chemistry is analyzed by XPS. The structural changes of electrodes and the conversion process of polysulfides is observed by *in-situ/ex-situ* Raman spectroscopy (provided by collaborator).

# Chapter 4 Characterization Techniques and Electrochemical Measurement

## 4.1 Introduce about Materials

**C65 (conductive carbon 65).** C65 conductive carbon is a high-performance carbon black material widely used in lithium-ion batteries, supercapacitors, and various electrode systems to enhance electronic conductivity and facilitate electron transport within the electrodes[71, p. 65]. It typically possesses a specific surface area of 60-80 $m^2$ $g^{-1}$ and an average particle size ($D_{50}$) of approximately 35-45 nm. Compared with other conductive carbon blacks, C65 offers several advantages:(1) High electrical conductivity: effectively promotes electron transport and improves rate capability;(2) Excellent dispersibility: easily disperses in electrode slurries, ensuring uniform coating and stable electrode structure;(3) Moderate specific surface area: reduces excessive electrolyte adsorption, thereby enhancing electrode stability;(4) High thermal and chemical stability: resists oxidation and degradation, suitable for long-cycle applications. Due to the balance between conductivity, dispersibility, and cost, C65 has become one of the most widely used conductive carbons in the lithium battery industry. Compared with Super P, C65 exhibits superior dispersibility, while being easier to process and handle than Ketjen Black.[72]. In Na–S batteries, the incorporation of C65 into the sulfur cathode facilitates the formation of a continuous and highly conductive network, which significantly improves electron transport and ensures uniform electrochemical reaction throughout the electrode. Moreover, its moderate surface area provides sufficient interfacial contact with sulfur species while minimizing undesirable electrolyte adsorption, thereby maintaining electrode stability.

**LA133.** The copolymer LA133 is composed of acrylamide (AM), lithium methacrylate (LiMAA), and acrylonitrile (AN) as a kind of water-based binder. LA133 not only contains highly polar hydrophilic cyanide/amide groups, which can provide sufficient adhesion strength between conductive agents, active materials, and current collectors, but also contains relatively low polarity lipophilic ester groups, which can introduce appropriate flexibility for the electrode (Figure 4.3). In addition, LA133 binder with vinyl-vinyl structure skeleton is softer than commonly used water-based CMC binder with ring-ring structure[73]. LA133 has following advantages: (1) Water-based system. Compared with the traditional NMP (N-methylpyrrolidone) solvent-based PVDF binder, LA133 uses water as solvent that is more environmentally friendly and safe, it can also reduce solvent recovery costs. (2) Good bonding performance. It can improve the adhesion between the active material and the current collector to enhance the mechanical stability of the electrode. (3) Excellent flexibility. Compared with pure PVDF, LA133 has better elasticity, which can improve the crack resistance of the pole piece and reduce the problem of powder removal.

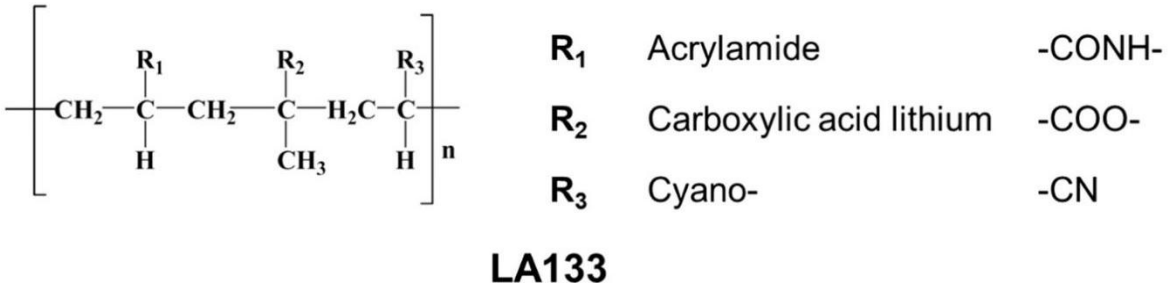


Figure 4.1 Schematic diagram of LA133[73]

### 4.2 Introduce of Inverse Vulcanization Method

Inverse vulcanization is a strategy for synthesizing sulfur-containing polymers using elemental sulfur as the main reactive monomer. Unlike the traditional vulcanization process (which uses a small amount of sulfur to crosslink rubber to improve its mechanical

properties), the reverse vulcanization method induces ring opening polymerization of elemental sulfur at higher temperatures (usually 160-200 $^{o}$C) to generate reactive polysulfide radical segments, which further crosslink with organic monomers containing carbon-carbon double bonds (such as olefins, ene-ethers, or ketone compounds) to form a high sulfur content covalently crosslinked polymer network.

The polymers synthesized via this method possess sulfur-rich backbones in which sulfur chains constitute the primary structural units, with the sulfur content typically exceeding 50 wt.%. Owing to their unique chemical composition and tunable cross-linked network, these inverse vulcanized polymers exhibit outstanding thermal stability, remarkable infrared absorption characteristics, strong metal-ion complexation capability, and notable electrochemical activity, while the overall synthesis process remains relatively simple and efficient.

### 4.3 Synthesis of Different Polymers by Inverse Vulcanization Method

**Synthesis of Sulfurized polyacrylonitrile (SPAN)**

In a typical process, excess of sulfur (Alfa Aeasar, 99.98%) and polyacrylonitrile polymer powder (Aldrich, average Mw=150,000) were mixed thoroughly in agate mortar with a mass ratio of 10:1. Subsequently, the mixture was hated in a tubular furnace at a ramp rate of 2℃/min to 270℃ and held at that temperature for 6 h under Nitrogen atmosphere. Unreacted free sulfur is removed from the nitrogen steam during the cooling process. The dark powder SPAN around 5g was obtained upon cooling down to 25$^{o}$C. The sulfur content of SPAN is 44.3% (measured by elemental analysis).

**Synthesis of Novel Sulfur Rich Polyamide (P1)**

In this part, the same protocol for the Catalysed Inverse Vulcanization of MBA was carried out according to a previously reported literature procedure [74].

1 g (3.90 mmol) of elemental sulfur was placed to a vial containing 0.056 mmol of the catalyst (which corresponds to either 0.0078 g of 1,5,7-triazabicyclo [4.4.0] dec-5-ene (TBD) or 0.0086 g of 1,8-Diazabicyclo (5.4.0) undec-7-ene (DBU)). The mixture was heated at 135°C with a stirring rate of 200 rpm for 10 to 20 min. Subsequently, the *N, N'*-Ethylenebisacrylamide was then added (1g, 6,49 mmol) to the mixture, and the stirring rate was raised to 900 rpm. Due to its solid state, the mixture was not homogeneous. During the synthesis, a gas was produced, which was expected to be $H_2S$[75]. The reaction was stopped after 2 hours of stirring at 135 °C. Most reactions yielded hard brownish solids at the bottom of the vial with a black crust on the sides in addition to unreacted *N, N'*-Ethylenebisacrylamide, which was found on the upper part of the reaction flask. The hard solids were very difficult to remove from the vial.

After grinding the solid into powder, the powder was washed with THF and then DMSO. A wet brown solid was collected and placed in a vial containing THF, which was then stirred overnight. At this point, a literature procedure was followed to remove unreacted sulfur[76]. After the filtration, the collected powder was treated with toluene at 60°C for 15 min under a stirring at 600 rpm. Upon filtration, the collected powder residue was dried overnight under vacuum, with a pressure lower than $4x10^{-4}$ mbar. The synthesis process is shown in Figure S1. The sulfur content of resulting polymer **P1** is 63.0% (conformed by TGA).

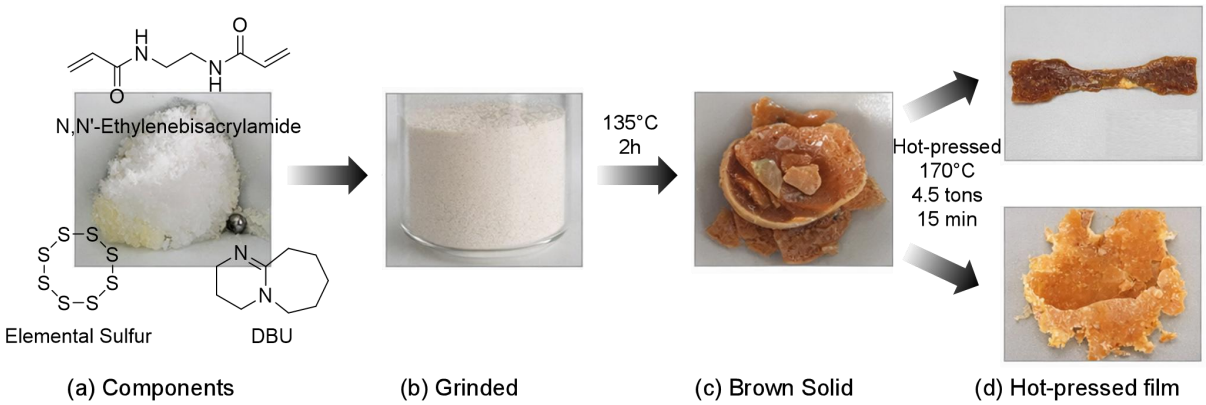


Figure 4.2 Synthesis process of **P1**

### 4.4 Synthesis of Carbon-Sulfur Composite by Solvent Method (CS)

In a typical process, 0.25g Super carbon 65 (C65, MTI Corporation) and 0.75 g sulfur (Alfa Aeasar, 99.98%) (25%:75% in mass ratio) were well mixed and put into N-Methyl pyrrolidone (NMP, Sigma-Aldrich, 99.5%) in mass ratio of solid to liquid of 1:10, then heated to 180℃ for 2h to get dark solution. A vacuum filter was used to obtain dark powder (CS) after solution was cooled down. The sulfur content of CS is 56.1% (measured by elemental analysis)

### 4.5 Materials Characterization

**Scanning Electron Microscopy (SEM-EDX).** The morphological characterization of materials and the separators was done through the scanning electron microscopy technique (FE-SEM, MERLIN-Zeiss) with an acceleration voltage of 10 keV, while the surface elemental distribution of materials over the glass fiber separator was determined from energy-dispersive X-ray spectroscopy (EDX, Quantax-Bruker).

**X-ray Diffraction (XRD).** The powder X-ray diffractometer (XRD) was used to measure the phase composition and crystal structure of the materials. The XRD patterns of materials were collected and recorded on a STOE STADI P COMBI diffractometer with Mo-K$\alpha_1$-radiation

(λ=0.7093 Å with focusing Ge 111 monochromator) in Debye-Scherrer geometry at room temperature. The diffractogram was collected from 2° to 50°.

**X-ray photoelectron spectroscopy (XPS).** XPS measurements were carried out to determine the chemical environment of samples before and after the polysulfide adsorption test, and before/after cycles with cell to see the interface of positive electrode; the samples after the adsorption test and the electrode after cycled were decanted, washed two times with 100 μL of TEGDME solvent, and dried at 40 °C under vacuum for 48 hours.

**Elemental Analysis.** Elemental analysis is test under Argon atmosphere and conduct three parallel tests on each sample to get the sulfur content of sulfur-containing polymers.

***In-Situ/Ex-situ* Raman Spectroscopy.** *In-Situ* Raman Spectroscopy was used to analyze the SPAN cathode. A typical electrochemical cell used for *in-situ* Raman spectroscopy test of sodium sulfur cell is shown in Figure 4.4. The sulfur-containing positive electrode, separator, and metal anode are sealed in the cell, and electrochemical reactions occur through charging-discharging process. At the same time, the quartz window is designed on the surface of the cell shell to ensure effective input of laser beam and collection of Raman signals[77]. Figure 4.4a shows a typical In-Situ electrochemical cell for sulfur cathodes observation. In this case, the sulfur cathode contacts with quartz window, to ensure effective penetration of the laser beam through the cathode to obtain Raman signals, the sulfur cathode typically uses an aluminum mesh as the current collector[78]. When the current collector cannot be replaced with aluminum mesh, an alternative solution of metal anode contact with quartz window can be adopted (Figure 4.4b). In this case, small hole needs to be created on the surface of the metal anode and separator to make the laser beam reach the cathode surface. In addition, it is necessary to perfectly seal the electrochemical cell to isolate the interference of water/oxygen for the high reactivity of metal anodes and polysulfides.[79] (Figure 4.4c and 4.4d)

Raman spectroscopy was performed *in- situ* with a 532 nm focused laser beam and a 10x objective lens (LadRAM HR Evolution, HORIBAJobin Yvon). This experiment used *In-Situ* cell with sapphire window at anode side, the sodium negative electrode, glass fiber separator, and SPAN positive electrode were punched to create a small hole in the center for the excitation beam. Data were collected every 15 minutes during the charge-discharge process. Baseline calibration was taken for all data. *Ex-situ* Raman Spectroscopy was used to analyze the cathode before and after cycling, the cathode was washed two times with 100 μL of TEGDME solvent and dried at 40 °C under vacuum for 48 hours.

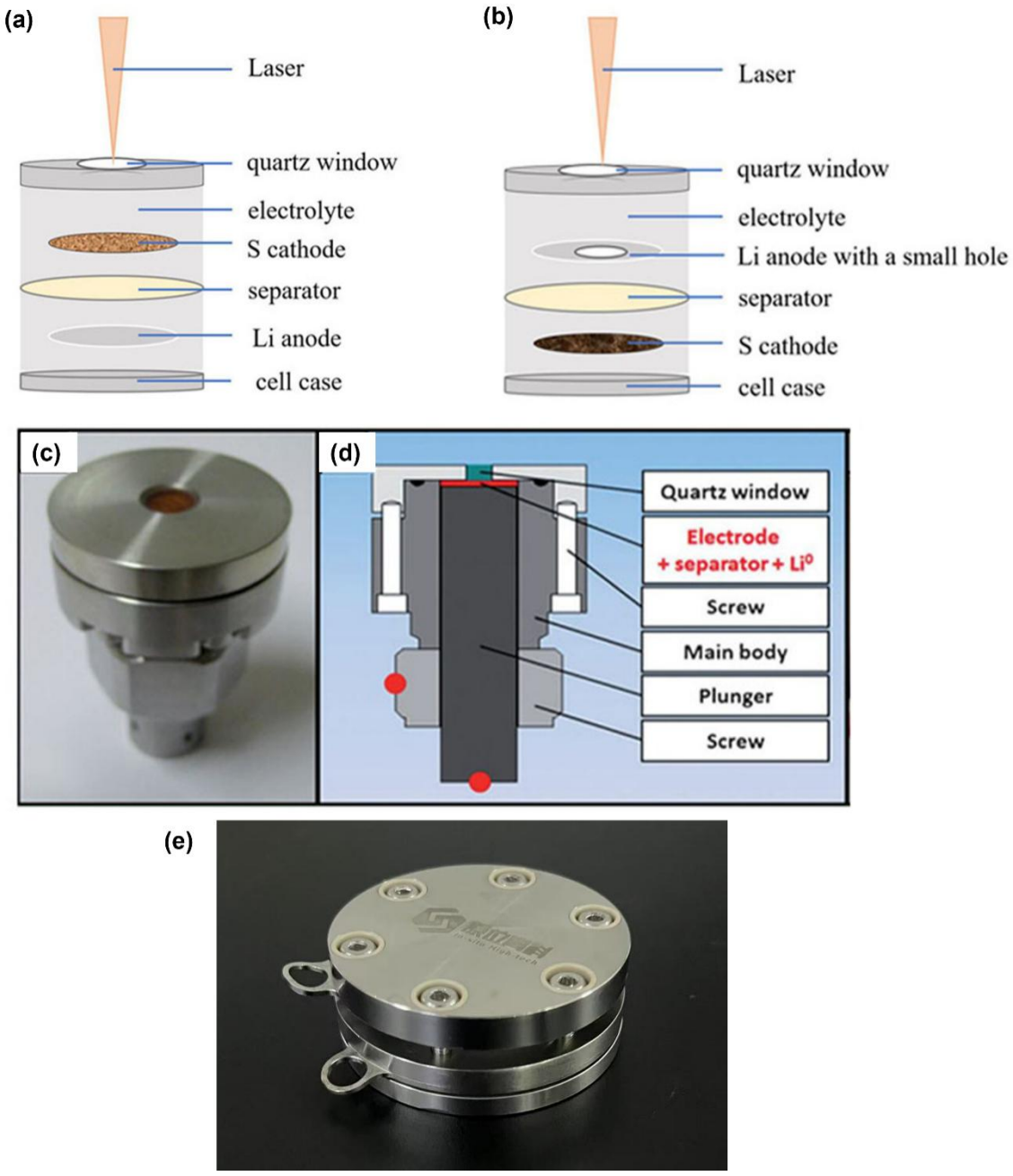


Figure 4.3 Schematic of a cell for the In-Situ Raman tests (a) For sulfur cathode with aluminum mesh as the current collector[77], (b) For sulfur cathode with aluminum foil as current collector, (c) The optical photos of electrochemical cell for In Situ Raman measurements, (d) Schematic diagram of in-situ cell[80], (e) In-situ Raman cell used for experiment in this thesis.

## 4.6 Electrochemical Characterization

### Preparation of Cathode

All electrodes were prepared by a classical slurry coating: the active material (sulfur-containing polymer), conductive agent (C65, MTI Corporation), and binder (LA133, MSE Supplies) were mixed in a mass ratio of 60:30:10. The detailed procedure is as follow: The LA133 binder was at first prepared as 3% (mass ratio) solution in a $H_2O$/ethanol (V: V=1:1). The polymer powder and C65 powder was at first mixed in agate mortar for 10 min, then LA133 solution was add into mixed materials. The components were dispersed evenly in a $H_2O$/ethanol (V: V=1:1) solution and stirred continuously for 12 h on magnetic stirrer to obtain a uniform black slurry. This slurry was then coated onto aluminum foil (Haeberle, 30μm, which was used as the current collector) using the Doctor Blade technique, with a wet thickness of 200 μm (adjustable film coater, Zehntner). The coated films were at first dried at room temperature to remove most solvent; after that, the electrode was dried at 60 ℃ under vacuum for 12h to further remove all the solvent. Subsequently, circular electrodes with a diameter of 12 mm were punched from the dried films (Figure 4.3).

After that, the completely dried electrode piece was cut into a circle with a diameter of 12 mm. On this basis, sulfur area content is calculated by following formula.

$$M_s=(M_e-M_{Al})*0.6*\text{sulfur content}/1.13$$

Where $M_e$= total mass of the cathode and $M_{Al}$= average mass of aluminum disk (4.41 mg), 0.6 is the ratio of cathode material in the electrode, and 1.13 is the area of electrode (1.13 $cm^2$, the area of a circle with a diameter of 12 mm is calculated by the formula for circle area). By above formula, sulfur loading of cathode is 0.5 mg± 0.1 $cm^{-2}$. For comparison, elemental sulfur cathode was prepared using elemental sulfur as active material, mixed with C65 and

LA133 in the same mass ratio of 60:30:10. The slurry was similarly prepared in $H_2O$/ethanol (V: V=1:1) solution and coated, subsequently dried under identical conditions. The sulfur loading was matched to that of SPAN-based electrodes to enable direct comparison.

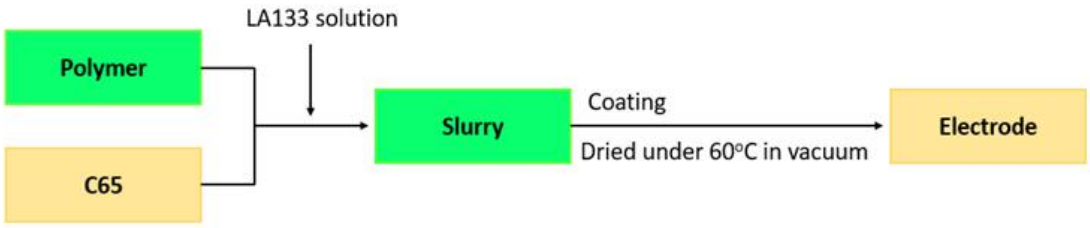


Figure 4.4 Preparation of electrode

**Preparation of Sodium Anode**

In this case, the anode material consists of pure sodium (Thermo Fisher Scientific, ≥99.8%). The preparation process of sodium metal anode is completed in a glove box. Normally, sodium metal is placed between two plastic films and rolled into thin sheets using a metal rod. Furthermore, the sodium sheet is cut into circular pieces with a diameter of 10mm as the negative electrode in cell assembly.

**Preparation of Electrolyte**

The preparation of electrolyte is completed in the glove box. Typically, sodium trifluoromethanesulfonate ($NaCF_3SO_3$, Tokyo Chemical Industry, >98%) was dried inside the glove box at 100 °C under vacuum for 24 h using a vacuum oven (Salvislab -vacucenter). For the solvent used in the electrolyte, 4Å molecular sieve is used to remove water, molecular sieves of 4Å (Honeywell Fluka) were dried at 300 °C in a furnace before used, then they were introduced into the glove box and added to the TEGDME solvent. The water was removed from TEGDME by molecular sieves for 72 h. On this basis, electronic balance was used in the glove box to weigh the required mass of $NaCF_3SO_3$ according to the electrolyte, and a fully dried syringe was used to measure the required volume of TEGDME. TEGDME

and $NaCF_3SO_3$ were stirred on a magnetic stirrer in a fully dried glass bottle for 24 hours to obtain a clear electrolyte.

**Assemble Three Electrode Swagelok Cell**

The three-electrode Swagelok cell were assembled in an argon filled glove box (MBRAUN-Lab Star Eco, $O_2$< 0.5ppm, $H_2O$<0.5ppm). The sulfur-containing polymer cathode was used as the working electrode, while sodium discs (10 mm diameter discs) served as the counter and reference electrodes. The electrolyte was composed of 1.0 M $NaCF_3SO_3$ (Tokyo Chemical Industry, >98.0%) dissolved in TEGDME (ThermoFisher, 99%), with a fixed volume of 75 µL per cell. In each cell, the ratio of liquid and sulfur (E/S ratio) is about 50 µL $mg_s^{-1}$(Figure 4.6).

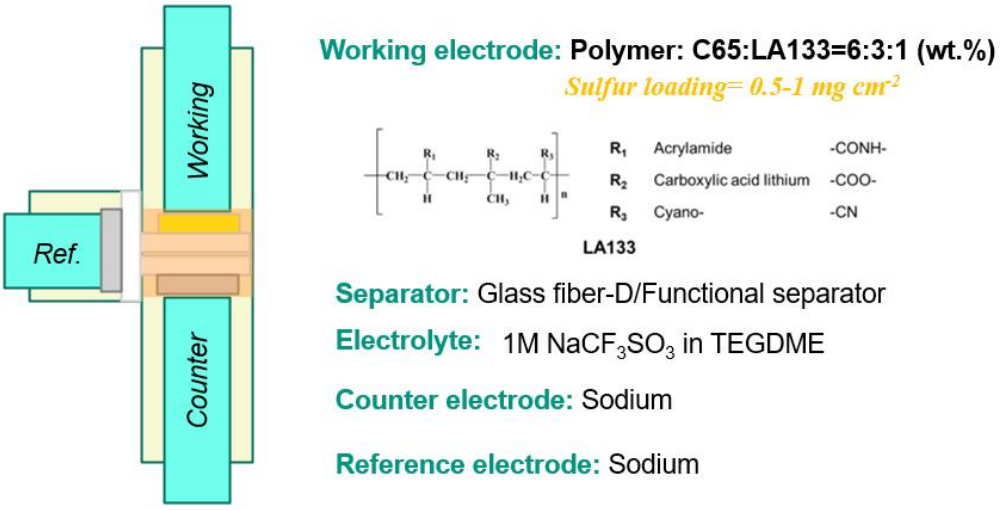


Figure 4.5 Details of cell assemble.

**Fabrication of Carbon Modified Separator**

The carbon-modified separator was fabricated using the Doctor Blade technique: A slurry consisting of carbon 65 and LA133 with a mass ratio of 7:3 was prepared in $H_2O$/ethanol solution (V: V=1:1) at room temperature, the solvent/solid material ratio was 10:1 (in mass ratio). The resulting slurry was stirred with a magnetic stirrer for 24h at room temperature.

Then, this the slurry was blade-coated onto one side of separator with a wet thickness of 150 μm (Whatman, Glass fiber-D). The solvent was removed by drying the coated separator at 60 ℃ under vacuum for 12 h Subsequently, discs with a diameter of 12 mm were punched out for cell assembly. The mass loading of C65 coating layer (contain binder) on separator is about 1.77 mg± 0.1 $cm^{-2}$, for C65 in coating layer loading is 1.24 mg± 0.1 $cm^{-2}$.

**Preparation of $MoS_2$ with Different Structure by Ball Milling**

A quantity of 1.5 g of bulk $MoS_2$ (Alfa Aesar, 99.98%) was ground in a planetary ball milling equipment (Fritsch-Pulverisette 7). The balls used for the reduction of the particle size were made of tungsten carbide. The grinding process was made in an argon atmosphere inside the jar and the speed used was 450 rpm. The set-up of the equipment consisted of 90 cycles of 30 minutes with a rest step of 10 minutes. The ball milled $MoS_2$ after 20 hours was obtained by stopping the equipment after the cycle number 40 and collecting one half of the material. Then the remaining quantity continued with the ball milling process (again under Ar atmosphere) and after the 90 cycles the powder was collected, stored and labeled as "BM $MoS_2$-45h"

**Preparation of $MoS_2$ Functional Separator**

$MoS_2$ functional separator was obtained by vacuum filtration method. The $MoS_2$ nanosheet was mixed with C65 (MTI Corporation) ($MoS_2$:C65 wt.% ratio=4:1) with different ball milling time and dissolved in deionized water. This solution was magnetically stirred for 12h to get slurry for vacuum filtration method (0.02 g $mL^{-1}$). The glass fiber-D separator was cut into a circle with a radius of 2cm and put on Buchner funnel, then the vacuum was open to make the glass fiber-D stick on the surface of the Buchner funnel for filtration. The above slurry was dropped on glass fiber-D by 2ml dropper to obtain uniform $MoS_2$ layer. The functional separator was dried in 60$^{o}$C for 12h and cut as circle with 12mm radius. The coating loading mass of functional layer is 25.0 mg $cm^{-2}$.

**Galvanostatic Tests**

The rate performance and long cycle test was obtained by the VMP-3 potentiostat (BioLogic Science Instruments), galvanostatic charge and discharge were performed in different voltage windows between 0.5V-2.7V (vs. $Na^+/Na$), 1.2V-2.7V (vs. $Na^+/Na$), and 1.4V-2.7V (vs. $Na^+/Na$). For the rate capability, the test process at the current density of 500mA $g^{-1}$, 1000mA $g^{-1}$, 2000mA $g^{-1}$ between 0.5V-2.7V (vs. $Na^+/Na$), 1.2V-2.7V (vs. $Na^+/Na$), and 1.4V-2.7V (vs. $Na^+/Na$). For long cycling, the test process at 500mA $g^{-1}$ for 200 cycles between 1.2V-2.7V (vs. $Na^+/Na$). All cells were tested in a climate chamber at 25°C. All capacity is calculated by mass of sulfur in cathode, for SPAN it is calculated by sulfur content of SPAN.

**Cyclic Voltammetry (CV)**

Cyclic voltammetry (CV) was performed at 1.2V-2.7V (vs. $Na^+/Na$), 1.4V-2.7V (vs. $Na^+/Na$), 1.6V-2.7V (vs. $Na^+/Na$), 1.8V-2.7V (vs. $Na^+/Na$) under scanning rate of 0.1 mV $s^{-1}$, 0.2 mV $s^{-1}$, 0.5 mV $s^{-1}$ and 0.8 mV $s^{-1}$. All cells were tested in a climate chamber at 25°C.

**Impedance Spectroscopy (EIS)**

The same instruments are also used for electrochemical impedance spectroscopy (EIS) in an alternating current voltage of 5 mV with a frequency range from 100 mHz to 100kHZ. All cells were tested in a climate chamber at 25°C.

**Sodium Polysulfides Absorption Test**

The absorption capacity of materials was tested with a sodium polysulfide solution. Na2S (Sigma Aldrich, ≤100) reacted overnight, at room temperature and magnetically stirred with S in 10 mL of anhydrous TEGDME to form the sodium polysulfide solution with a

concentration of 0,1 M ($7S + Na_2S \rightarrow Na_2S_8$). Then in four bottles was added 150 uL polysulfide solution and 1350 uL more of TEGDME to obtain four solutions of 0.01 M. One of these bottles was labeled as “Control”, in the second one was added 16 mg of bulk $MoS_2$, in third and fourth bottles was added again 16 mg of ball milled $MoS_2$ after 20 and 45 hours, respectively. The bottles were photographed at time 0, and after 2 and 72 hours of test, for the registration of the color changes in the solutions.

# Chapter 5 Results and Discussion

## 5.1 Depth-of-Discharge-Dependent Chemical Evolution in Sulfurized Polyacrylonitrile Cathodes for Ether-Based Room-Temperature Sodium–Sulfur Batteries

### 5.1.1 Introduction

Rationale cathode design is crucial to address the challenges in chapter 1.3 [81]. One widely adopted strategy involves engineering porous cathodes or incorporating sulfur into conductive carbon matrices, which can physically anchor polysulfides, thereby reducing their dissolution into the electrolyte and mitigating the shuttle effect[82], [83], [84].

Among various sulfur-based cathode materials[85], the sulfurized polyacrylonitrile (SPAN) contains short-chain sulfur species ($S_{2\text{-}3}$) that are covalently bonded to the polyacrylonitrile (PAN) backbone. SPAN is a sulfur–polymer composite obtained by chemically incorporating sulfur into the backbone of polyacrylonitrile (PAN, -$CH_2$–CH(C≡N)-). SPAN is typically synthesized through heat treatment of PAN with elemental sulfur, during which a portion of the nitrile (-C≡N) groups are replaced by sulfur species, leading to the formation of C–S and S–S bonds. In this process, elemental sulfur becomes covalently bonded to the carbon backbone, forming short sulfur chains or clusters (e.g., $S_8$ rings and linear $S_2$/$S_3$ units) rather than existing as free sulfur. Such chemical bonding effectively anchors sulfur atoms, thereby suppressing their dissolution into the electrolyte and mitigating the polysulfide shuttle effect.

Additionally, the heat treatment induces partial conjugation within the PAN backbone, improving the intrinsic electronic conductivity of the material compared to insulating elemental sulfur. The stabilized conjugated structure, together with the covalently bound short-chain sulfur species, prevents the formation of soluble long-chain polysulfides during electrochemical cycling. As a result, SPAN exhibits enhanced structural stability and

electrochemical performance, distinguishing it from conventional sulfur-based cathode materials.

However, despite its proven efficacy in Li–S systems and ester-based Na-S batteries[86], the application of SPAN in ether-based electrolyte Na–S batteries remains relatively unexplored, offering an exciting and timely opportunity for research[85]. The ether-based electrolytes could generate dense solid electrolyte interphase (SEI) layers for sodium metal anode to achieve enhanced cycling stability than ester-based electrolyte[87]. At the same time, the degradation mechanism of SPAN positive electrode in ether-based electrolyte RT Na-S batteries remains poorly understood. Therefore, it is important to elucidate the structural and electrochemical changes occurring during the initial charge-discharge cycle of the SPAN cathode, as this understanding can serve as a blueprint for cathode structure design and electrode optimization. Subsequently, in this study, SPAN is used as the cathode material in RT sodium-sulfur batteries with ether-based electrolytes (i.e.,1M $NaCF_3SO_3$ in TEGDME) under high current density conditions. The decay mechanism occurring during the initial few cycles is explained. In addition, cycles tests at different depths of discharge and post-mortem study are conducted to provide insights into the evolution of interfacial reactions within the SPAN-sodium cell. On this basis, to further enhance stability and rate capability, carbon functional separator configurations are explored and evaluated.

### 5.1.2 Result and Discussion

**Synthesis and characterization of materials**

To validate the synthesis, elemental analysis was used to determine the sulfur content, which was found to be 44.3% (Table 5.1). Additionally, X-ray diffraction (XRD) was employed to confirm the structural characteristics of SPAN[37].The XRD pattern reveals that SPAN is amorphous without any crystalline signals of $S_8$, indicating that elemental sulfur had successfully bonded with PAN to form a sulfur-containing polymer network[88]. (Figure 5.1)

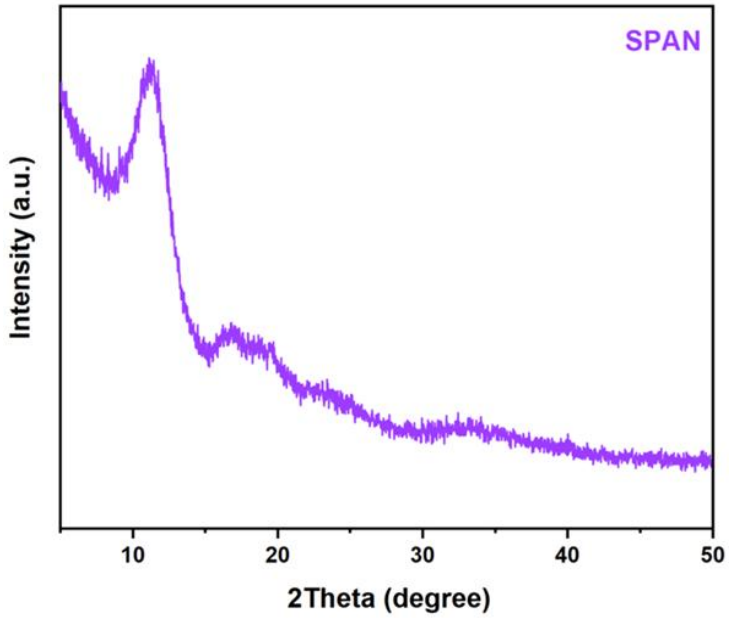


Figure 5.1 XRD of SPAN

Table 5.1 Elemental analysis of SPAN

| Sample | N% | C% | H% | S% |
|---|---|---|---|---|
| SPAN | 15.4 | 42.8 | 1.2 | 44.3 |

**Electrochemical behavior of SPAN**

CV is used to study the electrochemical behavior of SPAN between 0.5-2.7V (vs. $Na^+/Na$). As shown in Figure 5.2a, during the initial reduction process, SPAN exhibits a reduction peak centered at 1.2-1.5 V. This peak is generally associated with the sodiation of short sulfur chains covalently bonded within the SPAN framework, leading to the formation of short-chain polysulfides and $Na_2S$ [89]. Owing to the absence of free $S_8$ or long sulfur chains in pristine SPAN, no distinct reduction features related to long-chain polysulfides are observed in the initial discharge process [90]. In the subsequent anodic scan, a pronounced oxidation peak appears at around 1.7-1.9 V, which can be attributed to the partial desodiation of $Na_2S$ and the regeneration of sulfur species confined within the SPAN structure [91]. In addition, a

weak and broad oxidation feature located between 2.2 and 2.5 V is observed in the first cycle. This feature has been reported in previous studies and is commonly associated with the oxidation of higher-order polysulfide species [6]. However, its low intensity suggests that only a limited amount of such species may be involved [92]. After the first cycle, a new cathodic peak appears at around 2.0 V. The appearance of this peak indicates a change in the reduction behavior after the initial electrochemical activation. This phenomenon can be attributed to the incomplete reincorporation of sulfur species formed during the first cycle into the SPAN backbone, giving rise to weakly confined or electrolyte-accessible polysulfides that participate in subsequent redox processes [93]. Notably, after three cycles, the broad and small oxidation peak in the 2.2V - 2.5V range disappears and does not reappear in subsequent cycles with higher scan rates (as shown in Figure 5.2b).

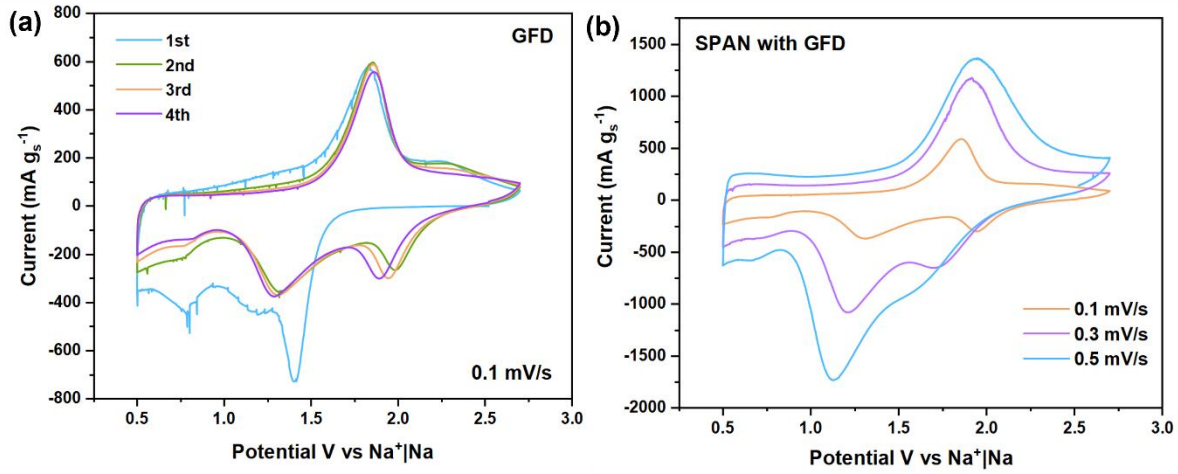


Figure 5.2 (a) CV curve of SPAN electrode at 0.1mV/s, (b) CV curve of SPAN electrode at different scan rates (Three electrodes cell with working electrode: SPAN, counter electrode: sodium, reference electrode: sodium. Electrolyte: 1M $NaCF_3SO_3$ in TEGDME)

To clarify the reasons for the disappearance of the small and broad peak between 2.2V-2.5V, CV curves (Figure 5.3a) were recorded within a different potential ranges(i.e.,1.4V-2.7V, 1.5V-2.7V, 1.6V-2.7V, 1.7V-2.7V, and 1.8V-2.7V). It is worth noting that after repeated cycles within a small range, the small peak between 2.2V and 2.5V does not disappear. This

result indicates that the reduction reactions occurring below 1.4 V cause the disappearance of the small high-voltage oxidation peak. To further support this conclusion, narrow range CV tests were conducted from the direction high to low potential using the same SPAN//Na cell to avoid the impact of possible irreversible reactions on further cycles that may exist at lower potentials (Figure 5.3b).

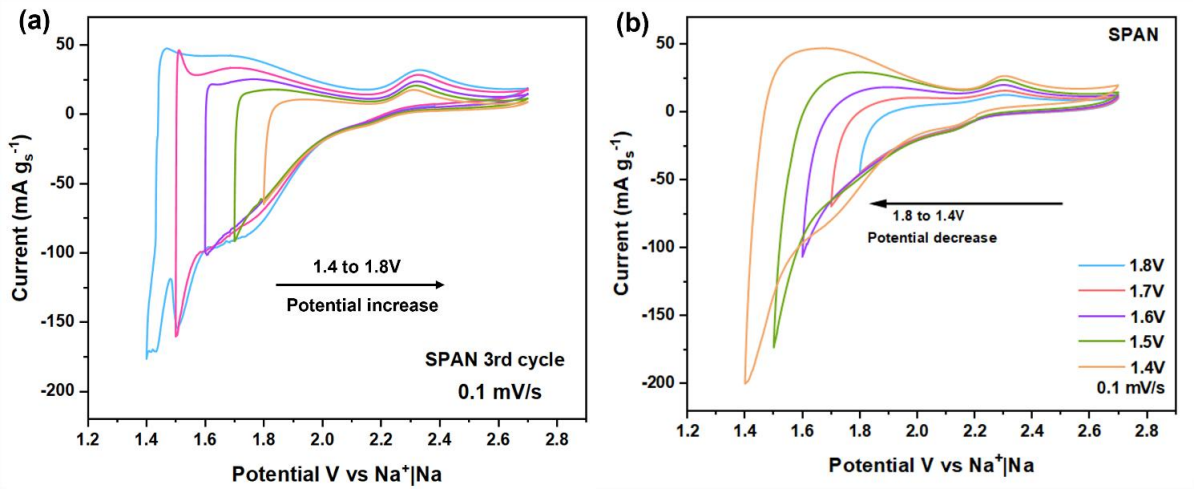


Figure 5.3 (a) CV curve test with potential opening with the lowest cut-off from low to high, (b) CV curve test with potential opening with the lowest cut-off from high to low. (Three electrodes cell with working electrode: SPAN, counter electrode: sodium, reference electrode: sodium. Electrolyte: 1M $NaCF_3SO_3$ in TEGDME)

Fig. 5.3b shows that by pushing the potential progressively to lower values (i.e., by pushing the reduction reaction) the broad oxidation peak between 2.2V and 2.4V increases, indicating that this oxidation process is a response to the reduction reaction. However, when the voltage drops down to 1.0V (as shown in Figure 5.4), the small peak between 2.2V and 2.4V becomes broader and hidden by the capacitive current. However, when the lower cut-off voltage increases from 1.0V to 1.2V, the small oxidation peak between 2.2V and 2.4Vcan be clearly observed again and becomes more pronounced when the lower cut-off voltage increases to 1.8V. This result indicates that the deep discharge in the low voltage region eventually inhibits the oxidation reaction between 2.2V and 2.4V.

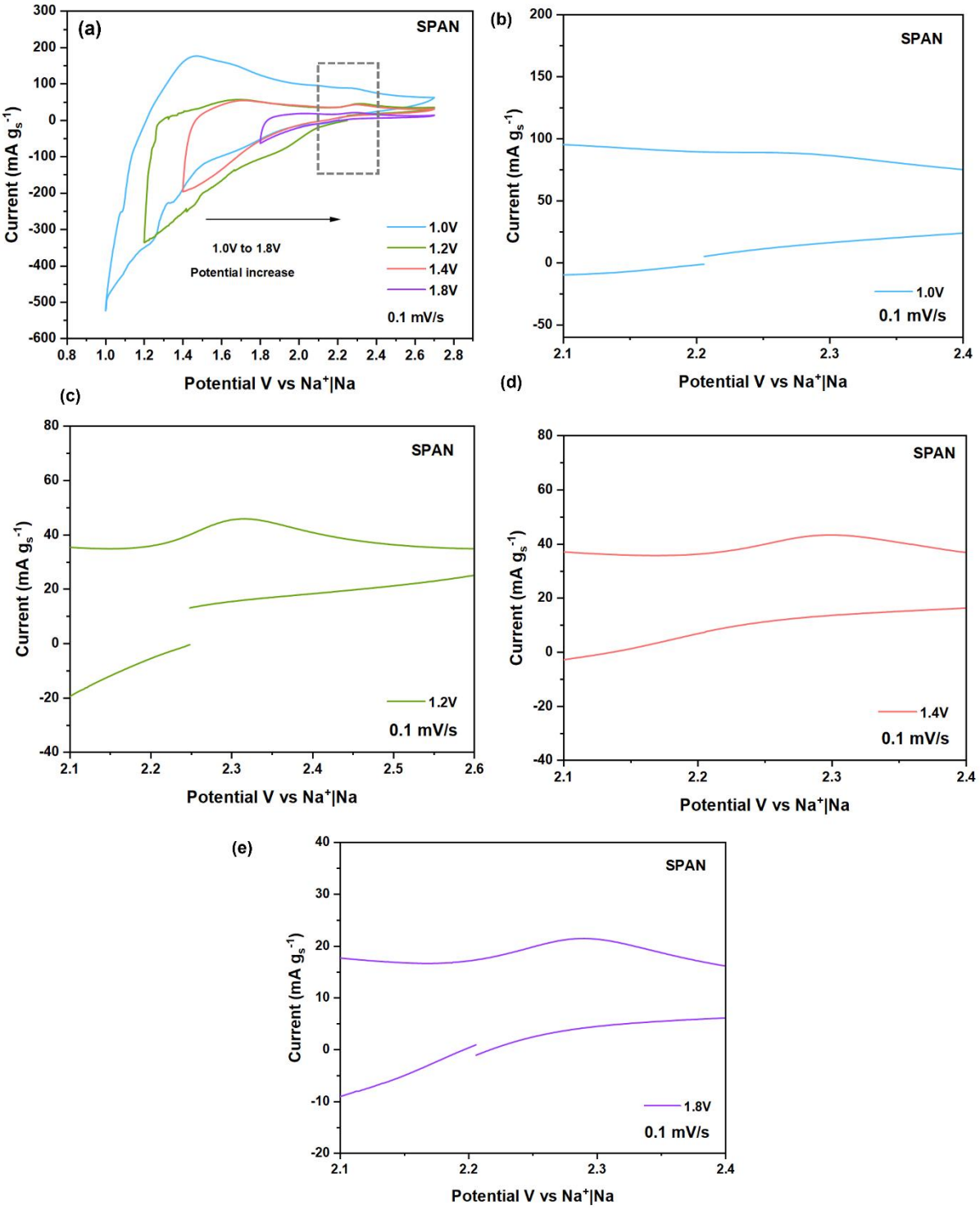


Figure 5.4 (a) CV curve of SPAN cells scanned with different lower potential cut-off (from low to high), (b-e) Enlarged view of the CV curves between 2.1V-2.4V. (Three electrodes cell with working electrode: SPAN, counter electrode: sodium, reference electrode: sodium. Electrolyte: 1M $NaCF_3SO_3$ in TEGDME)

***In-Situ* Raman spectroscopy and density functional theory calculation**

In order to further observe the reaction during the deep discharge process of the SPAN cell, *In-Situ* Raman spectroscopy was conducted during the complete discharge-charge process of the SPAN cell from 0.5V to 2.7V. As shown in Figure 5.5a, the peaks observed at 313, 370, 394, and 805 $cm^{-1}$ in the SPAN spectrum correspond to the vibrations of C-S bonds, confirming the presence of covalent carbon – sulfur linkages within the polymer structure. Furthermore, additional peaks detected at 473 and 936 $cm^{-1}$ are attributed to the ring stretching modes of S-S bonds. Finally, the most intense signals at 1345 and 1550 $cm^{-1}$ were assigned to the D and G bands typical of carbonaceous materials[92]. After cell assembly, the SPAN electrode exhibits a modified spectrum due to slight sulfur dissolution. A decrease in the intensity of the C-S bond signals is observed, along with the emergence of characteristic dissolution products, including long-chain polysulfide ions ($S_x$) at 483 $cm^{-1}$ and $S_3^-$ species at 534 $cm^{-1}$. It is worth noting that a distinct signal is present at 534 $cm^{-1}$ from the very beginning, this feature may arise from the stacking background associated with S-S bonds, which typically appear in the 430-550 $cm^{-1}$[94]. The D and G bands disappear after the electrode comes into contact with the electrolyte because a passivating cathode electrolyte interphase (CEI) forms. After sodiation to 0.57V, the D band becomes visible again. This reappearance occurs because sodium ions begin to interact with and insert into the carbonaceous SPAN framework once the CEI has already formed, and this insertion induces increased structural changes that restore the Raman activity associated with the D band. At the beginning of discharge, the Raman spectrum exhibits a Raman peak located at 460$cm^{-1}$, which usually corresponds to short-chain sulfur in SPAN. During the discharge to 0.5V, this signal gradually weakens, corresponding to the breakage and reduction of short-chain sulfur in SPAN. When the potential is below 1.0V, a significant increase in Raman signals was observed at 423$cm^{-1}$ (C-S), 534 $cm^{-1}$ ($S_3^-$ species), and 1345 $cm^{-1}$ (D band) (Figure 5.5b and

5.5c). [95]. The above results indicate that during low-voltage discharge (below 1.0 V), sodium ions form irreversible interactions with the C or N atoms within the SPAN. This process increased structural disorder within the carbonaceous framework, which contributes to the enhancement of the D-band signal [96], [97]. Meanwhile, the enhanced C-S vibrational signal from the presence of short-chain sulfur fragments transiently adsorbed at defect-rich carbon sites. This demonstrates that deep discharge can accumulate free $S_3^-$ ions in the electrolyte, resulting in the reconstruction of the SPAN structure.

During the charge process at around 2.0 V, the Raman signal in the range of 400-500 $cm^{-1}$ remained at high intensity, which corresponds to polysulfides ($Na_2S_x$, $2<x<6$)[95]. This indicates that the polysulfides do not reversibly oxidize back, and they are accumulating as soluble species consistently (Figure 4b and 4c). The soluble species can react with sodium at the subsequent discharge and show a new reduction peak around 2.0V in CV (Figure 1a). At the same time, compared to the initial discharge state, the Raman peak intensity at 460 $cm^{-1}$ (corresponding to sulfur-sulfur chain in SPAN) decreased significantly at the cut-off charge voltage (2.7 V) (Figure 4d). This result can further indicate that the sulfur-sulfur chain in SPAN cathode is unable to comprehensively reform in the charge process after deep discharge, which is due to the sulfur loss caused by accumulation and shuttle effect of $S_3$ ions in electrolyte. This behavior directly explains the evolution of the 2.2-2.4 V oxidation peak in CV (Figure 3). This peak corresponds mainly to the oxidation of surface-anchored intermediate-valence sulfur species, rather than soluble $S_3^-$. Under shallow discharge (higher than 1.0V), sulfur partially reduced and confined near the SPAN surface. Therefore, these species can be re-oxidized during charging, showing a distinct peak at 2.2-2.4 V. In contrast, most sulfur is converted into highly soluble $S_3^-$ species under deep discharge (lower than 1.0V), which dissolve into the ether electrolyte and undergo polysulfide shuttling. With continued cycling, the amount of polysulfides that remain at the cathode surface and are

electrochemically accessible for oxidation at 2.2-2.4 V gradually decreases and eventually becomes negligible. As a result, the 2.2-2.4 V peak progressively disappears with increasing discharge depth.

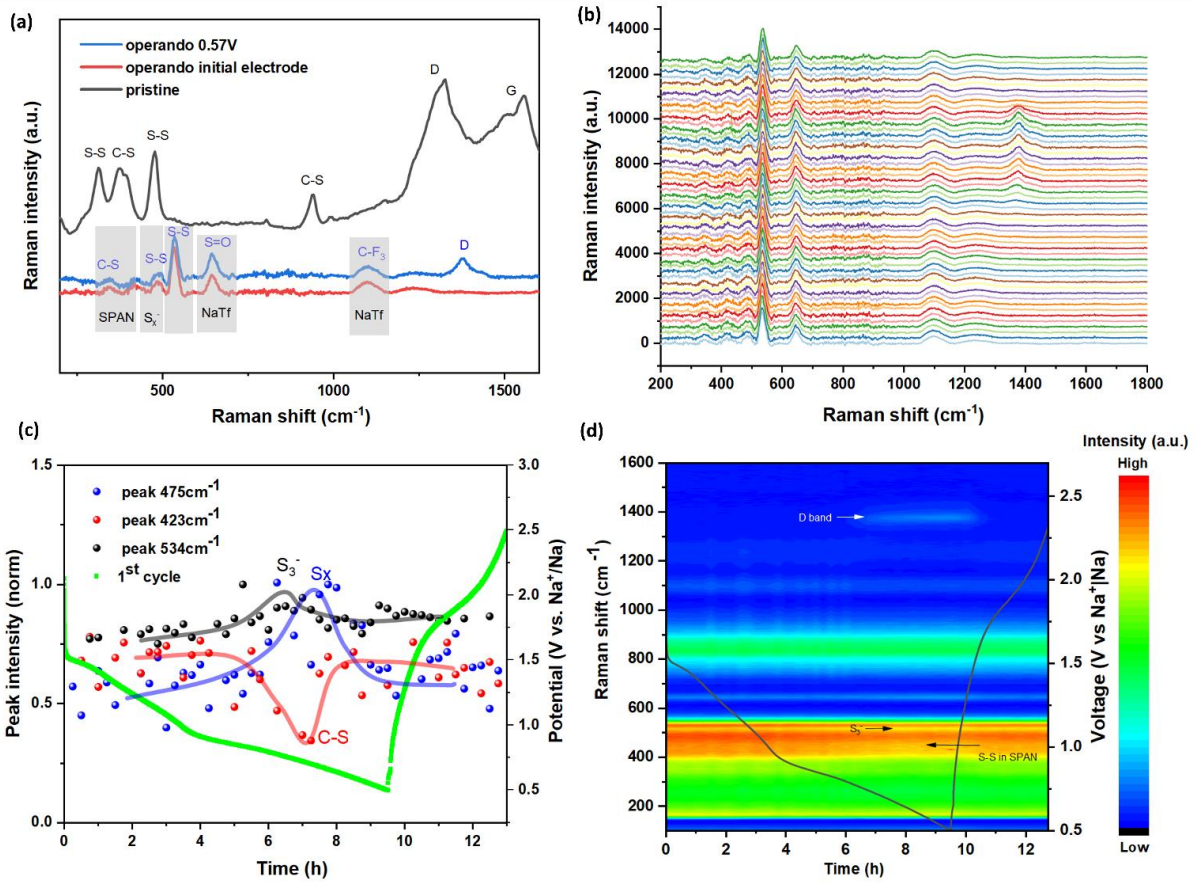


Figure 5.5 (a) Ex-situ Raman spectra of SPAN and in-situ Raman spectra of fresh SPAN cell/discharge at 0.57V, (b) Linear diagram of in-situ Raman spectra of SPAN cell during discharge-charge process between 0.5V to 2.7V (c) Raman peak intensity of C-S, $S_3^-$ and $S_x$ during charge-discharge between 0.5V-2.7V, (d) In-situ Raman spectra of SPAN cell during discharge-charge process between 0.5V to 2.7V.

**Galvanostatic charge-discharge observe in different potential windows**

Galvanostatic charge and discharge cycles were performed between 0.5V and 2.7V, and the curves are shown in Figure 5.6a. After a few cycles between 0.5V and 2.7V, the SPAN electrode shows an abnormal plateau at around 2.0-2.2V, unable to continue rising, indicating

a probable internal micro-short cut due to local dendrite formations. This could be due to the large amount of irreversible polysulfides formed at such low potential, which could shuttle to the sodium anode where they react[48]. This may consequently cause a large amount of sodium sulfide to cover and block the sodium surface and therefore causing local inactivity of the sodium anode. In this situation, the current cannot be evenly distributed on the surface of the sodium electrode, and it will only accumulate on the sites where sodium is not covered by sodium sulfide. This also means that the current is locally higher and the probability of dendrite growth at these sites is much higher. The uneven distribution of current leads to easier dendrite growth, which can cause the occurrence of micro short circuits and therefore impossibility to charge[98].

On this basis, the charging step was stopped and the current reversed. After discharge, the electrode can undergo further cycling, pointing towards the partial dissolution of the Na dendrites. This indicates that although the sulfur chain in SPAN electrode is hard to reform after deep discharge, the structure of PAN skeleton has not been completely destroyed: when the discharge depth becomes shallower, the polysulfides accumulated in the electrolyte are consumed during charging and the sulfur chains in SPAN can be partially reformed. This result is consistent with the CV showing that the oxidation peak around 2.0V to 2.2V reappears after recovering from low to high voltage. (Figure 5.6b). However, with repeated deep charge discharge processes, shuttle effect and the regeneration of soft sodium dendrites may occur again, resulting in the observed abnormal charging curves at around 2.0V (Figure 5.6b).

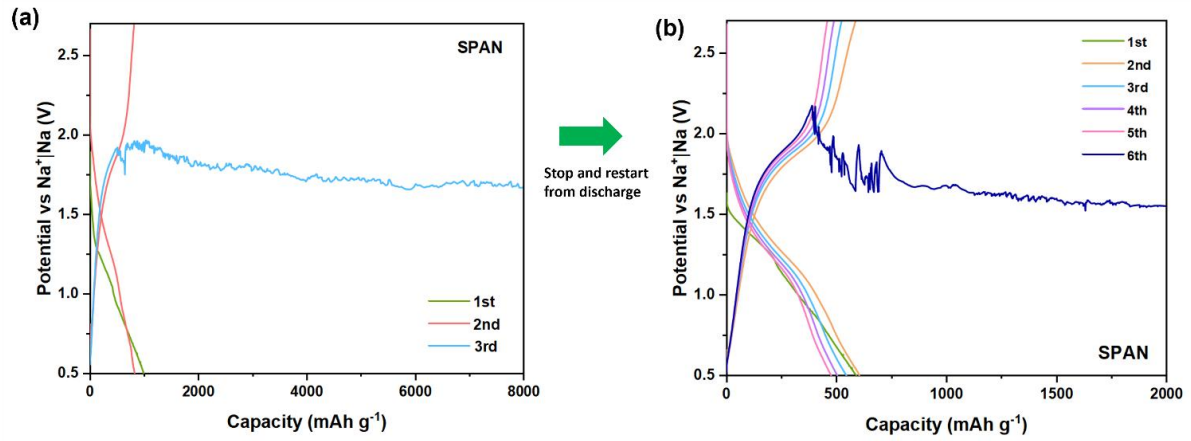


Figure 5.6 (a) Charge-discharge curve of SPAN cell between 0.5-2.7V, (b) Charge-discharge curve of SPAN cell between 0.5-2.7V after abnormal charge. (Electrolyte: 1M $NaCF_3SO_3$ in TEGDME, sulfur loading=0.8-1 mg $cm^{-2}$)

In order to avoid effects due to the deep discharge, a fresh SPAN electrode was cycled between 1.4V and 2.7V and the results are shown in Figure 5.7. In the first discharge, the SPAN electrode delivers 315mAh $g^{-1}$ at a specific current of 500 mA $g^{-1}$, but it only exhibits a capacity of about 50 mAh $g^{-1}$ during the first charge, a value which remains stable in subsequent cycles. This result indicates that when the lower potential cut off is limited to 1.4V, a part of reaction is strongly irreversible that make capacity decay between first and second cycle, and the conversion of short chain polysulfides to sodium sulfide is incomplete, which obviously lead to a drastic decrease in capacity [99]. This result indicates that even if the reduction of the potential window may improve the electrode stability, this has the drawback of very low capacity.

In another experiment, the SPAN cell in Figure 5.6, which was first pre-cycled between 0.5V and 2.7V at 500mA $g^{-1}$ for 9 cycles (and shown abnormal charge curve due to the soft dendrites), was further cycled in the restricted voltage range between 1.4V and 2.7V at 500 mA $g^{-1}$ (Figure 5.8c-5.8d). This pre-cycled cell shows now stable and reversible charge-discharge curves in the range 1.4V-2.7V at different current density. This further supports the

conclusion that the dissolution of sodium micro dendrites during the discharge process can alleviate micro short circuits; moreover, avoiding a deep discharge can effectively prevent the formation of irreversible polysulfide products and the occurrence of sodium dendrites. Furthermore, this pre-cycled cell delivers higher capacity than the cell cycled directly between 1.4V and 2.7V. This could be ascribed to the fact that polysulfide accumulated in electrolyte at low potential can participate in subsequent reactions providing capacity. This is consistent with the conclusion that polysulfides accumulated during deep discharge can be partially reversed during the charging process. It is worth noting that the cells precycled between 0.5V-2.7V has coulombic efficiency (CE) closer to 100% during the first 10cycles between 1.4V-2.7V, while the cell without pre-cycled has CE about 110%. This can be due to the irreversible reactions already occurred during pre-cycled. This kind of pre-irreversible reactions can help to reach more reversible reactions during subsequent cycles, which can be observed from CE of $10^{th}$ cycle to $20^{th}$ cycle and $30^{th}$ cycle to $40^{th}$ cycle. During the range of $10^{th}$ cycle to $20^{th}$ cycle, the cell without pre-cycled has CE about 102%, and during the range of $30^{th}$ cycle to $40^{th}$ cycle, the cell without pre-cycled has CE about 107%. This result can indicate irreversible reaction in each cycle, while the cell with pre-cycled has CE about 100% in above two ranges(Figure 5.7e) [10].

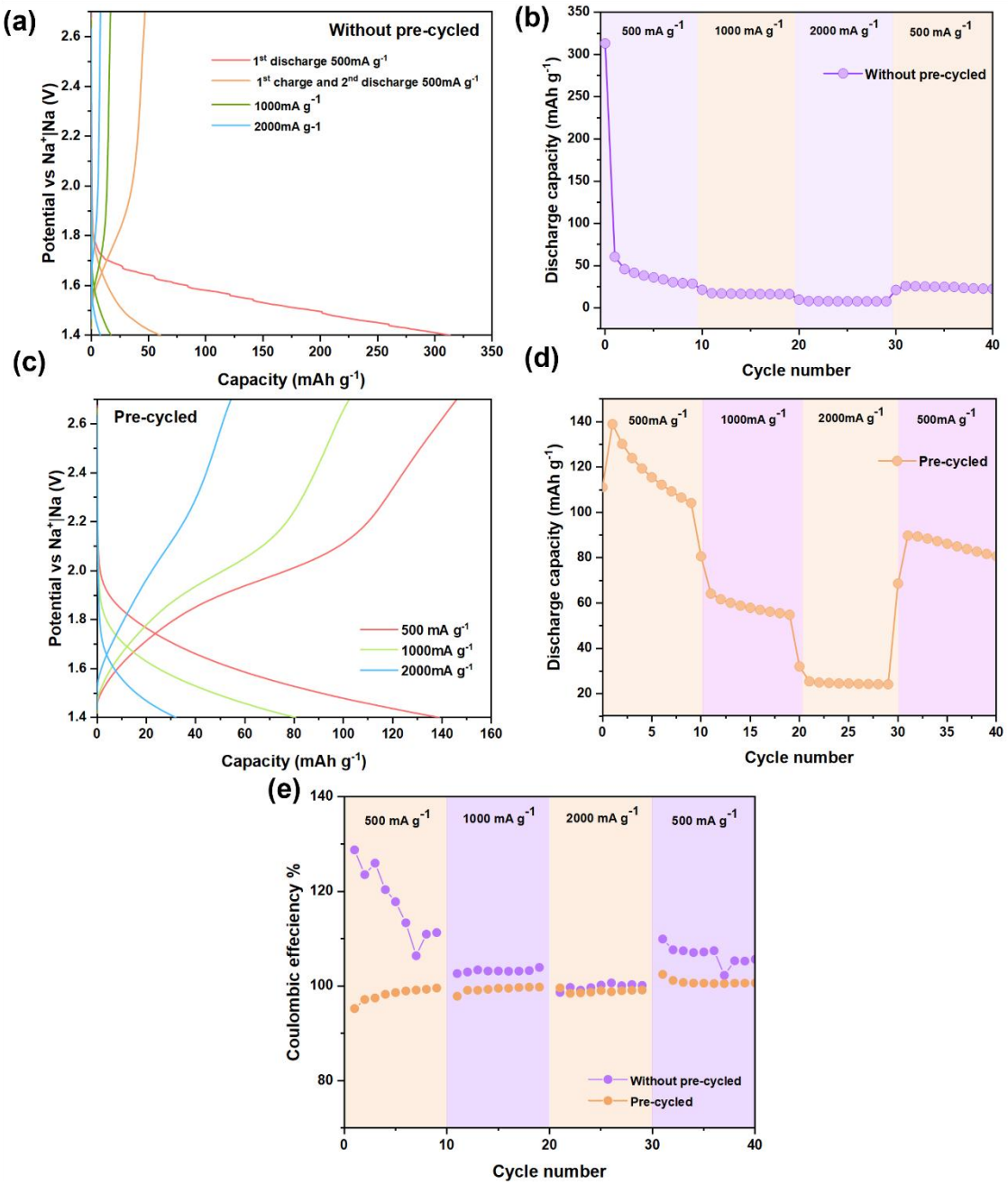


Figure 5.7 Electrochemical performance of SPAN between 1.4V to 2.7V (a) Charge-discharge curve of cell without pre-cycling , (b) Rate performance of cell without pre-cycling , (c) Charge-discharge curve after pre-cycled between 0.5V to 2.7V for 9 cycles at 500 mA $g^{-1}$, (d) Rate performance after pre-cycling between 0.5V to 2.7V for 9 cycles at 500 mA $g^{-1}$.(e) Coulombic efficiency of SPAN cell with/without pre-cycling in rate performance test. (Electrolyte: 1M $NaCF_3SO_3$ in TEGDME, sulfur loading=0.8-1 mg $cm^{-2}$)

**Electrochemical Performance Comparison in Reasonable Cut-off Voltage**

Considering the previous experiments, where we observed that deep discharge to 0.5V may be detrimental, and a too shallow discharge down to 1.4 V does not provide enough capacity, in the next experiments we decided to cycle the cell between 1.2V-2.7V and compared the SPAN electrode with elemental sulfur cathode (sulfur loading=1mg $cm^{-2}$, carbon content=30%, prepare by slurry coating). The cells have been cycled at currents between 500mAh $g^{-1}$ to 2000mAh $g^{-1}$. Clearly the SPAN electrode delivers higher capacity at all currents (Figure 5.8a) and longer stability (Figure 5.8b) than sulfur cathode probably due to the conjugated structures in SPAN, and the short sulfur chain. The initial capacity of the SPAN electrode is 550mAh $g^{-1}$ at first cycle at 500 mA $g^{-1}$ and it decays to 250 mAh $g^{-1}$ at the second cycle. After 100 cycles, 200 mAh $g^{-1}$ of capacity is retained the comparison of the coulombic efficiency (Figure 5.8c) further proves that SPAN can provide a more reversible sulfur conversion reaction by reasonable selection of potential window, and the short-chain sulfur in SPAN can prevent the generation of long-chain polysulfides.

The SPAN//Na cell has a coulombic efficiency at around 99.86% during first 20 cycles and stay at 100% during last 80 cycles at 500mA $g^{-1}$. In contrast, the coulombic efficiency of the sulfur cathode is only 60%-80%. This is because the shuttle effect caused by the polysulfides inside the cell cause continuous loss of sulfur[100]. At the same time, the electron transfer on the cathode side may be hindered by the insulating properties of sulfur (carbon content is 30%, same as SPAN cathode), resulting in high polarization and low reversibility of the cell [101]. Compared with sulfur, SPAN cathode have high conductivity as $10^{-4}$ S/cm, which is much higher than conductivity of sulfur cathode that is $10^{-30}$ S/cm.[102] [103]Such high conductivity can[104] reduce the polarization of the cell and improve the reversibility of the reaction between sulfur and sodium[105].

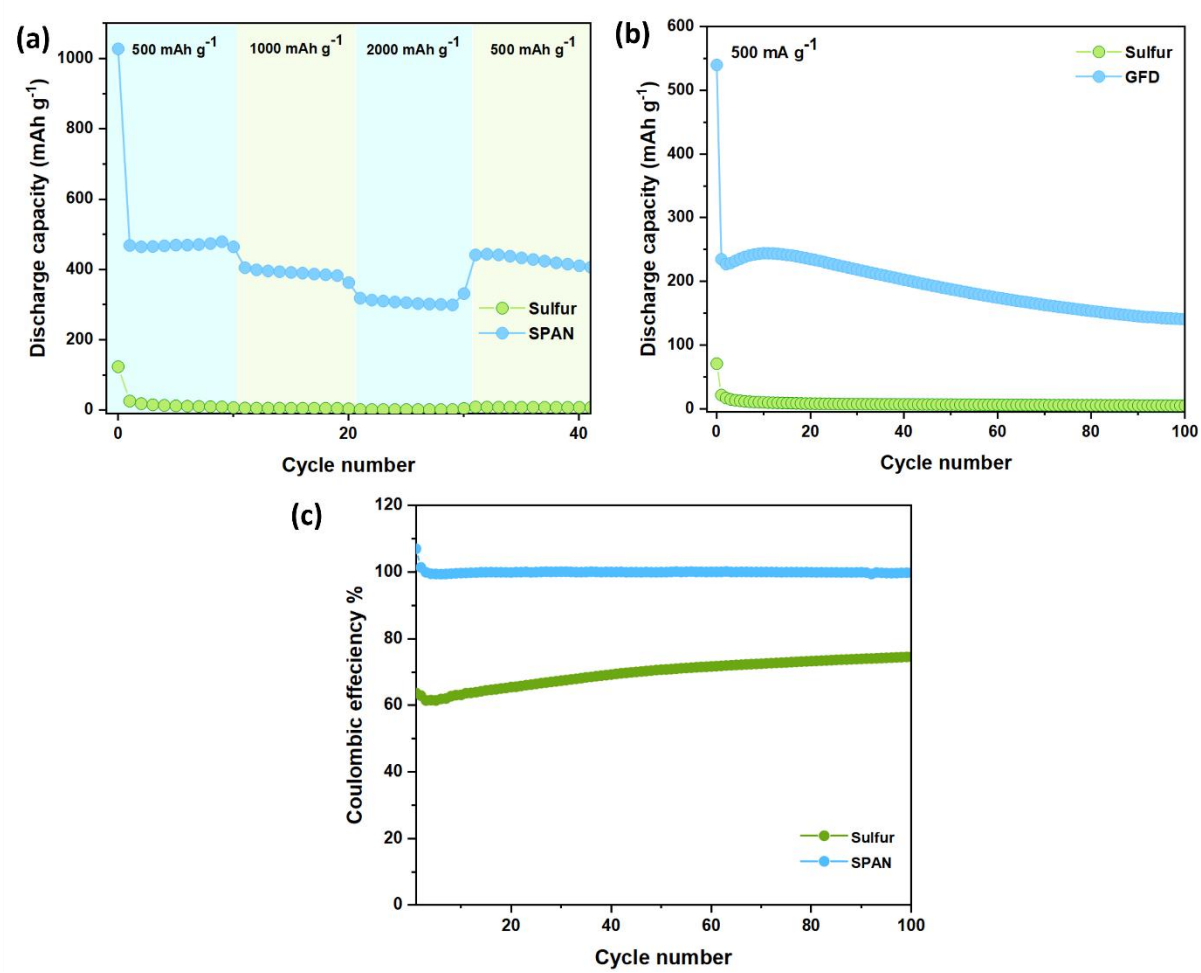


Figure 5.8 (a) Rate performance of cell with SPAN and sulfur cathode, (b) long cycling performance at 500 mA $g^{-1}$ of cell with SPAN and sulfur cathode.(c) Coulombic efficiency of SPAN and sulfur. (Electrolyte: 1M $NaCF_3SO_3$ in TEGDME, capacity is calculated by sulfur content of cathode, sulfur loading=0.8 mg $cm^{-2}$).

Figure 5.9 shows the charge-discharge curve of SPAN and sulfur. During the discharge process, the sulfur cathode exhibits a typical dual-platform feature, with the two platforms corresponding to the $Na_2S_8$ →$Na_2S_6$/$Na_2S_4$ conversion process and the $Na_2S_4$→ $Na_2S_2$/$Na_2S$ conversion process, respectively[106]. In contrast, the SPAN cathode only exhibits a sloped curve, which indicates a one-step reaction without phase transitions rather than the $Na_2S_8$ →$Na_2S_6$/$Na_2S_4$ conversion process: the short-chain polysulfides are directly converted into sodium sulfide by solid-state transformation [107]. During the charging process, the sulfur

cathode exhibits a charging capacity far exceeding the discharge capacity, which is due to the overcharge effect caused by the polysulfides[108]. At the same time, the high potential difference between the charge and the discharge curves indicates the high cell polarization[109]. In contrast, the SPAN cathode exhibits a charging capacity that is almost the same as the discharge capacity, proving the orderly and highly reversible sulfur-sodium conversion reaction, and much lower polarization[110]. However, one drawback is that the average voltage of the SPAN//Na cell is generally lower than that of sulfur//Na cell, which leads to lower energy density.

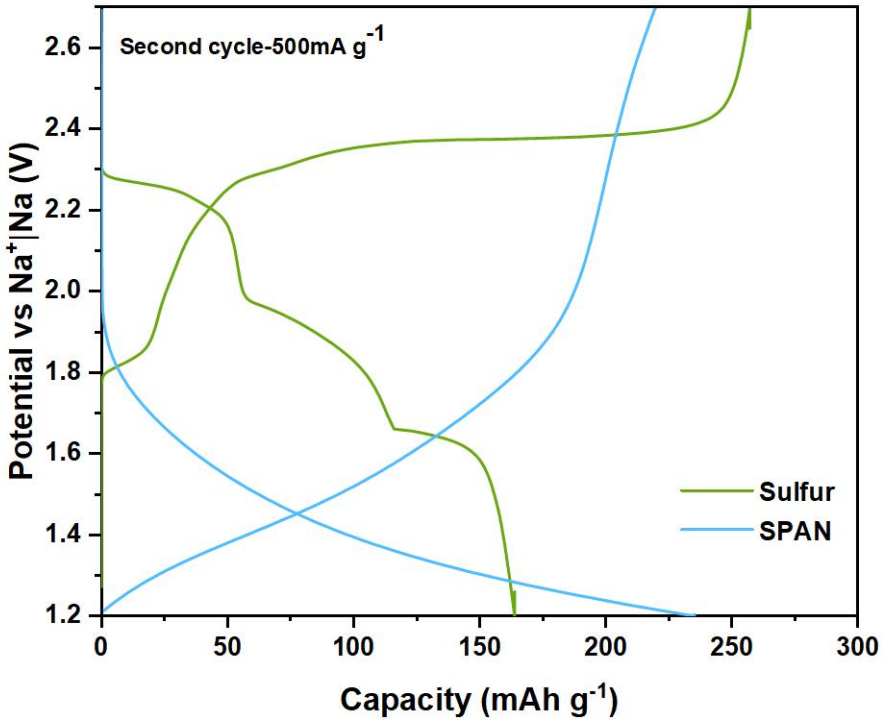


Figure 5.9 Charge-discharge curve of sulfur and SPAN (Electrolyte: 1M $NaCF_3SO_3$ in TEGDME, sulfur loading=0.8-1 mg $cm^{-2}$)

Figure 5.10 shows the Raman spectra of fresh SPAN electrode and a SPAN electrode after two cycles and four cycles between 1.2V-2.7V. Two Raman peaks can be observed at 297$cm^{-1}$ and 372$cm^{-1}$, which belong to the C-S bond in SPAN[111], [112]. Meanwhile, the Raman peak observed at 470$cm^{-1}$ belongs to the S-S bond in SPAN[113]. After two complete charge-discharge cycles (ending at 2.7V), the Raman signal intensity of C-S and S-S bonds

decreased, indicating that the reformation of C-S and S-S bonds is not completely reversible in the first cycle[114]. Then the cell cycled for two cycles was compared with the cell after four complete charge-discharge cycles, and the signal strength of the C-S bond and the S-S bond remained. This indicates that under shallow discharge conditions (1.2 V), the absence of significant S3- accumulation prevents sulfur loss through polysulfide shuttling. As a result, the C-S and S-S signals remain well preserved after cycling.

Further investigation on the structural evolution of SPAN between 1.2V to 2.7V is based on in-situ Raman spectroscopy. As shown in Figure 5.11b, the D-band signal near 1350 $cm^{-1}$ did not exhibit any noticeable enhancement throughout the charge–discharge process, suggesting that the carbon backbone of SPAN remained structurally stable. Moreover, no obvious enhancement of the signal associated with $S_3^-$ species was observed at end of discharge (1.2V), which is distinct from the behavior typically seen during deep discharge to 0.5 V (Figure 5.11b).

To further optimize the SPAN//Na cell, carbon modified functional separator (as a polysulfide blocking layer) was implemented and discussed in the next section.

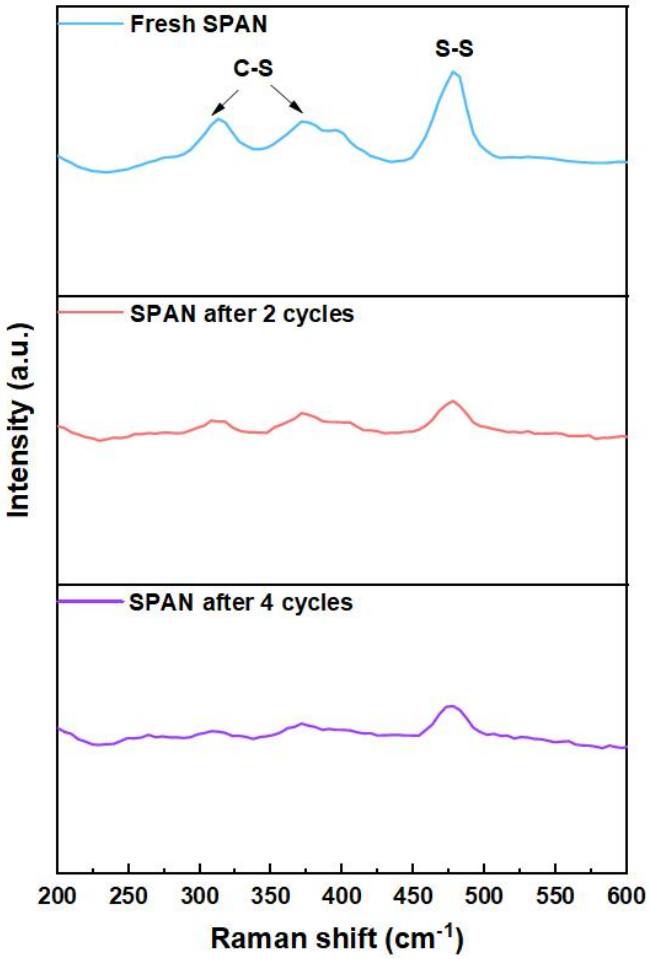


Figure 5.10 *Ex-situ* Raman spectra of SPAN positive electrodes: fresh, after 2 cycles, and after 4 cycles.

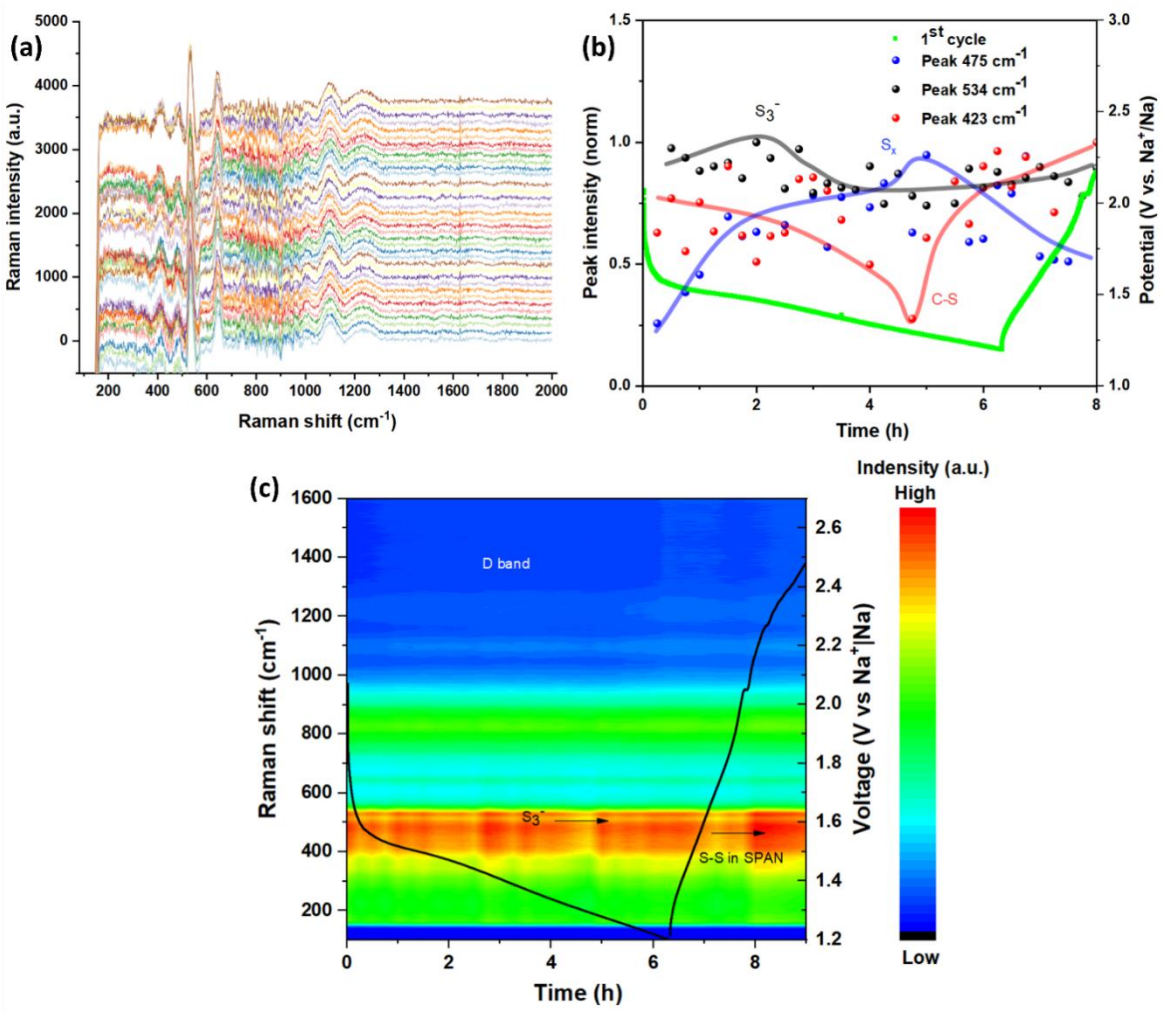


Figure 5.11 (a) Linear diagram of *in-situ* Raman spectra of SPAN cell during discharge-charge process between 1.2V to 2.7V, (b) Raman peak intensity of C-S, $S_3^-$ and $S_x$ during charge-discharge between 1.2V-2.7V, (c) *In-situ* Raman spectra of SPAN cell during discharge-charge process between 1.2V to 2.7V

**Application of functional separator to improve capacity retention**

Carbon functional separator with high specific surface area and porous structure can inhibit shuttle effects by physically adsorbing and confining soluble polysulfides[115], [116]. Moreover, it can provide an electron transport path for the positive electrode, thereby accelerating the conversion reaction kinetics and improving the utilization rate of active materials[117]. For this research, C65 was used as functional carbon layer for separator, which has high surface area ($62 m^2/g$) and high conductivity[72]. To exclude contribution to

the capacity by the carbon layer (C65:LA133=7:3 in mass ratio) applied to the separator, electrochemical tests have been performed by sandwiching the separator between an Al current collector and the Na counter electrode. The carbon layer of the separator is directly contacting the Al current collector. As shown in Figure 5.12, it can be seen that C65 | Na cell only deliver 0.045 mAh $g^{-1}$ capacity at 500 mA $g^{-1}$ and rapidly decay to 0.03 mAh $g^{-1}$ during charging and this proves there is no additional capacity coming from the material coated on the functional separator.

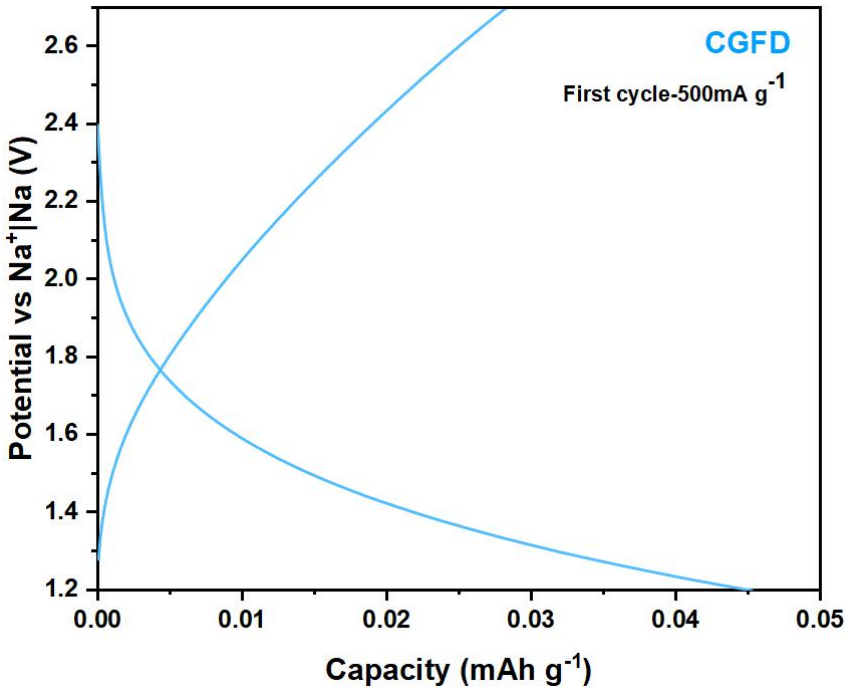


Figure 5.12 Charge-discharge performance of C65//Na Cell (Electrolyte: 1M $NaCF_3SO_3$ in TEGDME)

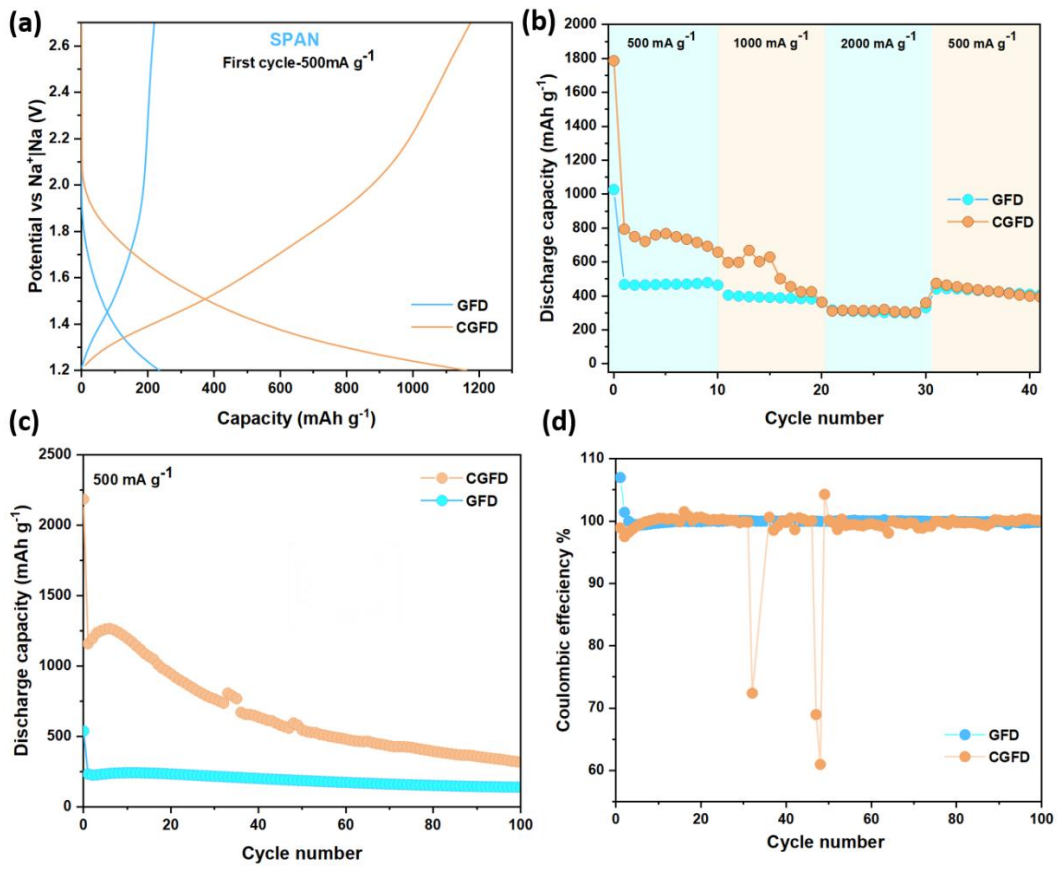


Figure 5.13 (a) Charge-discharge curve of SPAN//Na cell with CGFD and GFD, (b) Rate performance of SPAN//Na cell with CGFD and GFD separators, (c) long cycle performance of SPAN//Na cell with CGFD and GFD. (d) Coulombic efficiency of SPAN//Na cell with CGFD and GFD. (Electrolyte: 1M $NaCF_3SO_3$ in TEGDME, capacity is calculated by sulfur content of cathode, sulfur loading=0.8-1 mg $cm^{-2}$).

Figure 5.13a shows the charge and discharge curves of SPAN with CGFD separator and GFD separator at 500 mA $g^{-1}$. The cell with CGFD separator shows higher capacity. The SPAN with CGFD separator delivers reversible capacity 1202 mAh $g^{-1}$ at first cycle at 500mA $g^{-1}$, which indicates that CGFD separators can significantly inhibit shuttle effect to of the cell to improve the capacity.

Figure 5.13b shows the significantly improved rate performance of the cell containing the CGFD separator. The cell with CGFD-based cell exhibits specific capacities of 1787, 598, and 318 mAh $g^{-1}$ at 500mAh $g^{-1}$, 1000mAh $g^{-1}$, and 2000mAh $g^{-1}$. At the same time, it also

shows 474 mAh $g^{-1}$ after cycling under different rate, which reflects the help of CGFD separator in impeding the shuttling.

The two cells were compared in terms of long cycling stability at 500 mA $g^{-1}$. The cell with CGFD separator shows high capacity of 2186 mAh $g^{-1}$ at first cycle and can get higher capacity than cell with GFD separator after 100 cycles. Nevertheless, the capacity with the modified separator decays faster than cell with GFD. Apparently, the CGFD separator can help in the initial cycles, but is not suitable for a stabilization of the electrochemical reaction between SPAN and sodium. Same conclusion can be proved by CE. Figure 5.13d shows the coulombic efficiency (CE) of cells with CGFD separator and GFD separator. Compared to the GFD cell, the CGFD cell exhibits CE of 98.92% at first cycle, and then increases to 100% after 5 cycles. At the $32^{nd}$ cycle, the CE suddenly decreases to 72.42%, and back to 100% at $33^{rd}$ cycle. The same sudden decrease can be observed at $44^{th}$ and $48^{th}$ cycle. This can indicate side reactions that happened in the cell with CGFD and the application of carbon functional separators still needs to be optimized.

### 5.1.3 Conclusion

This study proved the electrochemical performance of sulfurized polyacrylonitrile (SPAN) as a positive electrode material for room temperature sodium sulfur batteries with ether-based electrolytes under high current density. In ether-based electrolytes, deep discharge (i.e., down to 0.5 V) can lead to accumulation of $S_3^-$. This accumulation exacerbates the shuttle effect and the generation of non-active sites on the sodium negative electrode, which leads to uneven current distribution at the negative electrode interface. Uneven current distribution can lead to easier growth of sodium dendrites, resulting in the occurrence of micro short circuits in the cell. This conclusion indicates the necessity of avoiding deep discharge in SPAN-sodium cells. However, it should be noted that a much higher cut-off voltage is not necessarily better, and a reasonable cut-off voltage should be chosen. Excessively high cut-

off voltage (such as 1.4V) can lead to incomplete sulfur-sodium reaction, resulting in a significantly lower capacity. According to our findings, the most suitable discharge cut-off voltage is 1.2V, which helps avoiding micro short circuits and generation of a large amount of polysulfides. As a further improvement, carbon functional separators can help SPAN electrodes to achieve higher capacities due to confinement of the reduced species to the cathode side of the cell. However, although a positive effect of the functional separator has been observed in the initial cycles, further optimization is required to achieve better stability over longer cycles.

**Authorship Contributions**

The conceptualization and design of the experiments were primarily developed by Liwen Yang under supervision of Prof. Dr. Sonia Dsoke and Prof. Dr. Hatice Mutlu. The synthesis of SPAN materials, cell assembly, and electrochemical testing were performed by Liwen Yang in IAM-ESS of Karlsruhe Institute of Technology. Structural characterizations (XRD and elemental analysis) were conducted and analyzed by Liwen Yang with technical support from IAM-ESS. *In-Situ* Raman test was provided by Dr. Rong Li with technical support from Guizhou University. *Ex-situ* Raman test was provided by Prof. Dr. Hatice Mutlu and Bercis Pektas with technical support from Mulhouse University. Liwen Yang prepared the manuscript draft, and it was revised under the supervision of Prof. Dr. Sonia Dsoke, Prof. Dr. Hatice Mutlu and Bercis Pektas.

## 5.2 Failure Mechanisms of Nitrogen-Rich Sulfurized Polyamides as Cathodes for Room-Temperature Na-S Batteries

### 5.2.1 Introduction

In the previous chapter, a reasonable discharge-charge potential of SPAN is proved in ether-based RT Na-S cells and enhanced capacity and stability by functional separator. The result indicates that SPAN needs optimization in stability and does not effectively inhibit the shuttle effect in polymer structure. Based on the understanding that polar functional groups can anchor polysulfide to enhance stability, this chapter reports on the investigation of sulfur rich polyamides that have not yet been used in Na-S batteries and have more polar functional groups than SPAN that can anchor polysulfides.

Sulfur-rich polyamides (S-PAs) constitute a subclass of polyamide (PA) materials distinguished by their high sulfur content. Polyamides are typically synthesized via the condensation polymerization of amino acids or their derivatives. Sulfur-rich polyamides are obtained by incorporating sulfur-containing monomers, such as dithiodicarboxylic acids or dithioamino acids into the polymer backbone, thereby introducing sulfur chains with tunable lengths and adjustable sulfur atom ratios.

S-PAs are polymers, suitable to test the research hypothesis, that flexible polyamide frameworks provide abundant polar functional groups (such as amide-CONH- units) that can chemically interact with polysulfide intermediates, further enhancing their immobilization and redox reversibility[118]. Moreover, S-PAs incorporate sulfur atoms covalently into the polymer backbone through C-S or S-S linkages. This structural feature effectively confines sulfur species within the polymer matrix, thereby to suppress the dissolution and migration of soluble polysulfides[119].

Moreover, S-PAs offer excellent molecular design flexibility, allowing the chemical composition and structure to be tailored to specific requirements. For example, this includes

tuning the sulfur content, adjusting polymer chain length, and optimizing the distribution of sulfur-carbon bonds [120]. Such structural tunability provides a versatile platform for optimizing capacity, cycling stability, and reaction kinetics in sodium-sulfur batteries. However, while polar nitrogen-containing groups are generally regarded as beneficial anchoring sites for polysulfides, their intrinsic chemical stability under strongly reducing polysulfide environments has not been systematically examined. In particular, soluble polysulfide species are strong nucleophiles, and their potential to attack electrophilic amide functionalities may trigger irreversible structural rearrangements within the polymer backbone, thereby compromising structural reversibility. Despite the widespread use of nitrogen-rich sulfur polymers, experimental evidence clarifying whether such nitrogen functionalities act as stabilizing anchors or reactive degradation sites remains limited.

In this study, a sulfur-rich polyamide (**P1)** was synthesized via inverse vulcanization approach. The polymer is decorated with abundant C=O groups, amide functionalities and a covalently cross-linked sulfur network. Rather than presuming purely beneficial anchoring effects, this work examines the chemical evolution of these nitrogen-rich environments during electrochemical cycling. **P1** was evaluated as a cathode material in room-temperature (RT) Na-S batteries using an ether-based electrolyte (i.e.,1M $NaCF_3SO_3$ in TEGDME). The electrochemical response, structural evolution, and failure mechanism of **P1** were systematically analyzed to elucidate irreversible degradation pathways associated with reactive nitrogen sites in sulfurized polymer cathodes. Although high sulfur utilization is often reported for sulfurized polymer systems, the present material is intentionally investigated as a model amide-rich network to critically evaluate the chemical stability of such functionalities under strongly reducing Na–S conditions.

### 5.2.2 Result and Discussion

**Synthesis and Characterization of P1**

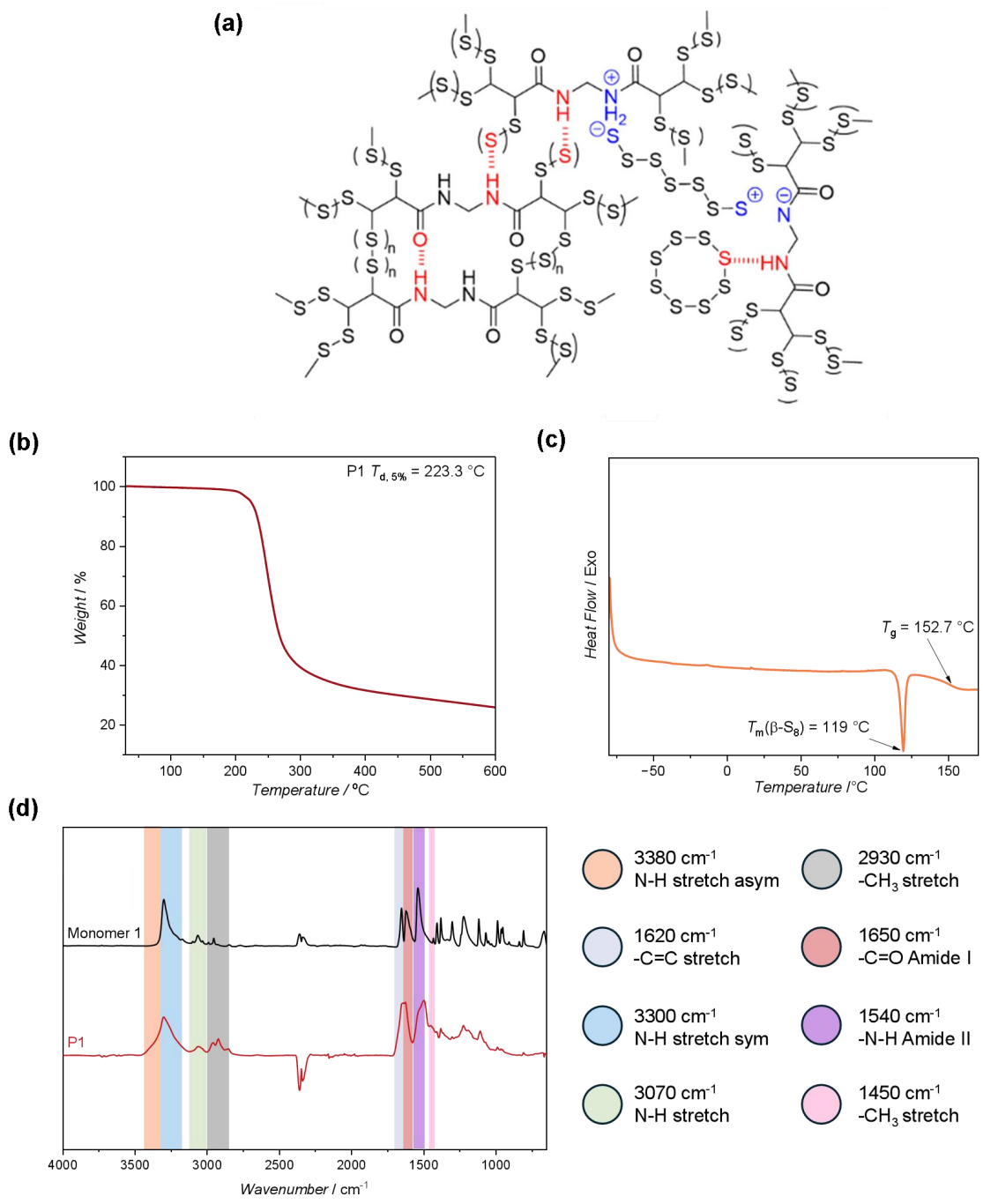


Figure 5.14 (a) Structural schematic of **P1** polymer, (b) TGA curve of **P1**, (c) DSC curve of **P1**, (d) FT-IR of **P1**

**P1** polymer consists of a carbon-based backbone with multiple heteroatom-containing functional groups, including amide (-CONH-) and amine (-NH-) type moieties (Figure 5.14a).

The presence of both sulfur and nitrogen atoms in conjugated and adjacent positions suggests the possibility of extensive intramolecular interactions, such as hydrogen bonding and charge delocalization. The incorporation of sulfonyl and thiocarbonyl functionalities introduces electron-withdrawing structural elements, while the amine and amide groups contribute to potential coordination or redox-active sites. The combination of C=O, N–H, and C–S/S–S linkages create a highly polar local environment, which may affect both $Na^+$ coordination and polysulfide adsorption energetics. The covalent bonding between sulfur and nitrogen within the polymer matrix provides molecular confinement of sulfur species, which may influence polysulfide evolution during cycling. Given the sulfur content of 63 wt% (vide infra), the polymer contains a high density of electrochemically addressable sulfur units relative to the organic backbone. Furthermore, the partially conjugated backbone of the polymer may contribute to structural rigidity during electrochemical cycling; however, no direct electronic conductivity measurement was performed, and therefore intrinsic charge transport remains dominated by the conductive carbon additive in the composite electrode.

The thermogravimetric analysis (TGA) thermogram of the **P1** shows a single-step weight-loss process, with the 5% weight-loss temperature ($T_d$, 5%) occurring at 210 °C (Figure 5.14b). The sharp decrease in mass between 200 and 300 °C is attributed to the thermal decomposition of sulfur-chains within the polymer. Assuming complete volatilization of free and weakly bound sulfur in this region, the calculated sulfur content of 63 wt% corresponds to a theoretical specific capacity of approximately 1040 mAh $g^{-1}$ (based on full conversion of sulfur to $Na_2S$, 1675 mAh $g^{-1}$ for sulfur, adjusted for sulfur fraction). The residual mass above 400 °C remains nearly constant, indicating that the non-sulfur carbonaceous backbone is thermally stable in this temperature region.

The DSC curve of **P1** displays two major thermal features (Figure 5.14c). First, a prominent endothermic peak appears at 119 °C, which is attributed to the melting of residual β-$S_8$

crystalline phase. indicating that a fraction of elemental sulfur remains physically embedded rather than fully chemically crosslinked. The presence of residual crystalline sulfur suggests incomplete inverse vulcanization and may contribute to initial electrochemical activity followed by rapid depletion. A glass transition temperature ($T_g$) at approximately 149 $^oC$ is observed, indicating restricted segmental mobility and a relatively rigid crosslinked structure. [121]. The comparatively high $T_g$ is consistent with a densely crosslinked sulfur–organic network, which may mechanically suppress large-scale volume changes but does not necessarily prevent molecular-level sulfur chain scission during electrochemical cycling.

The FT-IR spectra of the **P1** exhibit several characteristic absorption bands that confirm the presence of nitrogen-containing functional groups and the polymeric backbone structure (Figure S2d). Broad N–H stretching bands appear at3380 $cm^{-1}$ and 3300 $cm^{-1}$ , with an additional feature at 3070 $cm^{-1}$ [122]. The peak at 2930 $cm^{-1}$ is attributed to the C-H stretching of aliphatic -$CH_3$ groups [123]. In the fingerprint region, the spectrum displays a distinct absorption at 1650 $cm^{-1}$, assigned to the C=O stretching (amide I) [124], accompanied by a band at 1540 $cm^{-1}$ associated with N-H bending coupled with C-N stretching (amide II) [125]. Meanwhile, the signal at 1620 $cm^{-1}$ corresponds to C=C stretching, indicating the retention of conjugated or aromatic structural segments [126]. The absorption at 1450 $cm^{-1}$ arises from $CH_3$ stretch[127]. Notably, no distinct crystalline sulfur vibration dominates the spectrum, supporting that the majority of sulfur is covalently integrated rather than present as bulk $S_8$. These characteristic peaks verify the successful incorporation of amide functionalities and the expected polymer framework within **P1**.

**Electrochemical Behavior of P1**

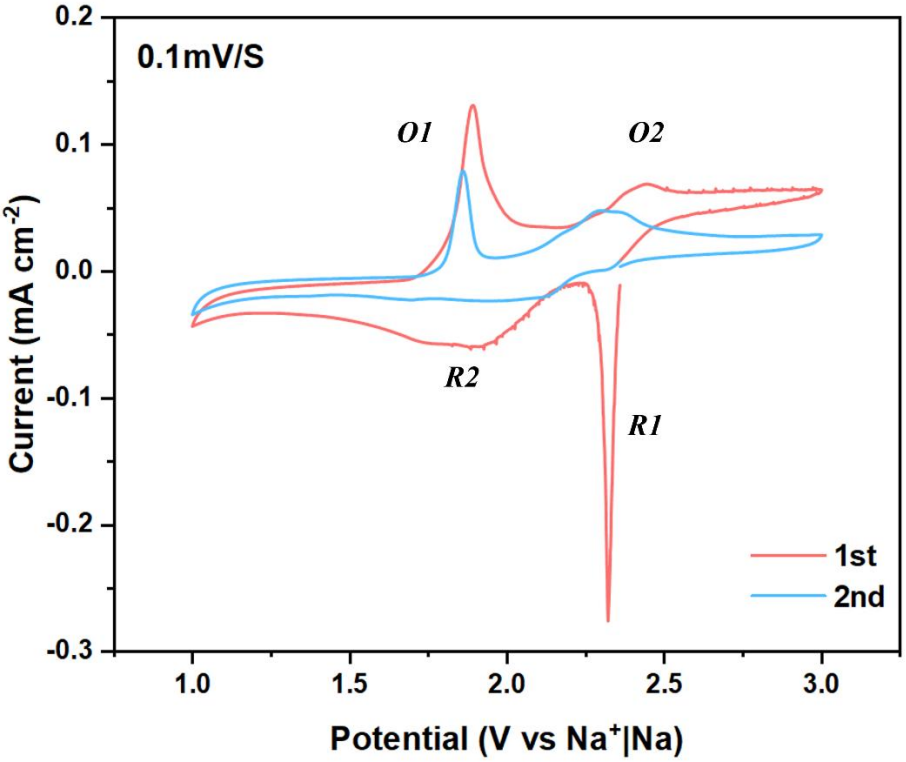


Figure 5.15 CV curve of cell with **P1** positive electrode (Three electrodes cell with working electrode: **P1**, counter electrode: sodium, reference electrode: sodium. Electrolyte: 1M $Na_2CF_3SO_3$ in TEGDME).

Cyclic voltammetry (CV) was performed to investigate the redox behavior of **P1** in Sodium metal cells. As shown in Figure 1, the first cycle exhibits two reduction peaks and two oxidation peaks, which are characteristics of stepwise sulfur conversion in Na-S systems.

The reduction peaks can be attributed to the sequential conversion of covalently bound sulfur species to soluble sodium polysulfide intermediates and ultimately to short-chain sulfide species (e.g., $Na_2S_2$/$Na_2S$). During the subsequent oxidation process, these reduced sulfur species are partially re-oxidized to higher-order polysulfides and sulfur-like species within the polymer matrix.

However, significant changes in peak intensity and position are observed from the second cycle onward, indicating limited reversibility of the sulfur redox process. Notably, the disappearance or strong attenuation of redox peaks in subsequent cycles suggests rapid loss

of electrochemically active sulfur species, consistent with irreversible structural or chemical transformations within the polymer.

Notably, in the second reduction cycle, the oxidation-related peaks are no longer clearly resolved. This further supports that a fraction of the initially active sulfur species becomes electrochemically inaccessible after the first cycle. These observations point to substantial loss of reversible sulfur conversion during the initial sodiation process.

To further evaluate the stability of the redox process, galvanostatic cycling was performed.

## Galvanostatic Tests of P1

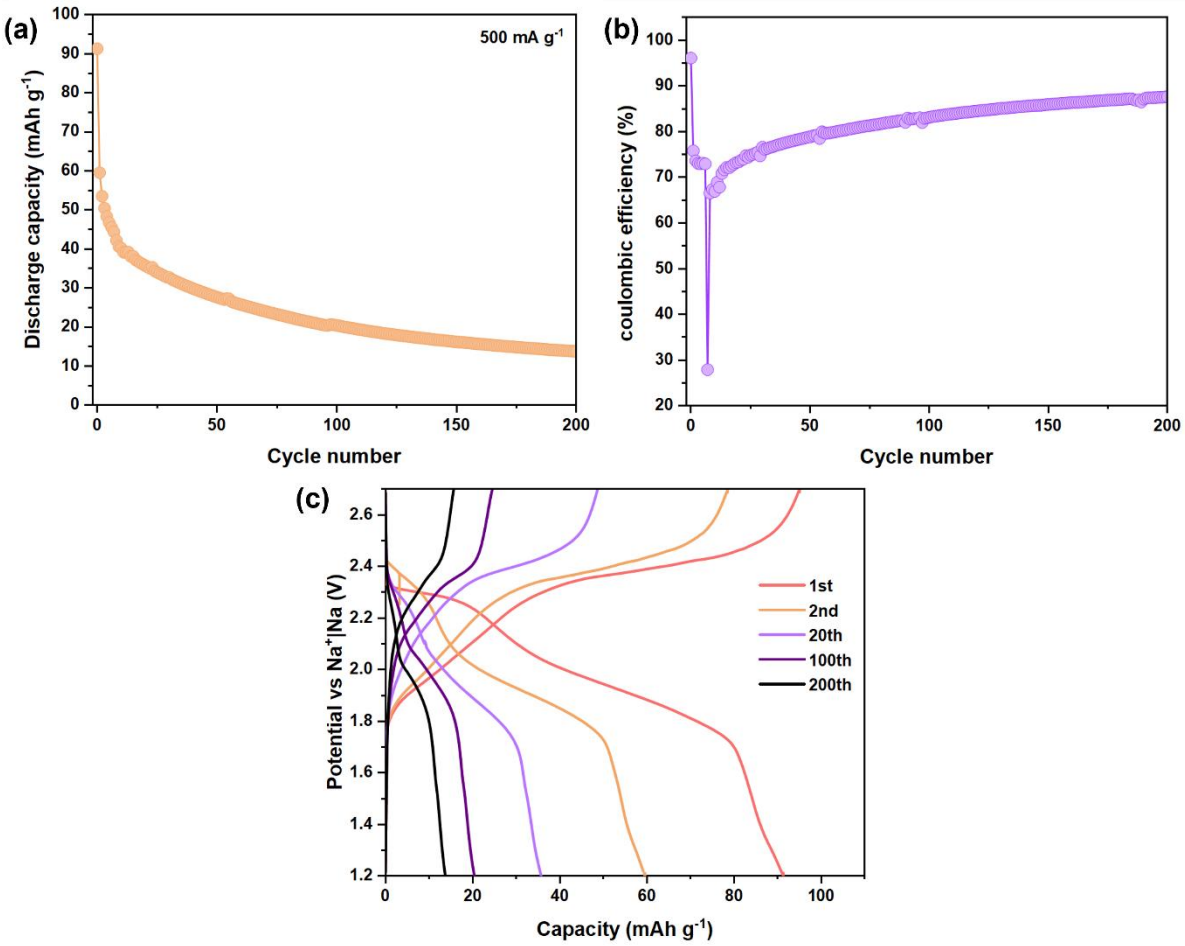


Figure 5.16 (a) Long cycle performance of cell with **P1** positive electrode, (b) Coulombic efficiency of cell with **P1** positive electrode, (c) Charge-discharge curve of cell with **P1** positive electrode (Electrolyte: 1M $NaCF_3SO_3$ in TEGDME, capacity is calculated by sulfur content of positive electrode, sulfur loading=0.8 mg $cm^{-2}$).

The initial discharge capacity is approximatively 90 mAh $g^{-1}$ at 500 mAh g-1 and it rapidly decreases within the first few cycles and progressively declines to circa 20 mAh $g^{-1}$ after 200 cycles (Figure 5.16a). This pronounced capacity decay indicates limited reversibility of the sulfur redox process and it is consistent with the attenuation of redox peaks observed in the CV measurements (Figure 5.15). The rapid loss of capacity during the initial cycles suggests that a substantial fraction of electrochemically active sulfur becomes inaccessible early during cycling.

While these capacity values are significantly lower than those reported for sulfurized polyacrylonitrile-based cathodes (480 mAh $g^{-1}$ at C/5), they provide insight into the distinct chemical instability of amide-containing sulfur networks in Na-S environment[92].

As shown in Figure 5.16b, the coulombic efficiency (CE) is approximately 96% in the first cycle, but decreases to ~ 75% at second cycle. In subsequent cycles, the CE gradually increases and stabilizes to 80-85% after prolonged cycling. A minor deviation in the CE was observed in an individual cycle (decrease to 28%), which is considered an outlier within experimental uncertainty. The subsequent cycles demonstrate a stable CE stabilization behavior. The initial drop in CE reflects substantial irreversible processes during early cycles, likely associated with loss of active sulfur species and parasitic side reactions. The gradual increase in CE at later stages may indicate that the majority of reactive sulfur species have already been consumed, leading to reduced shuttle-related losses. The charge-discharge profiles (Figure 2c) further illustrate the evolution of the redox behavior. In the first cycle, two distinct discharge plateaus can be observed at approximately 2.3 V and 1.7 V, which are characteristic of stepwise sulfur conversion reactions in Na-S systems. The corresponding charge curve exhibits broad oxidation features between 2.1-2.4 V, indicating partial reversibility of these processes. In the second cycle, these plateaus become less pronounced, reflecting diminished redox activity. From the 20th to the 80th cycle, both discharge and charge plateaus progressively fade, accompanied by continuous capacity decay. After ~100 cycles, the voltage profiles become increasingly sloped, and distinct redox plateau are no longer clearly resolved. Such behavior suggests transition from conversion-dominated (diffusion dominated) reactions toward more surface-limited or capacitive-like contributions [128]. By the 200th cycle, the remaining capacity is minimal and largely lacks characteristic sulfur redox features, indicating that the reversible sulfur conversion is largely suppressed.

To solve the above issues, $MoS_2$ functional separator was used to prevent the loss of sulfur, improve the reaction kinetic and help with the electron transfer by the metal sites. The $MoS_2$ functional separator retains its primary function as an electronic insulator, ensuring that no continuous electron-conductive pathways are introduced and thereby avoiding any risk of internal short-circuiting. The edge sites and defects of $MoS_2$ can reduce the reaction energy barrier for polysulfide conversion, accelerate the deposition of polysulfides to sodium sulfide ($Na_2S$), and the conversion of $Na_2S$ to polysulfides. At the same time, $MoS_2$ functional layer can improve the overall electron transfer efficiency of the electrode and make a fast reaction by electron conductivity of $MoS_2$[129]. In addition, the active sites on the $MoS_2$ surface (such as edge sites and sulfur vacancies) can form strong chemical bonds with polysulfides and inhibit the diffusion of polysulfides[130].

**Characterization of $MoS_2$ Functional Separator**

As described in Chapter 4.8.6, $MoS_2$ functional separators are obtained by loading $MoS_2$ with different morphologies obtained by ball milling onto the surface of glass fiber separator-D. Firstly, the obtained $MoS_2$ powder was characterized to evaluate its structural properties. XRD analysis was performed to investigate structural changes of the materials through the ball-milling process. As shown in Figure 5.17a, all diffraction peaks identified for $MoS_2$ confirm that the material has a hexagonal crystal structure (space group P63/mmc). After mechanical grinding, the 002 reflection exhibits significant broadening and a noticeable decrease in intensity. This result indicate a reduction in particle size and a decrease in the number of stacked $MoS_2$ layers, as the 002 reflection is associated with the interlayer stacking along the c-axis [131]. Among the samples, the $MoS_2$ after 45 hours ball milling shows broadening and attenuation of reflections, suggesting the highest level of $MoS_2$ sheet separation, and therefore highest surface area. Nevertheless, the overall crystallinity of $MoS_2$

is retained after intensive mechanical milling since the persistence of characteristic diffraction signals.

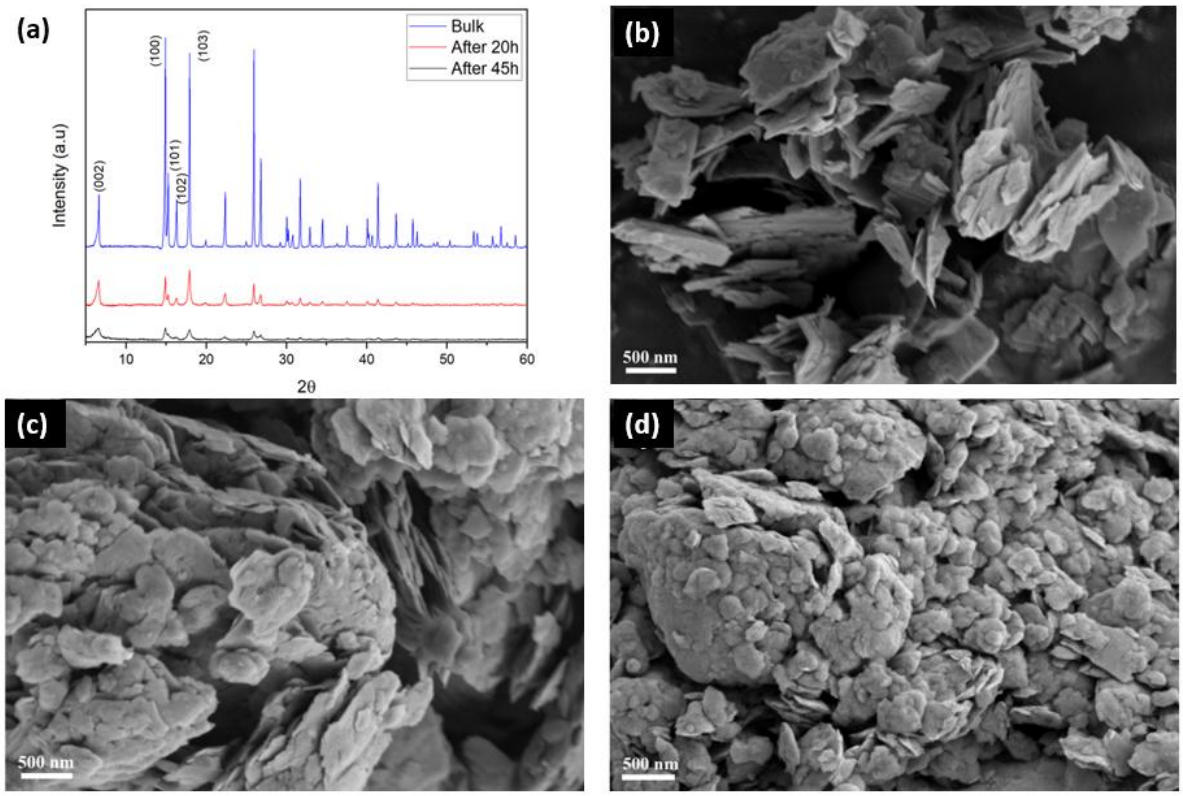


Figure 5.17 (a) XRD reflections for bulk $MoS_2$, and ball milled $MoS_2$ for 20 and 45 hours, (b-d) SEM images of $MoS_2$ with different ball milling time, (b) Bulk $MoS_2$, (c) $MoS_2$ after 20h ball milling (d) $MoS_2$ after 45h ball milling.

Furthermore, the crystalline structure of bulk $MoS_2$ exhibits also two pronounced reflections originating from (100) and (101) planes due to the preferential growth of the particles. As it was mentioned before, with the ball milling procedure, the intensity of all the reflections decreases, but especially the ones associated to the (100) and (101) planes.

The morphology of bulk $MoS_2$ and $MoS_2$ nanosheet was observed by SEM images. As shown in Figure 5.17, Figure 5.17b is the sheet-like bulk $MoS_2$, Figure 5.17c and 5.19d show the bulk $MoS_2$ after 20h and 45h ball milling. Following ball milling, bulk $MoS_2$ is transformed

into reduced-size nanosheets, facilitating homogeneous dispersion in the slurry and the formation of a functional interfacial layer on glass fiber D.

Figure 5.18 shows the surface of the GFD separator and functional separator. Figure 5.18a shows that the GFD separator has a network structure, which is expected to block polysulfides to inhibit the shuttle effect. Figures 5.18b and 5.18c show the surface of the $MoS_2$ functional separator. It can be seen that after functionalization, the original network structure of the GFD separator is covered by the $MoS_2$ functional layer, and flake $MoS_2$ materials of different sizes are evenly distributed on the surface of the separator.

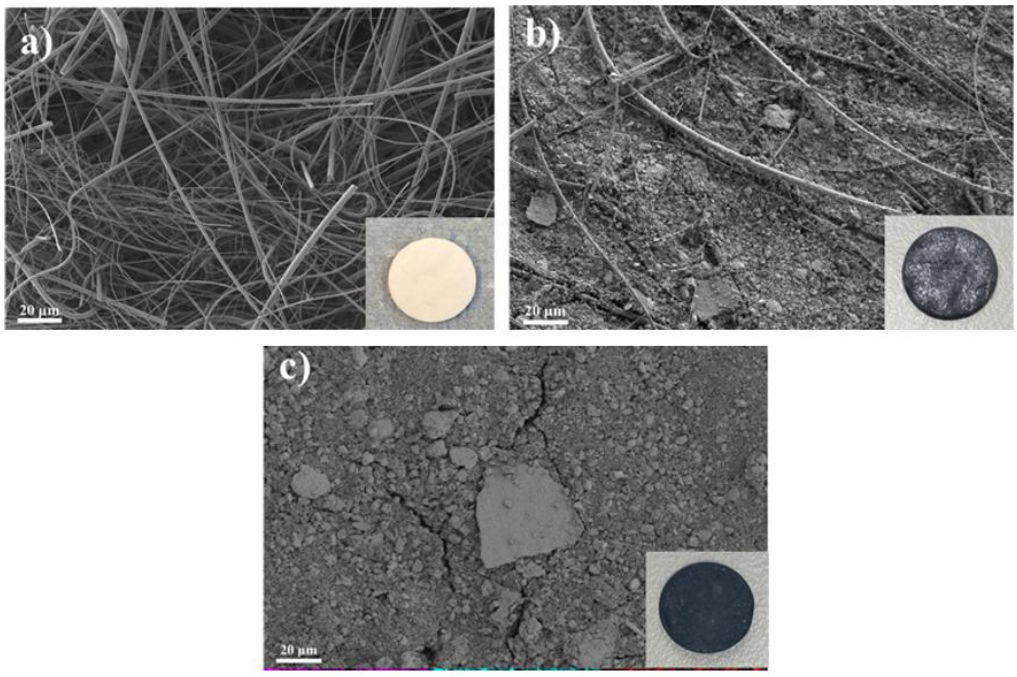


Figure 5.18 (a) GFD separator, (b) 20h $MoS_2$ functional separator, (c) 45h $MoS_2$ functional separator.

Furthermore, the visual adsorption experiment was used to test the effective anchoring of different kinds of $MoS_2$ on polysulfides. $MoS_2$ powders with different structures were placed in a polysulfide solution with TEGDME as the solvent to simulate the electrolyte environment of sulfur polymer-sodium batteries during charge-discharge. The anchoring ability of $MoS_2$ with different structures on polysulfides can be confirmed by observing the color of the polysulfide solution after $MoS_2$ is stored for a period of time. The clearer the

solution color, the more polysulfides in the liquid phase are adsorbed on the $MoS_2$ surface, which indicates that $MoS_2$ with this structure has a stronger ability to inhibit the shuttle effect. Figure 5.19 shows the results for different kinds of $MoS_2$ stored in polysulfide solutions for 2h and 72h. The solution with the 45h ball milling $MoS_2$ is lightest, which means that $MoS_2$ after 45h balling milling can efficiently anchor polysulfides. Therfore, the functional separator with 45h balling milling $MoS_2$ was used in the **P1**-sodium cells during the following tests.

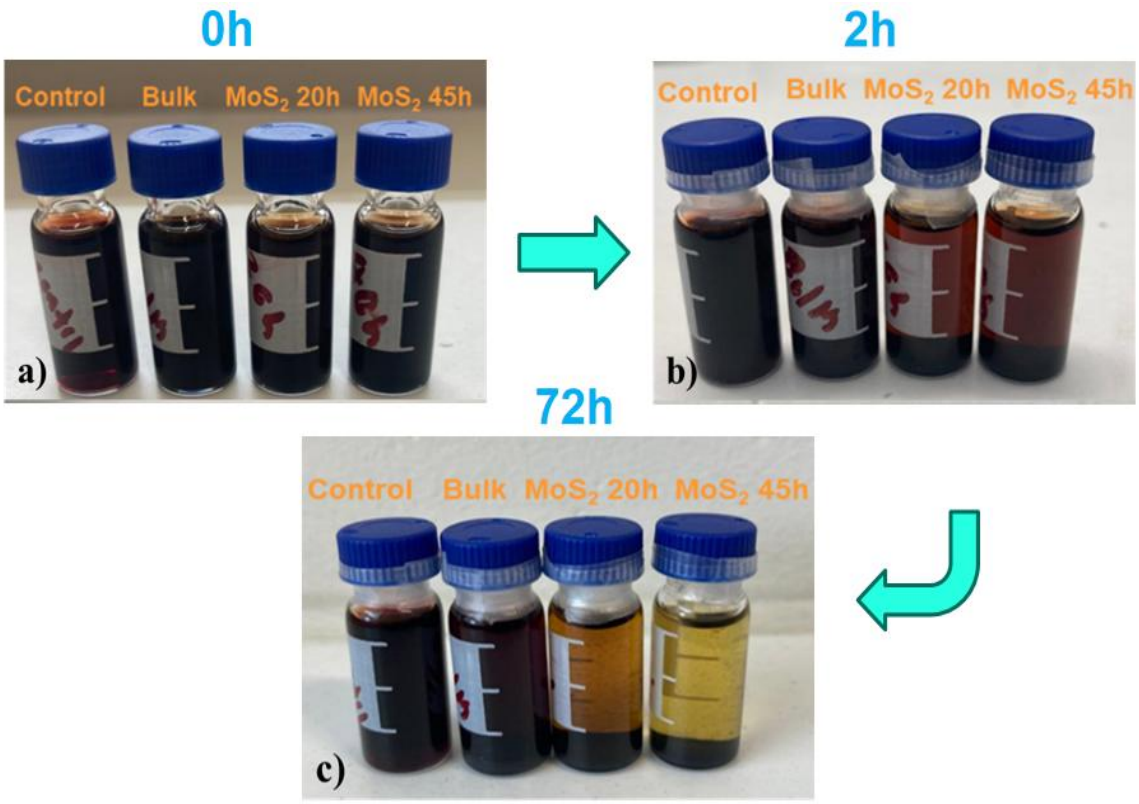


Figure 5.19 Bulk $MoS_2$, $MoS_2$ after 20h ball milling, and $MoS_2$ after 45h balling milling in polysulfide solution (a) 0h, (b) 2h, (c) 72h.

To further check the interaction of $MoS_2$ materials towards a sodium polysulfide solution (NaPS), X-ray photoelectron spectroscopy (XPS) studies were performed on the surface of all the $MoS_2$ samples (The XPS measurements were conduct by Isaac Paniagua). In all the spectra of Figure 5.20, the peak at 162.5 eV is the most intense and it is also linked to Mo3d5/2 (binding energy of 229.7 eV) and reliably attributed to S from $MoS_2$[132].

The $MoS_2$ samples also present signals at 161.6 and 163.5 eV; in this case, they are assigned to the terminal ($S_T^{-1}$) and bridging sulfur ($S_B^0$) atoms, respectively; which are in accordance to the molecular structure of polysulfides where the sulfur atoms at both ends have an oxidation state of -1, while the sulfur atoms in the middle of the chain have formal charge of zero [133]. Furthermore, an increase in the intensity of the signal at 168.8 eV is observed after the adsorption test, which is more pronounced for the ball-milled $MoS_2$ samples. This signal is attributed to the surface oxidation of $MoS_2$. However, the enhanced intensity can be described to the formation of thiosulfate complexes generated from oxidized sulfide species. This complexes likely originate from the interaction of $Na_2S_8$ with the solvent and atmospheric oxygen on the surface of the ball-milled $MoS_2$ sheets[130]. Therefore, the rise in this signal after the adsorption test suggests that the ball-milled $MoS_2$ samples have a stronger adsorption toward sodium polysulfides [134].

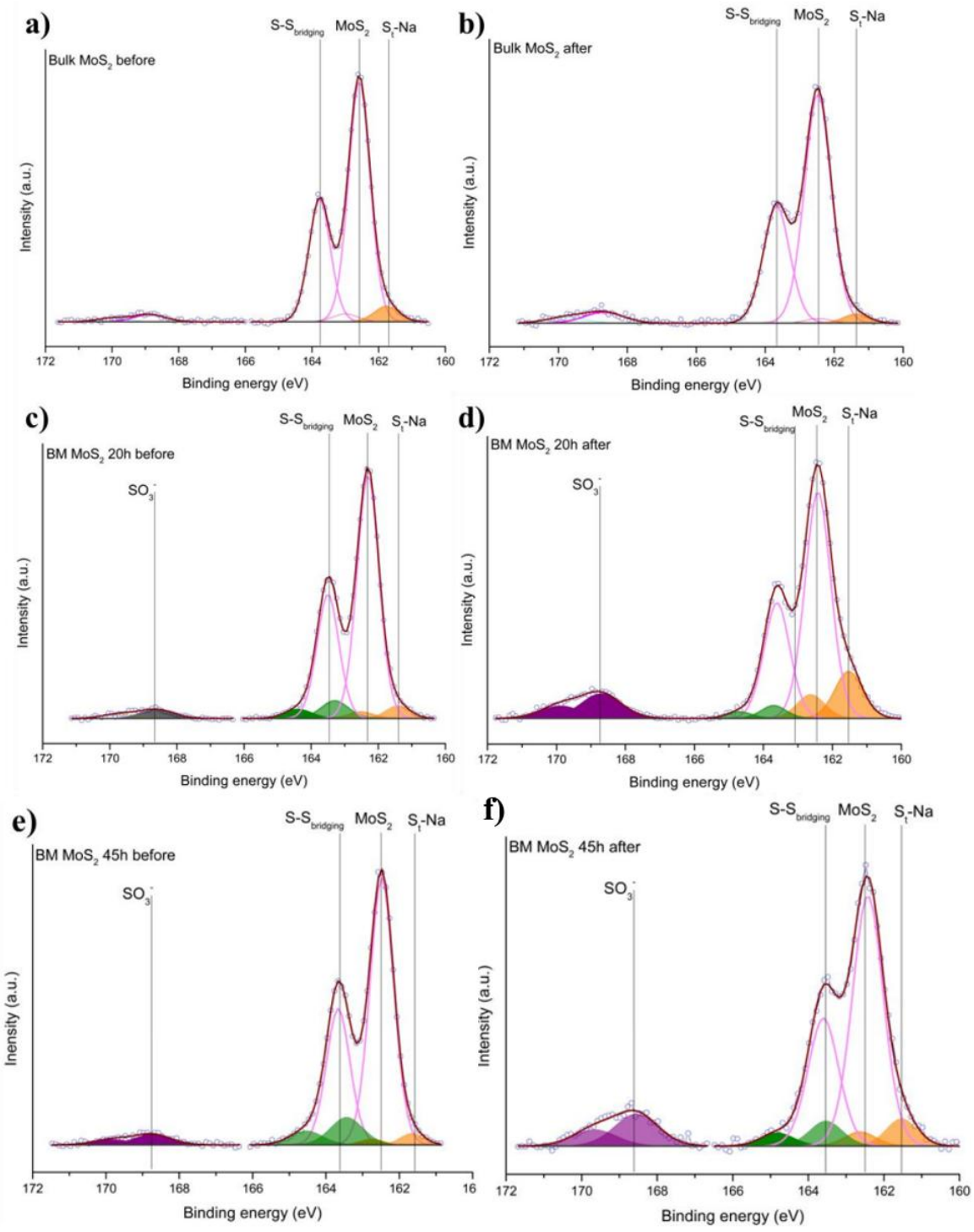


Figure 5.20 XPS S 2p spectra before and after the adsorption test of (a-b) bulk $MoS_2$ (c-d) ball milled $MoS_2$ for 20h, (e-f) ball milled $MoS_2$ for 45h.

**Galvanostatic Tests of P1 in Combination with$MoS_2$ Separator**

$MoS_2$ functional separator is introduced into the **P1**//Na cell to understand if the shuttle effect and the kinetics can be effectively improved. Figure 5.21 shows a comparison in terms of long cycling between a **P1**//Na cell with $MoS_2$ functional separator and one with GFD separator.

It can be observed that the cell with $MoS_2$ separator shows higher capacity during the first 50 cycles but it starts to decay from the 60th cycle. Figure 5.21b shows the coulombic efficiency (CE) of cells with different separator: **P1** cell with $MoS_2$ separator shows significantly higher CE than **P1** cell with GFD. This result proves the significant help of $MoS_2$ separator in inhibit shuttling effect. The higher CE indicates that the $MoS_2$ enhances sulfur utilization efficiency by anchoring polysulfides [135]. At first cycle, the **P1** cell with $MoS_2$ separator shows CE of 75%, which gradually increases to 90% at the $50^{th}$ cycle. After this, the CE slightly increases until reaching 95% at the end of $200^{th}$ cycles. Moreover, the CE of $MoS_2$ separator cell exhibits less fluctuation compared to GFD separator cell. However, the CE of less than 100% proves that although the functional separator is helpful in inhibiting shuttling effects, the ability to solve irreversible reactions of **P1** during charge and discharge is limited. There is a significant capacity decrease in the $MoS_2$ separator cell after 100 cycles of long cycle testing. Functional groups containing highly reactive nitrogen sites should be avoided in the design of polymer, as these active sites tend to undergo irreversible reactions with polysulfide species.

Figure 5.22 shows the charge and discharge curves of cell with **P1** cathode and $MoS_2$ separator/GFD separator at 500mA $g^{-1}$. As shown in Figure 5.22, the cell with **P1** cathode and GFD separator delivers only 90mAh $g^{-1}$ in capacity. In contrast, a higher capacity is obtained in the cell with $MoS_2$ separator. This is because the molybdenum metal sites contained in $MoS_2$ can promote the kinetics of the sulfur conversion reaction [136]. During the discharge process, the cell with $MoS_2$ separator exhibit a longer plateau between 2.2V and 2.4V,

attributed to the reaction of the conversion of long-chain sulfur to long-chain polysulfides. This demonstrates that the metal sites present in $MoS_2$ separators can effectively promote the solid-liquid reaction of sulfur chain conversion to polysulfides[137]. The same catalytic conversion effect is observed between 1.2V and 1.6V in cell with $MoS_2$ separator exhibit slower and longer diagonal lines, which indicates a more complete conversion of polysulfides to sodium sulfide than cells without functional separators[138].

The rate performance is tested between 500mA $g^{-1}$ to 2000mA $g^{-1}$. Figure 5.25 shows the significantly improved rate performance of cell with $MoS_2$ separator. At 500mA $g^{-1}$, 1000mA $g^{-1}$, 2000mA $g^{-1}$, cell with $MoS_2$ separator exhibit specific capacities of 162.0, 37.2, and 25.6 mAh $g^{-1}$. At the same time, it also shows 35.4 mAh $g^{-1}$ when back to 500 mA $g^{-1}$, which reflects the help of $MoS_2$ separator in capacity. The result indicate that $MoS_2$ separator can improve capacity under different current density of cell with **P1** polymer cathode by helping with charge transfer and electrochemical kinetics from metal site of $MoS_2$.

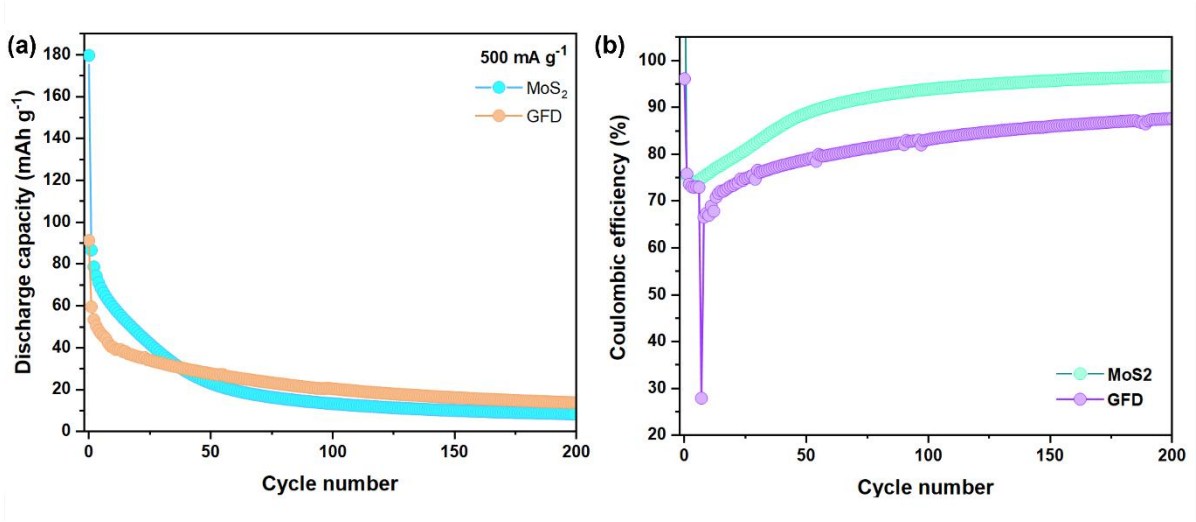


Figure 5.21 (a) Long cycle performance of **P1** cell with different separator at 500 mAh $g^{-1}$. (b) Coulombic efficiency of **P1** cells with different separator. (Electrolyte: 1M $NaCF_3SO_3$ in TEGDME, capacity is calculated by sulfur content of positive electrode, sulfur loading=0.8 mg $cm^{-2}$)

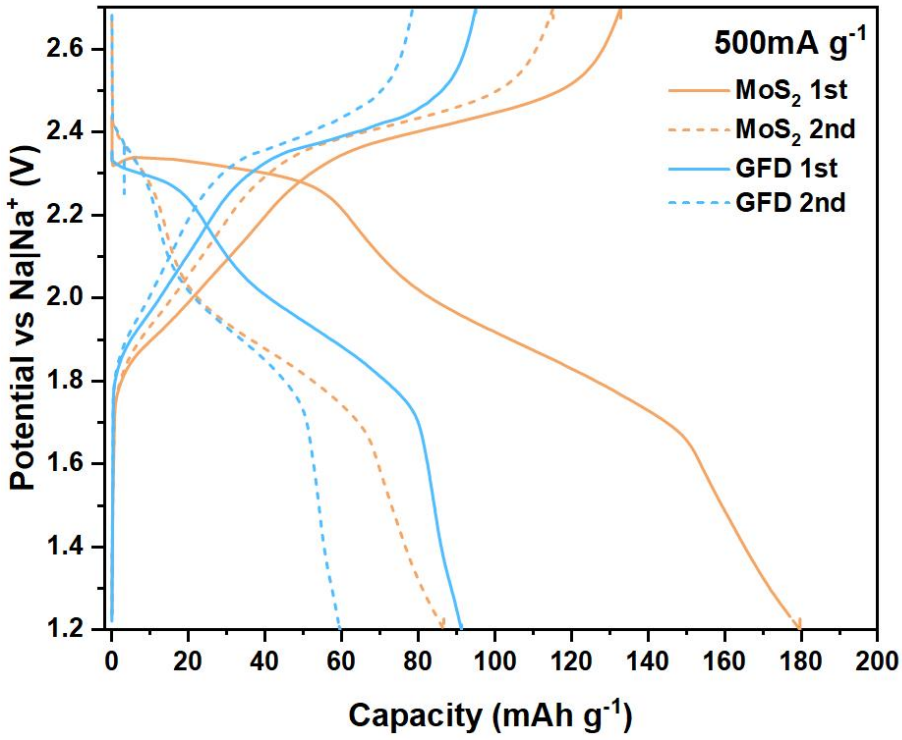


Figure 5.22 Charge-discharge curve of **P1** cells with different separator. (Electrolyte: 1M $NaCF_3SO_3$ in TEGDME, capacity is calculated by sulfur content of positive electrode, sulfur loading=0.8 mg $cm^{-2}$)

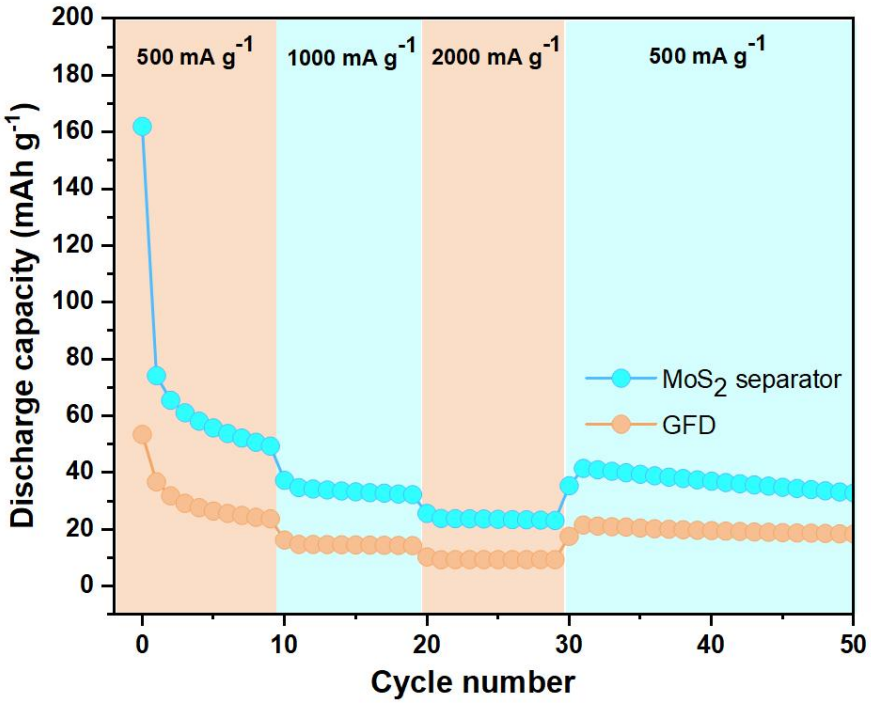


Figure 5.23 Rate performance of **P1** cell with different separator. (Electrolyte: 1M $NaCF_3SO_3$ in TEGDME, capacity is calculated by sulfur content of positive electrode, sulfur loading=0.8 mg $cm^{-2}$)

The impedance of cells with different separators was tested by electrochemical impedance spectroscopy (EIS). The corresponding Nyquist plots are shown in Figure 5.24a. Both impedance spectra display two distinct semicircles in the high-frequency ($10^5$-$10^3$ Hz) and medium-frequency regions ($10^3$-1 Hz), followed by a slight tail at low frequency (1-$10^{-2}$ Hz). This characteristic shape indicates that the overall electrochemical process involves two independent charge-transfer steps coupled with a limited ion diffusion process. The high-frequency semicircle corresponds to the resistance of the surface film or interfacial layer formed between the separator functional layer and the electrolyte, which can be represented as the film resistance ($R_x$) and constant phase element ($CPE_x$) in the equivalent circuit. For the cell with $MoS_2$ separator, this component is more pronounced, suggesting the presence of an additional interfacial layer caused by the $MoS_2$ functional layer or its interaction with sodium polysulfides[139]. The medium-frequency semicircle is attributed to the intrinsic charge-transfer resistance ($R_{ct}$) and double-layer capacitance at the cathode/electrolyte

interface ($CPE_{dl}$), representing the redox reaction of sulfur species. In low-frequency region, both cells exhibit a diffusion-related Warburg region, which corresponds to the sodium-ion diffusion within the electrode material (W in equivalent circuit). However, the cell with $MoS_2$ separator shows a smaller slope compared with the cell with GFD separator, indicating slower ion diffusion and higher diffusional impedance. To further evaluate the ion-diffusion behavior, the Warburg coefficient (σ) was derived from the linear fitting of Z' and $\omega^{-1/2}$ in the low-frequency region. According to the equation: $Z'=R_s \quad +\sigma\omega^{-1/2}$, a smaller σ value corresponds to faster ion diffusion. As shown in Figure 5.24b, the cell with $MoS_2$ separator exhibits a significantly larger σ compared with the cell with GFD separator. This suggests that although the $MoS_2$ functional layer provides chemical anchoring sites to anchor polysulfides and suppress the shuttle effect, it increases the interfacial and charge-transfer resistance due to its relatively low electronic conductivity and the possible formation of an insulating layer[140].

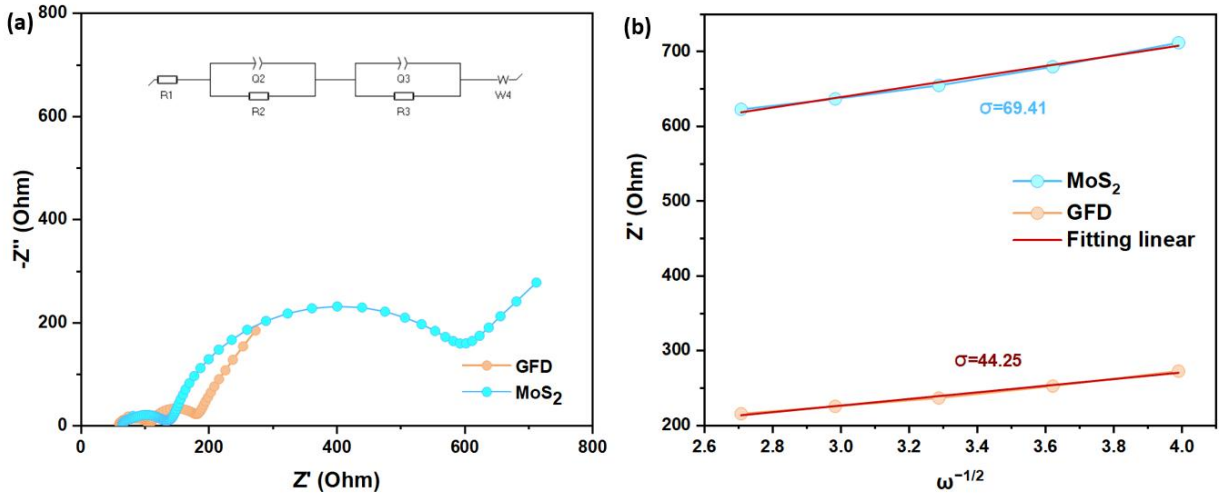


Figure 5.24 (a) EIS of **P1** cells with different separator. (b) Warburg fitting (Electrolyte: 1M $NaCF_3SO_3$ in TEGDME, sulfur loading=0.8 mg $cm^{-2}$)

**Post-mortem Study and Failure Mechanism Analysis**

To investigate evolution of chemical environment during cycling, X-ray photoelectron spectroscopy (XPS) was performed on **P1** electrodes before cycling and after the one cycle

(charged to 2.7V). As shown in Figure5.25, the S 2p spectrum of pristine **P1** (before cycling) is dominated by contributions at 163.52 eV [141] and 164.02 eV, attributed to C-S bonds and S-S bonds respectively, associated with the polymer skeleton and sulfur chains. After one cycle (terminated in charge), **P1** a new peak at 168.17 eV appears, which can be attributed to the S-O bond [142], indicating the formation of oxidized sulfur species. This may be closely related to the generation and further oxidation of polysulfides ($Na_2S_x$, x>2). In addition, the intensity of the S-S peak at 164.50 eV decreases markedly after cycling, suggesting significant modification of the sulfur bonding environment at the electrode surface. While a weak S-S signal remains detectable, the overall spectral changes indicate substantial structural rearrangement rather than complete preservation of the initial sulfur framework. The result of C 1s spectrum can further confirm this conclusion. As shown in Figure 5.25c, the C1s spectrum of **P1** exhibits a C-S bond signal at 285.83 eV [143], which is attributed to the binding of sulfur chains to the carbon skeleton in **P1**. After one cycle, the C-S signal in the C 1s spectrum of **P1** is strongly attenuated. This attenuation suggests disruption or transformation of sulfur-carbon linkages during electrochemical cycling. Together, these observations indicate that the original sulfur bondings are not fully restored upon charging.

In addition, N 1s spectra show two components at 399.76 and 401.19 eV for the pristine electrode, attributed to neutral N-C=O and a positively polarized/oxidized N species ($N^+$), respectively (Figure 5.25e). After 4 cycles, the higher binding energy component is no longer clearly resolved and the remaining dominant peak shifts to 399.26 eV. This shift to lower binding energy suggests a change in the electronic environment of nitrogen, possibly associated with deprotonation, reduction or altered bonding configurations during cycling[144]. Such changes are consistent with modifications of nitrogen-containing functionalities within the polymer matrix. Complementary changes are observed in the C1s spectrum. After one cycle, the C-N component (at 286.23eV) is strongly attenuated,

accompanied by the emergence of Sp2-like C. These spectral variations suggest a restructuring of the carbon-nitrogen bonding environment during electrochemical cycling, potentially associated with sulfur-related bond rearrangements (Figure 5.25c and 5.25d).

Furthermore, the XPS analysis of the **P1** positive electrode after four cycles (500mA $g^{-1}$, charged to 2.7V) was performed to further investigate the structural evolution of **P1** during cycling. As shown in Figure 5.26, the C-S signal in the in S2p spectrum becomes more prominent and slightly shifts toward higher binding energy after four cycles. This behavior suggests progressive modification of the sulfur bonding environment and possible enrichment of covalent C-S bonds at the electrode surface. In the N1s spectrum, the peak position shifts toward lower binding energy, suggesting a change in the electronic environment of nitrogen. Such changes are consistent with the formation of thioamide-like linkages [145]. This is in agreement with the strengthened C-S signal in S 2p (Figure 5.26a and 5.26b).

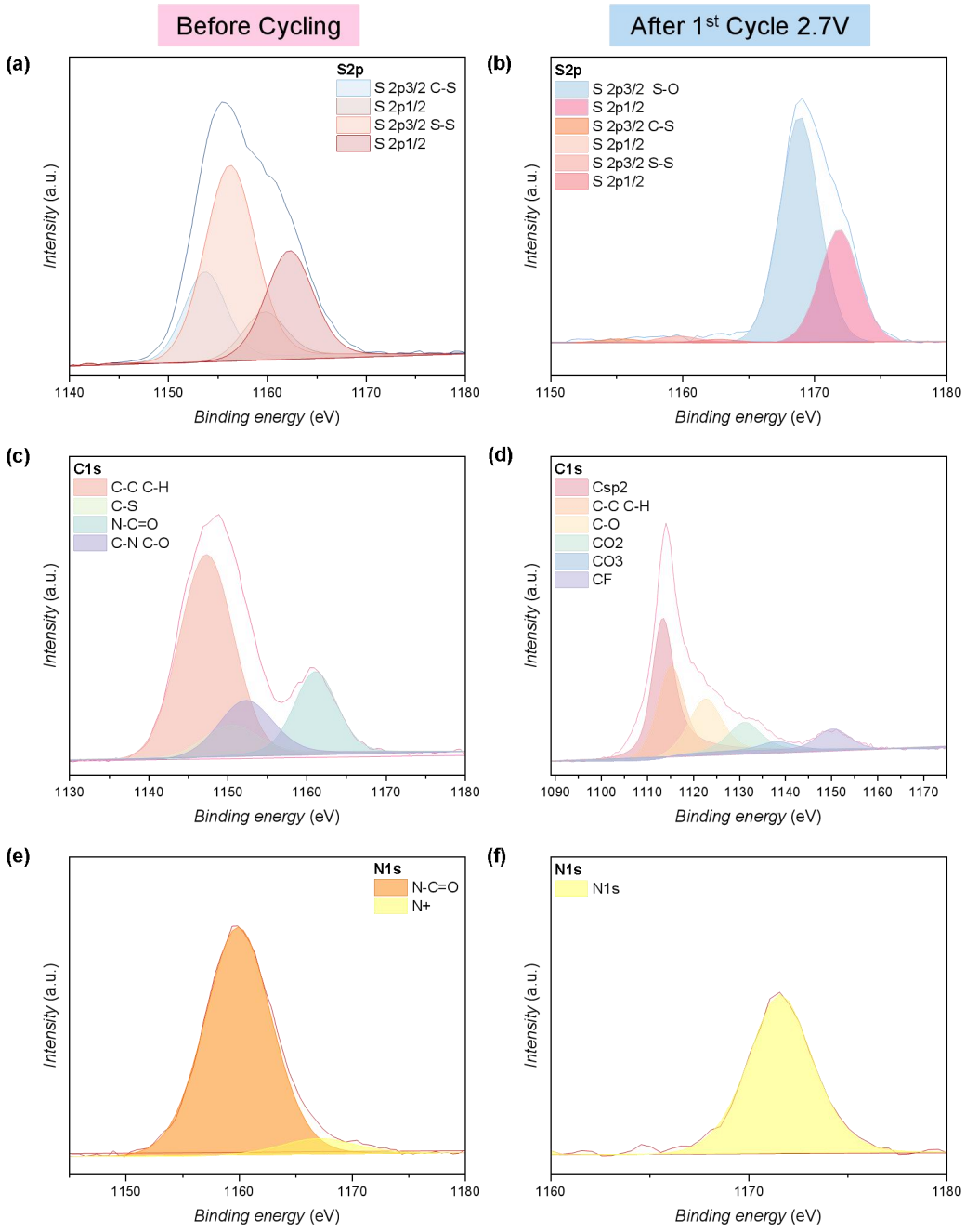


Figure 5.25 XPS spectrum of **P1** (a) S 2p before cycling, (b) S 2p after cycling, (c) C 1s before cycling, (d) C 1s after cycling, (e) N1s before cycling, (f) N 1s after cycling. (For cycled cell: 500mA $g^{-1}$, cycled for 1 cycle, end at charge stage at 2.7V)

Furthermore, the XPS results of the **P1** positive electrode after four cycles (500mA $g^{-1}$, cycled for 4 cycles, end at charge stage at 2.7V) were further provided to investigate the structural changes of **P1** during the cycling. As shown in Figure 5.26, the C-S signal becomes

more prominent and slightly shifts to higher binding energy in S2p spectrum after 4 cycles, indicating progressive formation of covalent C-S linkages and irreversible fixation of sulfur species. For N1s spectrum, peak position shifts towards lower binding energy, this shift suggests increase electron density at nitrogen, indicates that as respective cycles the formation of thioamide-like linkages become increase[145]. This is in concert with the strengthened C-S signal in S 2p (Figure 5.26a and 5.26b).

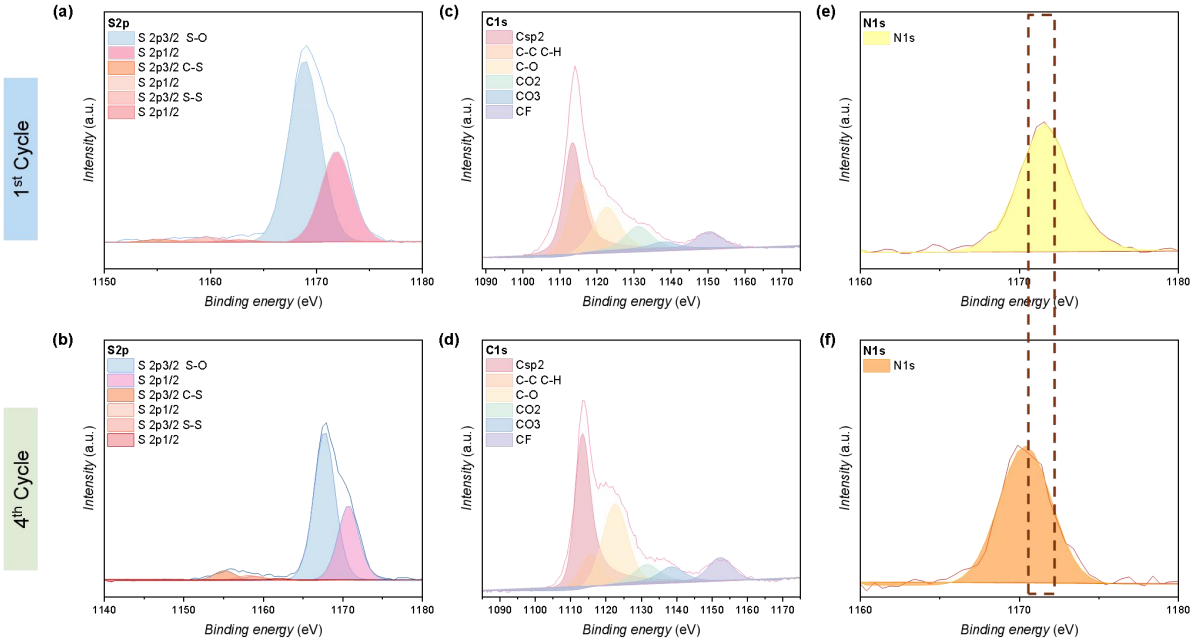


Figure 5.26 XPS spectrum of **P1** (a) S 2p after 1cycle, (b) S 2p after 4 cycles, (c) C 1s after 1 cycle, (d) C 1s after 4 cycles, (e) N1s after 1 cycle, (f) N 1s after 4 cycles. (For all cycled cell: 500mA $g^{-1}$, end at charge stage at 2.7V)

Based on the combined electrochemical and XPS results, the failure mechanism scenario of **P1** can be proposed as follows:

**Stage I**: **Initial sodiation and sulfur bond modification.** During the first discharge (initial sodiation) sulfur species within the polymer matrix are reduced, likely forming soluble $Na_2S_x$ intermediates (x=2-6). These species may partially shuttle to sodium anode side, and, due to the nucleophilic nature of $S_x^{2-}$ they may attack polar functionalities (C=O/-NH-) in the polymer backbone, potentially initiating bond rearrangements.

**Stage II**: **Progressive chemical immobilization of sulfur.** Continued exposure to reactive nucleophilic $S_x^-$ ions may lead to modification of amide groups with formation of C-S, S-N and thioamide-like C(=S)-N linkages, as suggested by XPS analysis. Such structural rearrangements could chemically anchor sulfur species, reducing their electrochemically accessibility and hindering reformation of the original sulfur bonding motif during oxidation.

**Stage III**: **Gradual consumption of electrochemically active sulfur.** Sulfur species not incorporated into the rearranged polymer network may exists as $Na_2S_2$/$Na_2S$ and undergo partial re-oxidation. However, repeated interaction with reactive polysulfide intermediates can further modify the polymer matrix, progressively consuming active sulfur and contributing to sustained coulombic inefficiency during cycling.

The results suggest that polymers containing highly reactive nitrogen centers (such as amide groups) may undergo chemical interactions with polysulfide species during cycling. The nitrogen sites can facilitate bond rearrangements involving C-N and sulfur species, leading to the formation of C-S/N-S bonds or thioamide-type linkages, as indicated by XPS analysis. Such structural modifications may chemically immobilize sulfur and reduce the electrochemical accessibility. Consequently, the reversible conversion reaction between sulfur species (S-S bond) and sodium ion becomes progressively suppressed, resulting in capacity decay and low coulombic efficiency. Therefore, although nitrogen-doped polymers can provide polar sites for polysulfide anchoring, excess reactivity of nitrogen functionalities may compromise structural reversibility and limit their effectiveness in Na-S batteries.

### 5.2.3 Conclusion

The main conclusions and innovations of this research are as follows:

(1) A novel sulfur-rich polyamide (**P1**) was applied as the positive electrode of sodium metal batteries to explore the effect of such functionalities on cycling stability. In this work, a sulfur-rich polyamide (**P1**) was investigated as a positive electrode material for RT Na-S

batteries to evaluate the stability of amide-containing sulfurized polymer networks. The electrochemical results reveal limited reversibility, accompanied by rapid capacity decay. Post-mortem XPS analysis indicates substantial modification of sulfur and nitrogen bonding environment after cycling, suggesting that the original sulfur chains are not fully restored during oxidation. The data support a degradation scenario in which reactive polysulfide species interact with amide functionalities, leading to structural rearrangements within the polymer matrix and progressive loss of electrochemically accessible sulfur. As a result, **P1** shows low initial capacity (90 mAh $g^{-1}$ at 500mA $g^{-1}$) low coulombic efficiency (<85% at 500mA $g^{-1}$ for 200 cycles) and poor long-term stability. These findings demonstrates that while nitrogen-containing polymers can provide polar sites for polysulfide interaction, excessive chemical reactivity of nitrogen functionalities may compromise structural reversibility of the cathode. Careful molecular design and control of heteroatom reactivity are therefore essential for the development of stable sulfurized polymer cathodes for RT Na-S batteries.

(2) Regulating sulfur conversion reaction by functional separator: $MoS_2$ can anchor polysulfides to increase the capacity (at 500 mA $g^{-1}$, capacity increases from 60mAh $g^{-1}$ to 162mAh $g^{-1}$). At the same time, the $MoS_2$ can effectively anchor polysulfides to inhibit shuttle effects and improve stability (at 500 mA $g^{-1}$, CE increase from 85% to 95%). But the $MoS_2$ separator exhibits a slightly higher charge-transfer resistance that needs to be optimized.

**Authorship Contributions**

The conceptualization and design of the experiments were primarily developed by Liwen Yang under supervision of Prof. Dr. Sonia Dsoke and Prof. Dr. Hatice Mutlu. The **P1** materials were provided by Prof. Dr. Hatice Mutlu. The cell assembly, and electrochemical testing were performed by Liwen Yang in IAM-ESS of Karlsruhe Institute of Technology.

Structural characterizations were conducted and analyzed by Prof. Dr. Hatice Mutlu and Dr. Bercis Pektas with technical support from Mulhouse University. *Ex-situ* XPS test was provided by Prof. Dr. Hatice Mutlu and Dr. Bercis Pektas and Dr. Samar Hajjar-Garreau with technical support from Mulhouse University. XRD, SEM and XPS for $MoS_2$ separator were conducted by Isaac Paniagua with technical support from IAM-ESS. Liwen Yang prepared the manuscript draft, and it was revised under the supervision of Prof. Dr. Sonia Dsoke and Prof. Dr. Hatice Mutlu.

## 5.3 Solvent-mediated Synthesis of Sulfur-carbon Composites with Uniform Sulfur Dispersion and Performance Optimized by Functional Separator

### 5.3.1 Introduction

In Sections 5.1 and 5.2, the electrochemical behavior and reaction mechanisms of sulfur-containing polymer cathodes for RT Na-S batteries were investigated. The result revealed the reasonable charging and discharging range of SPAN positive electrode and the side reactions that occur under deep discharge, and explored the failure mechanism of polymers containing active nitrogen sites in RT Na-S batteries

Moreover, the intrinsic electronic conductivity and active sulfur content of polymer-based cathodes remain limited, leading to sluggish reaction kinetics and relatively low energy density. These issues become more pronounced under high-loading and long-term cycling conditions, where capacity degradation is observed. Despite all these challenges, the uniform molecular-level distribution of sulfur in sulfur-containing polymers can still be an important advantage and it could play a crucial role in enhancing electrochemical activity and cycling stability. Driven by this hypothesis in chapter 3, this chapter aims to extend the design principle of molecularly uniform sulfur distribution to the development of sulfur-carbon composite.

In previous studies, sulfur-carbon composite is widely used to solve challenges of RT Na-S batteries due to the following reasons: (1) High conductivity that can provide electronic transmission paths[82], (2) Porous structure that can provide space for volume changes happening during the conversion of sulfur to sulfide[83], (3) Functional group with physical/chemical adsorption sites that can anchor polysulfide[84], (4) High specific surface area that can help to disperse sulfur uniformly at the nanoscale and shortening the electron and ion transport pathways. At the same time, the carbon with high specific surface area can accommodate a higher loading of sulfur without causing severe aggregation[146], [147].

Sulfur-carbon composite cathodes have been widely synthesized via the melt-diffusion method, in which elemental sulfur is physically infiltrated into the carbon matrix at elevated temperatures. Although this approach is simple and effective to achieve high sulfur loading, the distribution of sulfur within the host is often nonuniform, and sulfur tends to aggregate on the external surface or block the pores of the carbon framework. Such uneven sulfur dispersion results in limited interfacial contact between sulfur and the conductive carbon matrix, impeding electron/ion transport and leading to low utilization of active sulfur.

This chapter employed a solvent-based synthesis method from prior reports to construct the sulfur-carbon composite[148]. This method allows sulfur species to be introduced and anchored within the carbon framework through solution-phase diffusion and subsequent chemical interactions, leading to a more homogeneous dispersion of sulfur at the nanoscale. The improved sulfur-carbon interfacial contact can facilitate charge transfer and ion diffusion during electrochemical reactions, thereby enhancing the reaction kinetics and cycling stability. Consequently, the solvent method provides a more controllable and efficient pathway for designing high-performance sulfur-carbon cathode. At the same time, the reaction mechanism of this composite was investigated and $MoS_2$ functional separator in chapter 5.2 was used to improve the capacity and electrochemical kinetics.

### 5.3.2 Result and Discussion

**Characterization of Materials**

At first, elemental analysis was used to obtain sulfur content of CS. As shown in Table 5.2, CS has 56.1% sulfur content (take the average of three-time tests).

Table 5.2 Elemental analysis of CS material (Parallel measurement three times)

| Sample | N% | C% | H% | S% |
|---|---|---|---|---|
| CS-1 | 2.84 | 33.04 | 2.58 | 55.32 |
| CS-2 | 2.75 | 32.93 | 2.56 | 57.44 |
| CS-3 | 3.12 | 34.11 | 2.85 | 55.38 |

**Electrochemical Behavior**

Cyclic voltammetry (CV) is used to study the electrochemical reactions between CS and sodium in the cell.

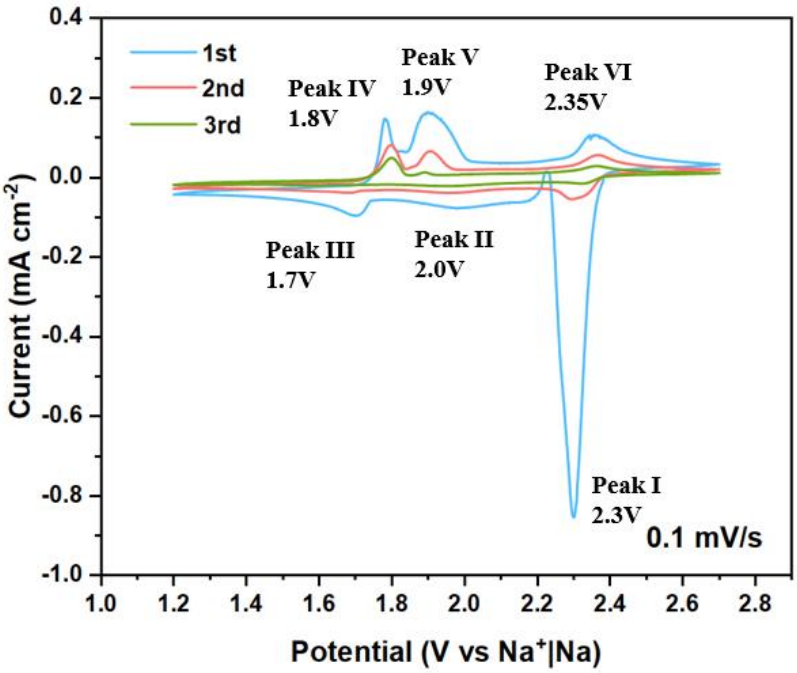


Figure 5.27 CV curve of CS positive electrode at 0.1mV/s. (Electrolyte: 1M $NaCF_3SO_3$ in TEGDME, sulfur loading=0.8-1 mg $cm^{-2}$)

As shown in Figure 5.27, at the first cycle, the curve shows three oxidation peaks and three reduction peaks. Among them, peak I at 2.3V and peak II at 2.0V can be regarded as the sulfur converted into long-chain sodium polysulfide ($Na_2S_6$ and $Na_2S_4$)[149]. Peak III at 1.7V

can be regarded as liquid-solid conversion reaction of $Na_2S_6$ and $Na_2S_4$ to $Na_2S_2$ and $Na_2S$[150]. Peak IV and peak V can be described as the reaction of solid phase polysulfide ($Na_2S_2$ and $Na_2S$) be oxidized to long-chain polysulfide ($Na_2S_6$ and $Na_2S_4$)[151]. The splitting of the peak due to the disproportionation reaction of $Na_2S_6$ an $Na_2S_2$/$Na_2S$ to $S_4^{2-}$ and dissociation of $S_6^{2-}$ to $S_3$•– radical[152].

In Figure 5.27a, a much stronger current is observed at the process peak associated with the conversion of sulfur to long-chain polysulfides, compared with other reaction peaks, indicating that this reaction proceeds relatively easily (peak I). In contrast, the subsequent liquid–solid conversion of polysulfides to sodium sulfide (step II) exhibits an almost indistinguishable reaction peak (peak III), suggesting sluggish kinetics [153]. Consequently, during the charge process, the oxidation peak intensity remains lower than that of peak I, reflecting the limited conversion of polysulfides to sodium sulfide[154]. As a result, only a part of sulfur transforms to sodium sulfide, while the majority persists in the electrolyte as polysulfides and then get lost through the shuttle effect. This conclusion was further confirmed by CV curve at second and third cycle. As shown in the Figure 5.27, in the second cycle, the peak current intensity of both reduction and oxidation peak decrease noticeably compared with the first one. Among all the redox peaks, the current intensity of peak I decreases most significantly, indicating substantial loss of active sulfur after the first oxidation process. This loss leads to a weakened reaction corresponding to the conversion of sulfur into long-chain polysulfides (corresponding to peak I). The decrease in peak current intensity is more pronounced in the third cycle, both the oxidation peak and the reduction peak were almost invisible. This indicates irreversible reaction in the first cycle, which reduced the observable reaction current intensity at second cycle and third cycle.

**Galvanostatic Tests of CS Positive Electrode and Performance Optimized by Different Functional Separator**

At first, the long cycle performance of CS cell with GFD separator was tested, and the test results are shown in Figure 5.28. At 500mA $g^{-1}$, the CS cell provided a capacity of 624 mAh $g^{-1}$ during the first discharge and then showed significant attenuation during the second cycle. This is consistent with the above CV test results and conclusions, the sluggish kinetic of the positive electrode in the first discharge reaction caused subsequent reactions to be hindered. As the cycle continued, after 100 cycles, the capacity decays to near 0 mAh $g^{-1}$. The coulomb efficiency (Figure 5.28b) is 110% in first cycle, and decrease to 80% in the second cycle, indicating that irreversible reactions occur during both the first and second cycle. In the following 50 cycles, the CE is lower than 95%, this indicates that there is a loss of active sulfur and a decrease in reversible capacity in each cycle, which is consistent with the capacity decay from the 2nd to the 50th cycle in the long cycle test (Figure 5.28a). During 100 cycles, the coulomb efficiency finally stabilized at about 95%, which corresponding to capacity decrease to almost 0 mAh $g^{-1}$. Moreover, Figure 5.28c shows the potential profile of CS cathode, in the first discharge process, two distinct voltage plateaus can be clearly observed at 2.3 V and 1.7 V. The higher-voltage plateau around 2.3 V corresponds to the reduction of elemental sulfur to form soluble long-chain sodium polysulfides ($Na_2S_x$, x=4-8, in CV curve is peak I). The subsequent lower-voltage plateau at around 1.7 V is attributed to the further reduction of these soluble polysulfides into short-chain species ($Na_2S_2$ and $Na_2S$, in CV curve is peak III). During the following charge process, broad oxidation plateaus reappear between 2.0 V and 2.4 V, corresponding to the reverse conversion of $Na_2S/Na_2S_2$ back into polysulfides and sulfur. The above charge-discharge profiles exhibit distinct voltage plateaus during the $1^{st}$ to $5^{th}$ cycles.

However, from the 10th cycle, the characteristic discharge plateaus at approximately 2.3 V gradually disappear and the voltage profiles evolve into sloping curves (Figure 5.28c). This transition coincides with the abrupt increase in coulombic efficiency (CE) observed at the same stage (Figure 5.28b and Figure 5.28d). The simultaneous disappearance of voltage plateaus and stabilization of CE suggests that the electrochemically active sulfur species are largely irreversibly depleted after the initial cycles. As the redox-active sulfur becomes exhausted, the Faradaic reactions associated with polysulfide conversion are progressively suppressed.

After $10^{th}$ cycle, the remaining capacity no longer exhibits clear signatures of sulfur redox behavior. Instead, the sloping voltage profiles and nearly constant CE are more characteristic of non-Faradaic charge storage mechanisms[128]. In this cell, the residual capacity is mainly attributed to the electric double-layer capacitance and limited pseudocapacitive contributions of the conductive carbon framework, rather than to reversible sulfur conversion reactions. This transition from sulfur-dominated Faradaic processes to carbon-dominated capacitive storage explains both the significantly reduced capacity and the stabilized coulombic efficiency observed during long-term cycling.

Furthermore, the continuous increase in CE during the early cycles indicates that a fraction of the active sulfur becomes electrochemically inactive after each cycle. This loss can be attributed to sluggish solid-liquid-solid conversion kinetics and the shuttle effect, which lead to irreversible sulfur loss, interfacial passivation, and the formation of electrochemically inert species. As a result, while the CE approaches 100% at later stages, it reflects the dominance of non-Faradaic processes rather than improved reversibility of sulfur redox reactions.

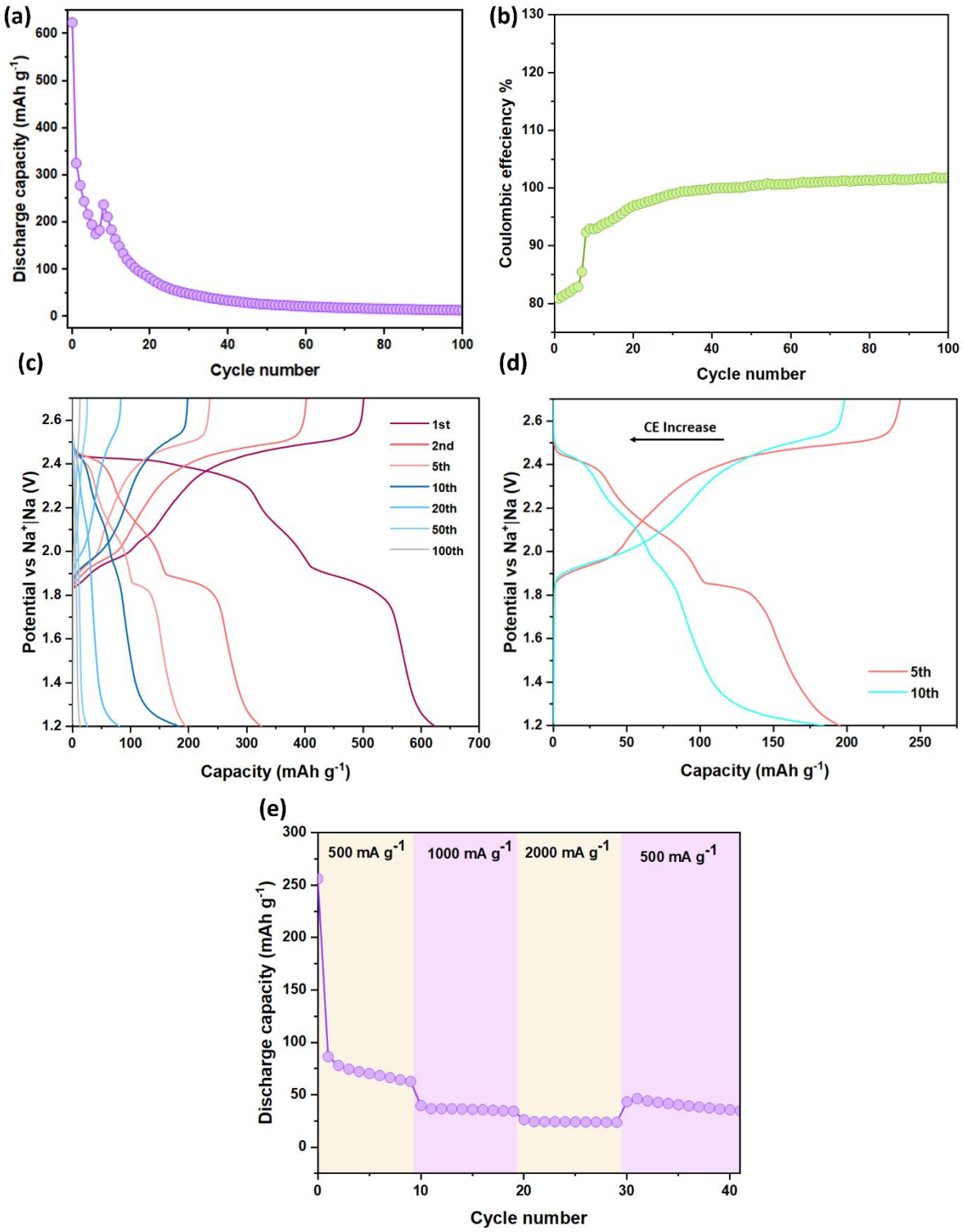


Figure 5.28 (a) Cycle performance of cell with CS positive electrode at 500 mA $g^{-1}$, (b) Coulombic efficiency of cell with CS positive electrode at 500 mA $g^{-1}$, (c) Charge-discharge curve of cell with CS positive electrode, (d) Charge-discharge curve of cell with CS positive electrode ($5^{th}$ and $10^{th}$ cycle) (e)

Rate performance of cell with CS positive electrode. (Electrolyte: 1M $NaCF_3SO_3$ in TEGDME, capacity calculated by mass of sulfur, sulfur loading=0.8-1 mg $cm^{-2}$).

Furthermore, the rate capability of the CS cell was evaluated under different current. As shown in Figure 5.28e, the CS cell initial discharge capacity of 250 mAh $g^{-1}$ at 500 mA $g^{-1}$, followed by a rapid decrease to around 100 mAh $g^{-1}$ in the subsequent cycle. This decline is consistent with the capacity fading observed during the first and second cycles in the long performance tests. Furthermore, as the current density further increases, the capacity of the CS cell exhibits no significant decay, indicating that the electrode maintains stable behavior under high-rate conditions. These results prove the potential of the CS material for high-rate Na-S batteries.

In order to solve the problems of sluggish kinetics and poor reversibility of CS materials, the $MoS_2$ functional separator (discussed already in chapter 5.2) were introduced into CS cell to understand their role on trapping polysulfide via catalytic effect of metal sites[155]. Two kinds of $MoS_2$ separator (different ball milling time leads to different structure of $MoS_2$) were tested to understand the role of the structure of $MoS_2$ on the performance. At first, the CV curve was tested to see how the separator works in cell. As shown in Figure 5.29a, the cell with $MoS_2$ separator shows higher peak current than cell with GFD separator, which indicates better electrochemical kinetic and electron transfer rate caused by $MoS_2$ functional layer.

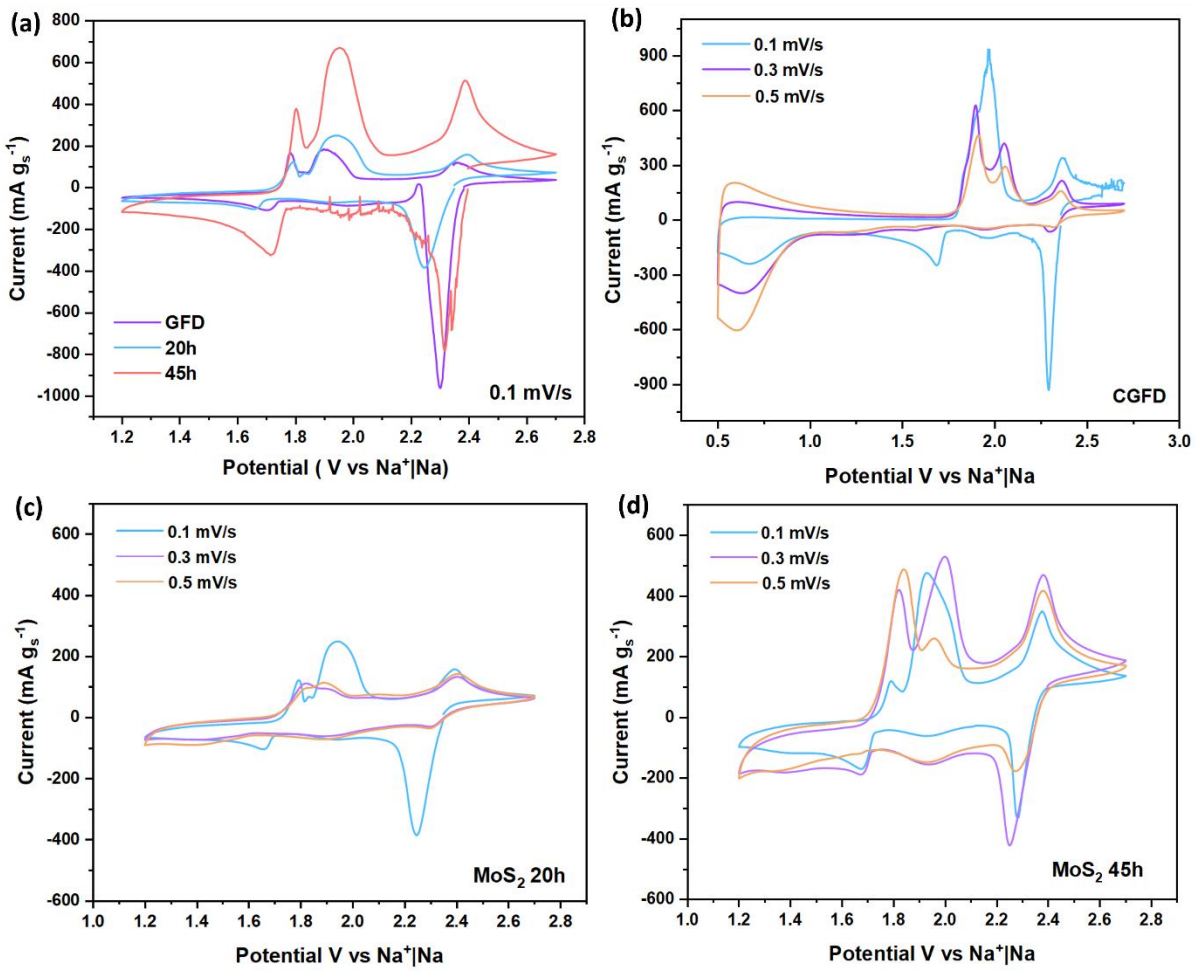


Figure 5.29 CV curve of cell of CS positive electrode with different kind of functional separator (a) GFD, $MoS_2$ 20h and $MoS_2$ 45h, (b) CGFD with different scan rate, (c) $MoS_2$ 20h with different scan rate, (d) $MoS_2$ 45h with different scan rate. (For each different scan rate: cycling for 3 cycles, and shows first cycle for each scan rate; Electrolyte: 1M $NaCF_3SO_3$ in TEGDME, capacity calculated by mass of sulfur, sulfur loading=0.8-1 mg cm$^{-2}$)

As shown in Figure 5.29, the CV curves of the cell with CGFD separator exhibit stronger peak currents and sharper redox features compared with cell with GFD separator, indicating enhanced redox activity and improved reaction kinetics. The more pronounced peaks suggest that the CGFD functional layer facilitates charge transfer and promotes faster electrochemical responses of sulfur species. However, at higher scan rates, several redox peaks gradually weaken or even disappear, suggesting that some electrochemical reactions are kinetically

hindered and cannot proceed completely. This phenomenon may also be associated with the shuttle effect that cause the sulfur loss. This result indicates that although the CGFD functional layer on the CGFD separator promotes redox kinetics by providing localized electron-transport pathways on the cathode side without compromising the intrinsic electrical insulation of the separator, its ability to suppress the shuttle effect remains limited, leading to the continuous loss of active sulfur species during cycling. The enhance of peak current and narrowed peak shape also shows in the CS cell with $MoS_2$ separator. This is due to the catalytic effect of the molybdenum metal site in $MoS_2$, which can reduce the reaction activation energy of polysulfides, making it easier to convert into short-chain polysulfides[156]. This is further demonstrated by the significant enhancement in peak current of the reduction peak II (the liquid-solid process of the polysulfide converted into short-chain polysulfides/sodium sulfide) and the oxidation peak I (solid-liquid conversion during the charge process).

On this basis, further observation of the high scan rate CV test shows that this kinetic effect is still significant at high scan rates. The cell with the $MoS_2$ separator has a visible reaction peak at high scan rates, instead of invisible peak shown by cell with GFD separator. More importantly, as shown in Figure 5.29d, the peak current intensity at high scan rates is consistent with higher than the peak current at low scan rates in cell with $MoS_2$ 45h separator. This phenomenon can be attributed to the increased exposure of metal active sites on the surface of the flake-like $MoS_2$ after 45h ball milling. Such structural and interfacial advantages facilitate faster charge-transfer kinetics and significantly promote the reaction of conversion of polysulfide to sulfur.

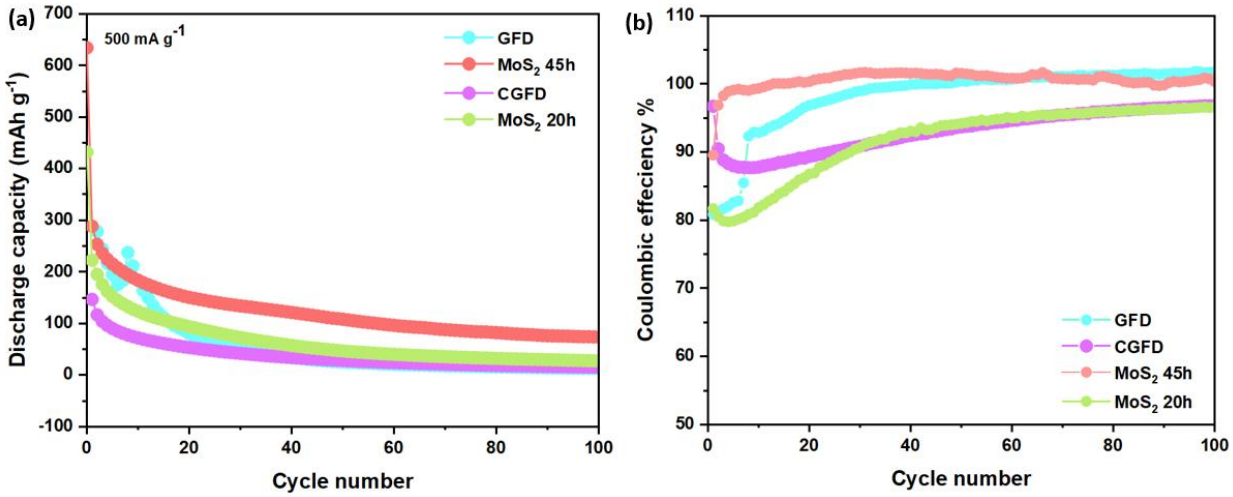


Figure 5.30 (a) Long cycle performance of CS positive electrode with different separator at 500 mA $g^{-1}$, (b) Coulombic efficiency of CS positive electrode with different separator at 500 mA $g^{-1}$(Electrolyte: 1M $NaCF_3SO_3$ in TEGDME, capacity calculated by mass of sulfur, sulfur loading=0.8-1 mg $cm^{-2}$)

Furthermore, Figure 5.30 shows the cycling performance of CS cells with different separators, the CS cells with $MoS_2$ separators and CGFD (same as chapter 5.1) separators deliver higher capacity,this improvement can be attributed to the enhanced reversibility of active sulfur species and the accelerated redox kinetics facilitated by the $MoS_2$ separators and CGFD separators. Among them, the cell with $MoS_2$ 45h functional separator shows the best performance in agreement with the CV. Moreover, Figure 5.30b shows the CE of CS cell with the $MoS_2$ 45h functional separator, which maintained of 100% in 100 cycles. In contrast, the cell with the GFD separator exhibited a coulombic efficiency of approximately 90% over 100 cycles. The cell with the CGFD separator provides an initial coulombic efficiency of about 96%, and decrease to 90% during the first five cycles, which gradually increased to around 92% in subsequent cycles and eventually reached 95% after 60 cycles. This indicates that during the 100 cycles, the CGFD cell suffers from continuous side reactions and the active sulfur is lost at each cycle, leading to severe capacity decay. The $MoS_2$ 20h separator cell displayed a similar trend to that of the CGFD cell, exhibiting coulombic efficiency of around 80% in the first five cycles and reaching a maximum of only about 92% over the

subsequent 95 cycles. This result indicates the cell with $MoS_2$ 45h separator has highly reversible reaction and less sulfur loss than cells with others separator.

On this basis, to further explore the effects of different separators on stability and capacity, the differences in the first and second cycle charge-discharge curves of CS cells with different separators were compared. As shown in Figure 5.31, the cell with the $MoS_2$ separator exhibits a more rapid voltage decay between 2.4V and 2.0V (corresponding to sulfur→$Na_2S_x$, x=4-8) compared to the GFD separator and CGFD separator. It can due to the excellent catalytic effect of $MoS_2$ that reduces the sulfur conversion reaction barrier to make the reduction of over-potential required for the sulfur conversion reaction. At the same time, the cell with the $MoS_2$ separator delivers almost the same charge capacity as the discharge capacity. This can be due to the anchoring effect of the metal sites in $MoS_2$ on polysulfides, and the promotion of $MoS_2$ on the deposition-conversion of sodium sulfide. The metal sites can promote the efficient deposition of sodium sulfide during discharge and the rapid oxidative decomposition during charge process.

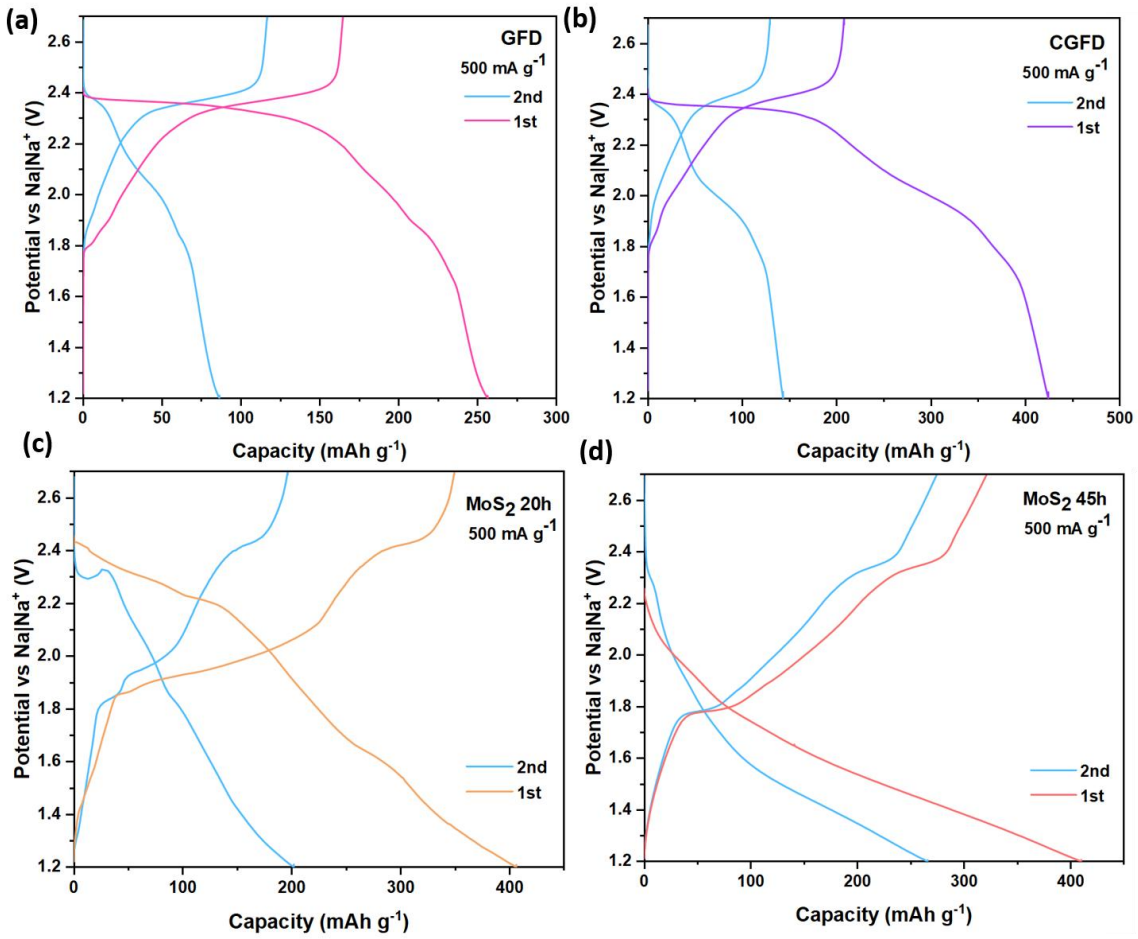


Figure 5.31 Charge-discharge curve of CS cell with different separator (a)GFD, (b) CGFD, (c)$MoS_2$ 20h, (4) $MoS_2$ 45h. (Electrolyte: 1M $NaCF_3SO_3$ in TEGDME, capacity calculated by mass of sulfur, sulfur loading=0.8-1 mg $cm^{-2}$)

In addition, the cell with $MoS_2$ separator has a higher first-cycle discharge capacity and less single-cycle decay due to the catalytic effect of $MoS_2$ on the sulfur polymer-sodium sulfide reaction and the anchoring of polysulfides. As shown in Table 5.4, the cell with $MoS_2$ 45h separator shows a high first-cycle capacity and less single-cycle decay, but the first-cycle capacity is not higher than CGFD separator, which indicate $MoS_2$ 45h separator can provide the greatest improvement in stability, while CGFD separator performs better in capacity enhancement. This further proves that the flaky $MoS_2$ (ball-milled for 45h) has a significant effect on improving the capacity and stability.

Furthermore, Table 5.3 shows the discharge energy of the cells with different separators during the first and second cycle. The cell with CGFD separator delivered the highest initial energy of 0.89 Wh $g^{-1}$, followed by $MoS_2$ 20 h (0.76 Wh $g^{-1}$), $MoS_2$ 45 h (0.64 Wh $g^{-1}$), and GFD (0.55 Wh $g^{-1}$). However, after the second cycle, a pronounced energy decay was observed for all cells, particularly for the CGFD separator (0.60 Wh $g^{-1}$). Among them, the $MoS_2$ 45 h separator exhibited the smallest energy decay (0.22 Wh $g^{-1}$), suggesting its interfacial stability and effective suppression of polysulfide shuttling. In contrast, although cell with CGFD separator providing higher initial energy due to enhanced electronic conductivity, suffered from faster energy fading, likely caused by insufficient anchor of soluble sulfur species. After this, the cell with $MoS_2$ 45 h separator maintains a significantly higher energy, suggesting that it preserves more electrochemically active sulfur (Figure 5.32a). As the current increases to 1000 mA $g^{-1}$ and 2000 mA $g^{-1}$, cells with all separators show further reductions in discharge energy, indicating increasingly sluggish sodium ion transport and more hindered solid-liquid conversion kinetics under high-rate conditions. Notably, the cell with $MoS_2$ 45 h separator provides the highest energy retention across all high-rate regions, which is benefited from large density of catalytically active metal edge sites. These sites enhance the redox conversion of polysulfides and improve interfacial charge transfer, while inhibiting the shuttle effect through chemical adsorption of metal sites. Figure 5.32b shows the variation of energy efficiency for cells with different separators at various current. At 500 mA $g^{-1}$, all cells exhibit an initially energy efficiency more than 100% due to electrode activation. After first cycle, the cell with GFD separator shows the lowest energy efficiency (60-70%), indicating severe polarization and sluggish redox kinetics. In contrast, the cell with $MoS_2$ 45 h and CGFD separators deliver higher efficiencies (>80%), and cell with CGFD is higher than cell with $MoS_2$ 45 h in all rates, reflecting improved charge transfer kinetics and reduced overpotential. As the current increases to 1000 and 2000 mA $g^{-1}$,

the energy efficiency of all cells decreases due to increased polarization at higher rates. The cell with $MoS_2$ separator, particularly the cell with $MoS_2$ 45 h separator, exhibit slightly lower discharge voltages, reflecting the presence of additional interfacial impedance introduced by the $MoS_2$ layer (Figure 5.31). At 2000 mA $g^{-1}$, the cell with GFD separator shows the highest energy efficiency with low capacity, which does not indicate better electrochemical performance. Instead, due to the severe shuttle effect, most active sulfur is already lost during the early cycles. As a result, the cell has a very limited amount of sulfur, the capacity mainly from capacitive behavior of the carbon matrix, the carbon-driven electrochemical processes do not involve phase transitions and long-range ion diffusion[157]. As a result, charge-transfer and diffusion resistances are minimized, leading to a lower polarization. This reduced reaction complexity leads to the higher energy efficiency with the significantly lower capacity. Overall, the CGFD separator enhances the redox kinetics and achieves higher energy in first cycle but suffers from energy decay due to insufficient suppression of polysulfide migration. In contrast, the $MoS_2$ 45h separator provides higher energy and better energy retention, but $MoS_2$ functional layer introduces extra charge-transfer resistance, which results in higher polarization, lower voltage and consequently reduces the energy efficiency.

Table 5.3 First cycle and second cycle of CS cell with different separator (capacity mAh $g^{-1}$, energy: Wh $g^{-1}$)

| **Separator** | **$MoS_2$ 45h** | **$MoS_2$ 20h** | **CGFD (carbon)** | **GFD** |
|---|---|---|---|---|
| Capacity of first cycle | 408.6 | 405.7 | 423.6 | 255.8 |
| Capacity of second cycle | 265.7 | 201.4 | 143.0 | 86.0 |
| **Capacity decay** | **142.9** | **204.3** | **280.6** | **169.8** |
| Energy of first cycle | 0.64 | 0.76 | 0.89 | 0.55 |
| Energy of second cycle | 0.42 | 0.36 | 0.29 | 0.17 |
| **Energy decay** | **0.22** | **0.40** | **0.60** | **0.38** |

The same result can be observed in rate performance (Figure 5.32c) The rate performance of CS cell with different separator is tested between 500mAh $g^{-1}$-2000mAh $g^{-1}$. Figure 5.32c shows the significantly improved rate performance of cell with $MoS_2$ 45h separator. At 500mAh $g^{-1}$, 1000mAh $g^{-1}$, 2000mAh $g^{-1}$, cell with $MoS_2$ 45h separator exhibit specific capacities of 409.80mAh $g^{-1}$, 150.05mAh $g^{-1}$, 111.31mAh $g^{-1}$. At the same time, it also shows 122.21 mAh $g^{-1}$ when back to 500mAh $g^{-1}$, which reflects the help of $MoS_2$ separator in sulfur conversion reaction under high current density.

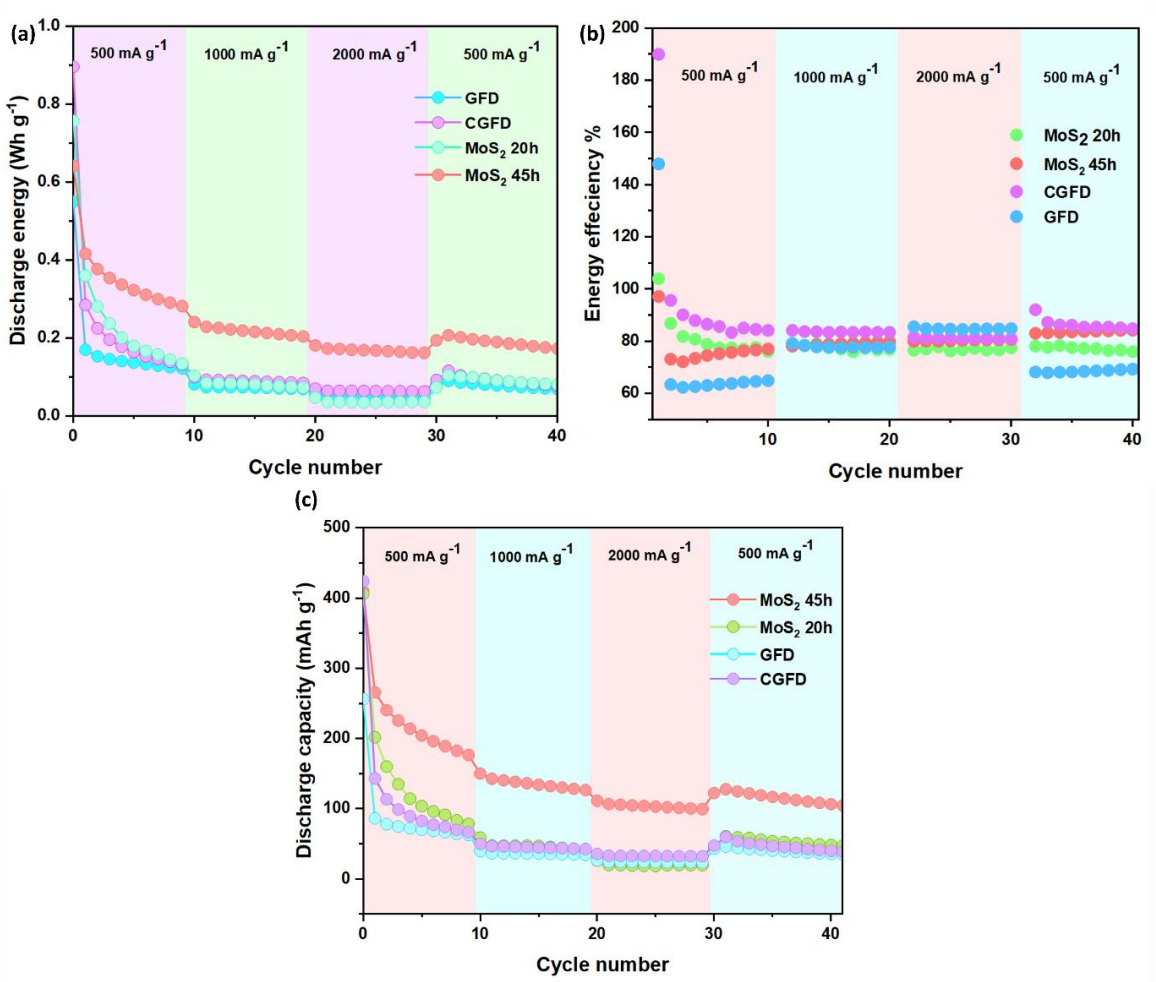


Figure 5.32 (a) Discharge energy in different current of cell with different separator, (b) Energy efficiency in different current of cell with different separator, (c) Rate performance of CS cell with different separator (Electrolyte: 1M $NaCF_3SO_3$ in TEGDME, capacity calculated by mass of sulfur, sulfur loading=0.8-1 mg $cm^{-2}$)

### 5.3.3 Conclusion

The main conclusions and innovations of this chapter are as follows:

(1) Design sulfur distribution. Carbon host of sulfur can effectively solve the challenges of low capacity and high energy barrier of conversion reaction in sulfur-based batteries that is caused by insufficient conductivity of sulfur. On this basis, the sulfur distribution can be designed by synthetic method. In this research, a sulfur carbon composite was synthesized by solvent method adapted from prior reports[148]. This method can obtain the carbon-sulfur

composite with the uniform molecular-level distribution. The improved sulfur-carbon interfacial contact can facilitate charge transfer and ion diffusion during electrochemical reactions, thereby enhancing the reaction kinetics and cycling stability.

(2) Promotion of sulfur conversion reaction kinetics: functional separator can improve the cathode-electrolyte interface of sodium-sulfur batteries to improve the kinetics of sulfur conversion reactions on the positive electrode side through the contact between the functionalized materials and the positive electrode. Meanwhile, functional separators also can anchor the polysulfides from cathode side and inhibit the shuttle effect, thereby improving the capacity and cycle stability of the cell. This research explored the application of functional separators for improving capacity and stability: the $MoS_2$ with different microstructure was applied as functional materials for separators to understand relationship between structures and capacity/stability. Among them, the sheet-like $MoS_2$ obtained by ball milling for 45 hours can provide improvement in capacity due to its abundant metal sites (CE=~100%, 408.6mAh $g^{-1}$ at 500mA $g^{-1}$). By molybdenum metal sites, $MoS_2$ can effectively anchor polysulfides and promote sulfur conversion to improve capacity and stability.

**Authorship Contributions**

The conceptualization and design of the experiments were primarily developed by Liwen Yang under supervision of Prof. Dr. Sonia Dsoke and Prof. Dr. Hatice Mutlu. The CS materials synthesis, cell assembly, and electrochemical testing were performed by Liwen Yang in IAM-ESS of Karlsruhe Institute of Technology. Elemental analysis was conducted and analyzed by Nicole Klaassen. Liwen Yang prepared the manuscript draft, and it was revised under the supervision of Prof. Dr. Sonia Dsoke and Prof. Dr. Hatice Mutlu.

# Chapter 6 Conclusions & Outlook

## 6.1 Conclusions

This thesis investigated different types of sulfur-containing polymers as the positive electrode of RT-Na-S batteries and explores how their designable structure and polymer backbones can address the key challenges of RT Na-S batteries. The main conclusions of the research are as follows:

**(1) The impact of charge-discharge voltage range needs to be carefully considered.** In ether-based electrolytes, deep discharge of a sulfurized polyacrylonitrile (SPAN) cathode promotes excessive polysulfide formation, which then accumulates during the subsequent oxidation step. The resulting shuttle effect induces non-uniform current distribution at the anode, leading to micro short circuit of the cell. More importantly, deep discharge can lead to the accumulation of $S_3^-$ ions and changes in the PAN skeleton structure, resulting in the failure of reform of sulfur chain in SPAN. Reasonable selection of charging and discharging voltage range is crucial for the cell stability when SPAN is used as positive electrode. Within the appropriate charging and discharging range, SPAN positive electrode exhibits excellent discharge specific capacity, rate performance, and cycling stability, significantly better than elemental sulfur positive electrode. The initial capacity of the SPAN electrode is 550mAh $g^{-1}$ at first cycle at 500 mA $g^{-1}$, while elemental sulfur cathode provides less than 100 mAh $g^{-1}$ in first cycle at 500 mA $g^{-1}$. After 100 cycles, 200 mAh $g^{-1}$ of capacity is retained for a SPAN cell, while cells with elemental sulfur shows capacity almost 0 mAh $g^{-1}$. Moreover, the SPAN//Na cell has a coulombic efficiency at around 99.86% during first 20 cycles and stay at 100% during last 80 cycles at 500mA $g^{-1}$. In contrast, the coulombic efficiency of the sulfur cathode is only 60%-80%. Furthermore, the performance of SPAN positive electrode is further improved by using functionalized separators. With the use of carbon functionalized

separators, the SPAN positive electrode can provide a capacity of up to 1787mAh $g^{-1}$ at a current density of 500mA $g^{-1}$, and still provide a capacity of 474 mAh $g^{-1}$ at 500mA $g^{-1}$ after 100 cycles.

**(2) Functional groups of polymers have a strong impact on key-performance indicators.** The selection of functional groups within the polymer backbone plays a decisive role in determining the reversibility of Na-S cells. For instance, the active nitrogen centers in amide groups tend to undergo irreversible reactions with polysulfide, inducing bond reconstruction from C-N to C-S, S-N, or C(=S)-N linkages and partially graphitizing the carbon framework. This irreversible transformation results in chemical fixation of sulfur and prevents the regeneration of sulfur chains, leading to capacity decay and low coulombic efficiency. Therefore, the molecular design of polymer cathodes should avoid functional groups containing highly reactive sites and instead introduce electronically stabilized or dynamically reconfigurable functional group. Such a design can prevent the formation of irreversible covalent bonds while maintaining interactions with polysulfides. In addition, the construction of highly conductive polymer frameworks and the coordinated optimization of electrolytes and operating potential windows are also critical to achieving stable and reversible Na-S battery performance.

**(3) Functional separator design.** Functional separators can be precisely designed according to specific requirements. For example, metal compounds with amount of metal sites can enable functional separator to regulate the electrochemical reaction kinetics between sulfur and sodium, in same time can anchor polysulfides generated during the reaction between sulfur and sodium by metal sites to inhibit shuttle effects; The use of carbon materials can enable functional separators to act as "additional electronic conductive path", thereby promoting charge transfer to the positive electrode. At the same time, carbon materials can physically confine polysulfides by porous structure and functional group. In Chapter 5 of this

thesis, different functional separators were used to improve the performance of sodium-sulfur cells in terms of specific capacity and cycling stability. According to the results in section 5.3, the sheet-like metal sulfide obtained by 45h mechanical ball milling has higher surface with metal sites, thereby exhibiting superior in anchoring polysulfides and catalyzing sulfur metal conversion reactions. Carbon-modified separator has impressive effects in increasing the initial capacity, this indicates that the carbon helps to increase the sulfur utilization in the first cycles, but does not suppress shuttling. Consequently, more sulfur dissolves into the electrolyte and still shuttles. The cell with carbon functional separator still requires optimization to improve stability. The functional separator can be seen as a simplified version of the positive electrode functionalization scheme that does not require a high-temperature sulfur loading process.

### 6.2 Outlook

In recent years, researchers in RT sodium-sulfur batteries have proposed numerous effective measures to suppress the diffusion of polysulfides. The regulation strategies for polysulfides range from simple physical adsorption barriers to chemical adsorption, and then to catalysis of the conversion process. These studies are almost limited to the use of elemental sulfur as the positive electrode, and there are still promising possibilities for the application of polymers in RT Na-S batteries. Based on the summary of recent research and the conclusion of this thesis, there are still the following challenges in the application of polymer cathodes in RT Na-S batteries:

**(1) Complex reaction mechanism.** Polymers contain different functional groups and structures, and the sulfur chain length is not fixed. This means different polymers positive electrode will have different reaction pathways with sodium metal. In addition, during the reaction process, the structure of the polymer itself may change, which further leads to

different reaction mechanisms for different polymers. Compared with the relatively fixed reaction mechanism of elemental sulfur, sulfur-containing polymers exhibit diverse electrochemical behaviors depending on their molecular structures, which makes their reaction processes more complex to study. Therefore, it is essential to develop a deeper understanding of their reaction mechanisms and to optimize the corresponding control strategies. On this basis, sulfur-containing polymers should be systematically investigated according to their structural types to establish structure-mechanism correlations that can guide future research and material design. To gain deeper insight into the electrochemical behavior of sulfur-containing polymers, future research should integrate advanced *in-situ* characterization techniques with theoretical modeling approaches. *In-situ* methods (such as *in-situ* Raman spectroscopy, FTIR spectroscopy, XRD, XPS, and X-ray absorption spectroscopy) can provide real-time information on bond evolution, phase transitions, and valence state changes during electrochemical cycling. Moreover, theoretical calculation such as density functional theory (DFT) and molecular dynamics (MD) simulations can explain polymer-polysulfide interactions, reaction energetics, and interfacial evolution at the atomic scale.

**(2) Conductive skeleton design.** A considerable amount of carbon material is typically incorporated as a conductive additive to facilitate efficient charge transfer in polymer positive electrode with low electronic conductivity. Although increasing the carbon content can effectively enhance the electrical conductivity of the electrode, it will reduce the overall energy density. Therefore, it is important to explore the strategy that can maximize the intrinsic conductivity of the active material without compromising energy density and promote both ionic and electronic transport within sulfur-containing polymer positive electrode.

**(3) The inhibition of shuttle effect and effective regulation of sulfur conversion reaction.**

Future research should focus on the rational selection of physical and chemical adsorption materials, and the realization of rapid sulfur conversion reactions through the catalytic materials. It is important to have a clear understanding of the catalytic mechanisms, such as the transformation pathways during sulfur conversion and the interaction between functional material and polysulfide. Moreover, further studies should focus on the reaction mechanisms of Na-S batteries and the evolution of sulfur species on positive-electrolyte interface. To achieve this, a combination of advanced *in-situ* and *ex-situ* characterization techniques is essential. *In-situ* Raman and FTIR spectroscopy can track the formation and conversion of polysulfide intermediates in real time, while X-ray photoelectron spectroscopy (XPS) and X-ray absorption spectroscopy (XAS) can offer valuable insights into chemical-state transitions and the local coordination environments of sulfur species. High-resolution transmission electron microscopy (HRTEM) and *in-situ* X-ray diffraction (XRD) can further reveal the structural evolution of active materials during electrochemical cycling. In addition, *in-situ* electrochemical methods (such as *in-situ* electrochemical impedance spectroscopy (EIS)) enable direct correlation between interfacial chemical changes and capacity. By these experimental techniques, a multi-scale understanding of sulfur species evolution at the electrode-electrolyte interface can be achieved.

In summary, the application of sulfur-containing polymers in RT Na-S batteries requires comprehensive investigations into their structure, reaction mechanisms, and electrochemical performance. Such studies should be supported by advanced chemical characterization techniques and emerging materials science approaches to develop integrated and systematic solutions for next-generation Na-S batteries.

# Acknowledgement

It was since 10/2022 when I officially started my PhD work at the Department of Chemistry and Biosciences (Karlsruhe Institute of Technology, KIT), Institute for Applied Materials - Energy Storage Systems (IAM-ESS). It's a great pleasure to thank the financial support from China Scholarship Council (CSC, No. 202206240016). Many thanks go to people who kept offering me help and conduct.

First of all, I would like to express my sincere gratitude to my supervisor Prof. Dr. Helmut Ehrenberg, who gave me the chance to do research work at IAM-ESS. I am grateful for his great support, value guidance and comments.

I would like to express my sincere gratitude to my co-supervisor, Prof. Dr. Sonia Dsoke, for her meticulous guidance to my research. She consistently identifies the core scientific questions, offers unique insights, and inspires new directions in my work. She has outstanding insights and extensive knowledge in the field of electrochemistry/energy storage, and is passionate and uniquely inspired by research. Her constructive advice has also greatly helped me improve my presentation skills. I have gained invaluable knowledge and deepened my scientific understanding through her wisdom, encouragement, and continuous support.

I would also like to express my sincere thanks to my second supervisor, Prof. Dr. Hatice Mutlu, for her dedicated guidance in polymer synthesis and organic chemistry. Her passion for scientific research and unwavering enthusiasm have been a constant source of inspiration. She has provided tremendous support in polymer synthesis and has offered insightful advice that has shaped my research ideas. Through her professionalism, encouragement, and guidance, I have developed a strong enthusiasm for research and acquired a profound understanding of polymer science.

I am grateful to Dr. Angelina Sarapulova for her detailed discussions with me on scientific research issues and for providing me with a lot of help in my laboratory work. Many thanks

go to my group leader Dr. Fabian Jeschull for insightful guidance and invaluable suggestions to my research, as well as for his dedicated leadership and continuous support in managing our research group. I would also like to thank Xinyue Li and Kun Tang for them help and support and patiently answering my questions at all times. Many thanks are also given to Hao Liu and Bijian Deng for them help in data analysis. The help from my colleagues at IAM-ESS: Liuda Mereacre (essential support in the lab), Mrs. Almut Kriese (administrative support), Mr. Luis Martin Sanchez Neudeck (IT support) are gratefully acknowledged.

I would like to express my gratitude to my collaborator Dr. Rong Li for support with in-situ Raman, which have played a crucial role in my research about mechanisms. Many thanks to Xinyue Zhang, Shuaiwei Liu and Ying Li for their valuable scientific discussion with me.

I would like to express my heartfelt gratitude to my dear friends who have always been by my side: Xinying, Dongyue, Ruoyun, Yiling, Liyu, Xiaoxi, and Ran. We have shared both joyful and difficult moments in life, and your companionship has given me the courage to persevere in the face of challenges, as well as the strength to move forward with confidence.

I am also deeply thankful for the wonderful new bonds that have entered my life like hidden treasures. My sincere thanks go to Liu Yang for her constant companionship, mutual support, and emotional understanding. Her selfless help and steady presence have given me a lasting sense of security in a foreign land.

I am grateful as well to the friends connected to me through the internet. Many thanks to Shuang Kou E for our shared resonance of thought and effortless understanding, her insightful advice has inspired me to grow into a better version of myself. Thanks to Bi Lei Zhen for his optimism and remarkable emotional resilience that have been a great source of encouragement. I would also like to extend my appreciation to all the friends I have met in the online world. The joyful moments and challenges we have shared have offered me steady

and positive energy, helping me rise again from disappointment and face the obstacles of scientific research with renewed courage.

Finally, my deepest gratitude goes to my parents, the steadfast foundation of my life, for their enduring trust and support, and always trusting and guarding.

# Reference

[1] “Post-lithium-ion battery cell production and its compatibility with lithium-ion cell production infrastructure | Nature Energy.” Accessed: Sep. 02, 2025. [Online]. Available: https://www.nature.com/articles/s41560-020-00748-8

[2] M. S. Syali, D. Kumar, K. Mishra, and D. K. Kanchan, “Recent advances in electrolytes for room-temperature sodium-sulfur batteries: A review,” *Energy Storage Mater.*, vol. 31, pp. 352–372, Oct. 2020, doi: 10.1016/j.ensm.2020.06.023.

[3] M. Wang, H. Zhang, W. Zhang, Q. Chen, and K. Lu, “Electrocatalysis in Room Temperature Sodium-Sulfur Batteries: Tunable Pathway of Sulfur Speciation,” *Small Methods*, vol. 6, no. 7, p. 2200335, 2022, doi: 10.1002/smtd.202200335.

[4] Y.-X. Wang *et al.*, “Room-Temperature Sodium-Sulfur Batteries: A Comprehensive Review on Research Progress and Cell Chemistry,” *Adv. Energy Mater.*, vol. 7, no. 24, p. 1602829, 2017, doi: 10.1002/aenm.201602829.

[5] G. Nikiforidis, G. J. Jongerden, E. F. Jongerden, M. C. M. van de Sanden, and M. N. Tsampas, “An Electrochemical Study on the Cathode of the Intermediate Temperature Tubular Sodium-Sulfur (NaS) Battery,” *J. Electrochem. Soc.*, vol. 166, no. 2, p. A135, Jan. 2019, doi: 10.1149/2.0491902jes.

[6] F. Jin *et al.*, “Conversion mechanism of sulfur in room-temperature sodium-sulfur battery with carbonate-based electrolyte,” *Energy Storage Mater.*, vol. 69, p. 103388, May 2024, doi: 10.1016/j.ensm.2024.103388.

[7] S. Li *et al.*, “N,S-codoped carbon dots as deposition regulating electrolyte additive for stable lithium metal anode,” *Energy Storage Mater.*, vol. 42, pp. 679–686, Nov. 2021, doi: 10.1016/j.ensm.2021.08.008.

[8] M. Wild *et al.*, “Lithium sulfur batteries, a mechanistic review,” *Energy Environ. Sci.*, vol. 8, no. 12, pp. 3477–3494, Nov. 2015, doi: 10.1039/C5EE01388G.

[9] “Manipulating the Electronic Structure of Nickel via Alloying with Iron: Toward High-Kinetics Sulfur Cathode for Na–S Batteries | ACS Nano.” Accessed: Sep. 02, 2025. [Online]. Available: https://pubs.acs.org/doi/10.1021/acsnano.1c05778

[10] J. Lei *et al.*, “Exploring and Understanding the Roles of Li2Sn and the Strategies to beyond Present Li-S Batteries,” *Chem*, vol. 6, no. 10, pp. 2533–2557, Oct. 2020, doi: 10.1016/j.chempr.2020.06.032.

[11] Y. C. Jeong, J. H. Kim, S. Nam, C. R. Park, and S. J. Yang, “Rational Design of Nanostructured Functional Interlayer/Separator for Advanced Li–S Batteries,” *Adv. Funct. Mater.*, vol. 28, no. 38, p. 1707411, 2018, doi: 10.1002/adfm.201707411.

[12] M. R. Busche, P. Adelhelm, H. Sommer, H. Schneider, K. Leitner, and J. Janek, “Systematical electrochemical study on the parasitic shuttle-effect in lithium-sulfur-cells at different temperatures and different rates,” *J. Power Sources*, vol. 259, pp. 289–299, Aug. 2014, doi: 10.1016/j.jpowsour.2014.02.075.

[13] “Architecting Freestanding Sulfur Cathodes for Superior Room-Temperature Na–S Batteries - Yang - 2021 - Advanced Functional Materials - Wiley Online Library.” Accessed: Sep. 02, 2025. [Online]. Available: https://advanced.onlinelibrary.wiley.com/doi/10.1002/adfm.202102280

[14] H. Wu, D. Zhuo, D. Kong, and Y. Cui, “Improving battery safety by early detection of internal shorting with a bifunctional separator,” *Nat. Commun.*, vol. 5, no. 1, p. 5193, Oct. 2014, doi: 10.1038/ncomms6193.

[15] “Dual-Phase Lithium Metal Anode Containing a Polysulfide-Induced Solid Electrolyte Interphase and Nanostructured Graphene Framework for Lithium–Sulfur Batteries | ACS Nano.” Accessed: Sep. 02, 2025. [Online]. Available: https://pubs.acs.org/doi/10.1021/acsnano.5b01990

[16] L. Zhou *et al.*, “Engineering Sodium-Ion Solvation Structure to Stabilize Sodium Anodes: Universal Strategy for Fast-Charging and Safer Sodium-Ion Batteries,” *Nano Lett.*, vol. 20, no. 5, pp. 3247–3254, May 2020, doi: 10.1021/acs.nanolett.9b05355.

[17] G. Li, X. Lou, C. Peng, C. Liu, and W. Chen, “Interface chemistry for sodium metal anodes/batteries: a review,” *Chem. Synth.*, vol. 2, no. 3, p. N/A-N/A, Sep. 2022, doi: 10.20517/cs.2022.19.

[18] “Electrolyte Additives for Room-Temperature, Sodium-Based, Rechargeable Batteries - Eshetu - 2018 - Chemistry – An Asian Journal - Wiley Online Library.” Accessed: Sep. 02, 2025. [Online]. Available: https://aces.onlinelibrary.wiley.com/doi/10.1002/asia.201800839

[19] F. Zhao, Y. Li, and W. Feng, “Recent Advances in Applying Vulcanization/Inverse Vulcanization Methods to Achieve High-Performance Sulfur-Containing Polymer Cathode Materials for Li–S Batteries,” *Small Methods*, vol. 2, no. 11, p. 1800156, 2018, doi: 10.1002/smtd.201800156.

[20] “Intrinsic differences and realistic perspectives of lithium-sulfur and magnesium-sulfur batteries | Communications Materials.” Accessed: Sep. 02, 2025. [Online]. Available: https://www.nature.com/articles/s43246-021-00143-0

[21] Y. Qi and M. Xu, “Engineering towards stable sodium metal anodes in room temperature sodium-sulfur batteries: challenges, progress and perspectives,” *Energy Storage Mater.*, vol. 72, p. 103704, Sep. 2024, doi: 10.1016/j.ensm.2024.103704.

[22] L. Lin *et al.*, “Challenge and Strategies in Room Temperature Sodium–Sulfur Batteries: A Comparison with Lithium–Sulfur Batteries,” *Small*, vol. 18, no. 43, p. 2107368, 2022, doi: 10.1002/smll.202107368.

[23] Y. Liang, B. Zhang, Y. Shi, R. Jiang, and H. Zhang, “Research on Wide-Temperature Rechargeable Sodium-Sulfur Batteries: Features, Challenges and Solutions,” *Materials*, vol. 16, no. 12, p. 4263, Jan. 2023, doi: 10.3390/ma16124263.

[24] H. Li *et al.*, “Anode-free sodium metal batteries: optimisation of electrolytes and interphases,” *Energy Environ. Sci.*, vol. 18, no. 9, pp. 3887–3916, 2025, doi: 10.1039/D5EE00136F.

[25] Y. Wang *et al.*, “Strategies to mitigate the shuttle effect in room temperature sodium–sulfur batteries: improving cathode materials,” *Dalton Trans.*, vol. 52, no. 9, pp. 2548–2560, Feb. 2023, doi: 10.1039/D3DT00008G.

[26] S.-H. Chung, C.-H. Chang, and A. Manthiram, “Progress on the Critical Parameters for Lithium–Sulfur Batteries to be Practically Viable,” *Adv. Funct. Mater.*, vol. 28, no. 28, p. 1801188, 2018, doi: 10.1002/adfm.201801188.

[27] A. G. Simmonds *et al.*, “Inverse Vulcanization of Elemental Sulfur to Prepare Polymeric Electrode Materials for Li–S Batteries,” *ACS Macro Lett.*, vol. 3, no. 3, pp. 229–232, Mar. 2014, doi: 10.1021/mz400649w.

[28] G. Gao, X. Sun, and L.-W. Wang, “An inverse vulcanized conductive polymer for Li–S battery cathodes,” *J. Mater. Chem. A*, vol. 8, no. 41, pp. 21711–21720, Oct. 2020, doi: 10.1039/D0TA06537D.

[29] Z. Chen *et al.*, “Sulfur-anchored azulene as a cathode material for Li–S batteries,” *Chem. Commun.*, vol. 55, no. 61, pp. 9047–9050, Jul. 2019, doi: 10.1039/C9CC04413B.

[30] Y. Wang *et al.*, “Covalently Grafting Sulfur-Containing Polymers to Carbon Nanotubes Enhances the Electrochemical Performance of Sulfur Cathodes,” *ACS Appl. Polym. Mater.*, vol. 4, no. 2, pp. 939–949, Feb. 2022, doi: 10.1021/acsapm.1c01398.

[31] S. Yeşilot, S. Küçükköylü, T. Mutlu, and R. Demir-Cakan, “Halogen-Free Polyphosphazene-Based Flame Retardant Cathode Materials for Li–S Batteries,” *Energy Technol.*, vol. 9, no. 12, p. 2100563, 2021, doi: 10.1002/ente.202100563.

[32] S. Yeşilot, S. Küçükköylü, E. Demir, and R. Demir-Cakan, “Phosphazene based star-branched polymeric cathode materials via inverse vulcanization of sulfur for lithium–sulfur batteries,” *Polym. Chem.*, vol. 11, no. 25, pp. 4124–4132, Jun. 2020, doi: 10.1039/D0PY00490A.

[33] S. H. Je *et al.*, “Rational Sulfur Cathode Design for Lithium–Sulfur Batteries: Sulfur-Embedded Benzoxazine Polymers,” *ACS Energy Lett.*, vol. 1, no. 3, pp. 566–572, Sep. 2016, doi: 10.1021/acsenergylett.6b00245.

[34] C. Krishnaraj, H. S. Jena, K. Leus, and P. V. D. Voort, “Covalent triazine frameworks – a sustainable perspective,” *Green Chem.*, vol. 22, no. 4, pp. 1038–1071, Feb. 2020, doi: 10.1039/C9GC03482J.

[35] S. N. Talapaneni, T. H. Hwang, S. H. Je, O. Buyukcakir, J. W. Choi, and A. Coskun, “Elemental-Sulfur-Mediated Facile Synthesis of a Covalent Triazine Framework for High-Performance Lithium–Sulfur Batteries,” *Angew. Chem. Int. Ed.*, vol. 55, no. 9, pp. 3106–3111, 2016, doi: 10.1002/anie.201511553.

[36] “Fluorinated, Sulfur-Rich, Covalent Triazine Frameworks for Enhanced Confinement of Polysulfides in Lithium–Sulfur Batteries | ACS Applied Materials & Interfaces.” Accessed: Sep. 02, 2025. [Online]. Available: https://pubs.acs.org/doi/10.1021/acsami.7b10991

[37] X. Wang *et al.*, “Sulfurized Polyacrylonitrile Cathodes with High Compatibility in Both Ether and Carbonate Electrolytes for Ultrastable Lithium–Sulfur Batteries,” *Adv. Funct. Mater.*, vol. 29, no. 39, p. 1902929, 2019, doi: 10.1002/adfm.201902929.

[38] S. H. Je, H. J. Kim, J. Kim, J. W. Choi, and A. Coskun, “Perfluoroaryl-Elemental Sulfur SNAr Chemistry in Covalent Triazine Frameworks with High Sulfur Contents for

Lithium–Sulfur Batteries," *Adv. Funct. Mater.*, vol. 27, no. 47, p. 1703947, 2017, doi: 10.1002/adfm.201703947.

[39] J. Zhou *et al.*, "Selenium-Doped Cathodes for Lithium–Organosulfur Batteries with Greatly Improved Volumetric Capacity and Coulombic Efficiency," *Adv. Mater.*, vol. 29, no. 33, p. 1701294, 2017, doi: 10.1002/adma.201701294.

[40] J. Fanous, M. Wegner, J. Grimminger, Ä. Andresen, and M. R. Buchmeiser, "Structure-Related Electrochemistry of Sulfur-Poly(acrylonitrile) Composite Cathode Materials for Rechargeable Lithium Batteries," *Chem. Mater.*, vol. 23, no. 22, pp. 5024–5028, Nov. 2011, doi: 10.1021/cm202467u.

[41] "Easily Accessible, Textile Fiber-Based Sulfurized Poly(acrylonitrile) as Li/S Cathode Material: Correlating Electrochemical Performance with Morphology and Structure | ACS Energy Letters." Accessed: Sep. 02, 2025. [Online]. Available: https://pubs.acs.org/doi/10.1021/acsenergylett.7b00009

[42] Q. Sun, X.-M. Zhang, L. Liu, D.-C. Guo, Z.-B. Feng, and P. Lu, "Engineering of polymeric disulfide nanosheet cathode for highly durable lithium-sulfur battery," *Appl. Surf. Sci.*, vol. 526, p. 146754, Oct. 2020, doi: 10.1016/j.apsusc.2020.146754.

[43] M. B. Preefer, B. Oschmann, C. J. Hawker, R. Seshadri, and F. Wudl, "High Sulfur Content Material with Stable Cycling in Lithium-Sulfur Batteries," *Angew. Chem. Int. Ed.*, vol. 56, no. 47, pp. 15118–15122, 2017, doi: 10.1002/anie.201708746.

[44] "Poly(anthraquinonyl sulfides): High Capacity Redox Polymers for Energy Storage | ACS Macro Letters." Accessed: Sep. 02, 2025. [Online]. Available: https://pubs.acs.org/doi/10.1021/acsmacrolett.8b00154

[45] "Polyphenylene Tetrasulfide as an Inherently Flexible Cathode Material for Rechargeable Lithium Batteries | ACS Applied Energy Materials." Accessed: Sep. 02, 2025. [Online]. Available: https://pubs.acs.org/doi/10.1021/acsaem.8b01350

[46] S. Zeng *et al.*, “Polymer-Capped Sulfur Copolymers as Lithium–Sulfur Battery Cathode: Enhanced Performance by Combined Contributions of Physical and Chemical Confinements,” *J. Phys. Chem. C*, vol. 121, no. 5, pp. 2495–2503, Feb. 2017, doi: 10.1021/acs.jpcc.6b09543.

[47] C.-H. Tsao, C.-H. Hsu, J.-D. Zhou, C.-W. Chin, P.-L. Kuo, and C.-H. Chang, “Vulcanized polymeric cathode material featuring a polyaniline skeleton for high-rate rechargeability and long-cycle stability lithium-sulfur batteries,” *Electrochimica Acta*, vol. 276, pp. 111–117, Jun. 2018, doi: 10.1016/j.electacta.2018.04.013.

[48] H. Zou *et al.*, “Nitrogen-doped porous carbon hosted sulfur-rich polymer for room temperature Na-S batteries with superior cycle performances,” *Electrochimica Acta*, vol. 486, p. 144154, May 2024, doi: 10.1016/j.electacta.2024.144154.

[49] N. Wang *et al.*, “Rational design of Co9S8/CoO heterostructures with well-defined interfaces for lithium sulfur batteries: A study of synergistic adsorption-electrocatalysis function,” *Nano Energy*, vol. 60, pp. 332–339, Jun. 2019, doi: 10.1016/j.nanoen.2019.03.060.

[50] Z. Chang *et al.*, “Co3O4 nanoneedle arrays as a multifunctional ‘super-reservoir’ electrode for long cycle life Li–S batteries,” *J. Mater. Chem. A*, vol. 5, no. 1, pp. 250–257, Dec. 2016, doi: 10.1039/C6TA07202J.

[51] L. Luo, J. Li, H. Yaghoobnejad Asl, and A. Manthiram, “In-Situ Assembled VS4 as a Polysulfide Mediator for High-Loading Lithium–Sulfur Batteries,” *ACS Energy Lett.*, vol. 5, no. 4, pp. 1177–1185, Apr. 2020, doi: 10.1021/acsenergylett.0c00292.

[52] “SnO2/Reduced Graphene Oxide Interlayer Mitigating the Shuttle Effect of Li–S Batteries | ACS Applied Materials & Interfaces.” Accessed: Sep. 02, 2025. [Online]. Available: https://pubs.acs.org/doi/10.1021/acsami.8b03255

[53] N. Li, X. Ma, H. Ye, S. Wang, and K. Han, “Carbon nanotube-modified separator for lithium–sulfur batteries: Effects of mass loading and adding polyvinylpyrrolidone on

electrochemical performance," *J. Phys. Chem. Solids*, vol. 134, pp. 69–76, Nov. 2019, doi: 10.1016/j.jpcs.2019.05.045.

[54] J. Cui *et al.*, "An atomic-confined-space separator for high performance lithium–sulfur batteries," *J. Mater. Chem. A*, vol. 8, no. 4, pp. 1896–1903, Jan. 2020, doi: 10.1039/C9TA11250B.

[55] Y. Li *et al.*, "CoFe2O4@rGO as a Separator Coating for Advanced Lithium–Sulfur Batteries," *Small Sci.*, vol. 3, no. 8, p. 2300045, 2023, doi: 10.1002/smsc.202300045.

[56] Y. Li *et al.*, "Separator decoration with nitrogen-doped porous carbon derived from resin for highly efficient polysulfides confinement in lithium sulfur batteries," *J. Energy Storage*, vol. 112, p. 115566, Mar. 2025, doi: 10.1016/j.est.2025.115566.

[57] K. Zhang *et al.*, "Single-Atom Coated Separator for Robust Lithium–Sulfur Batteries," *ACS Appl. Mater. Interfaces*, vol. 11, no. 28, pp. 25147–25154, Jul. 2019, doi: 10.1021/acsami.9b05628.

[58] "An Anionic-MOF-Based Bifunctional Separator for Regulating Lithium Deposition and Suppressing Polysulfides Shuttle in Li–S Batteries - Wang - 2020 - Small Methods - Wiley Online Library." Accessed: Sep. 02, 2025. [Online]. Available: https://onlinelibrary.wiley.com/doi/full/10.1002/smtd.202000082

[59] "Single-Atom Zinc and Anionic Framework as Janus Separator Coatings for Efficient Inhibition of Lithium Dendrites and Shuttle Effect | ACS Nano." Accessed: Sep. 02, 2025. [Online]. Available: https://pubs.acs.org/doi/10.1021/acsnano.1c03876

[60] J. He, Y. Chen, and A. Manthiram, "Vertical Co9S8 hollow nanowall arrays grown on a Celgard separator as a multifunctional polysulfide barrier for high-performance Li–S batteries," *Energy Environ. Sci.*, vol. 11, no. 9, pp. 2560–2568, Sep. 2018, doi: 10.1039/C8EE00893K.

[61] J. Wang, T. Wu, S. Zhang, S. Gu, J. Jin, and Z. Wen, “Metal-organic-framework-derived N-C-Co film as a shuttle-suppressing interlayer for lithium sulfur battery,” *Chem. Eng. J.*, vol. 334, pp. 2356–2362, Feb. 2018, doi: 10.1016/j.cej.2017.11.180.

[62] “MOF-Derived MnS/N–C@CNT Composites as Separator Coating Materials for Long-Cycling Li–S Batteries | ACS Sustainable Chemistry & Engineering.” Accessed: Sep. 02, 2025. [Online]. Available: https://pubs.acs.org/doi/10.1021/acssuschemeng.1c04636

[63] B. Li *et al.*, “MOF-derived NiCo2S4@C as a separator modification material for high-performance lithium-sulfur batteries,” *Electrochimica Acta*, vol. 344, p. 135811, Jun. 2020, doi: 10.1016/j.electacta.2020.135811.

[64] C.-L. Song *et al.*, “3D catalytic MOF-based nanocomposite as separator coatings for high-performance Li-S battery,” *Chem. Eng. J.*, vol. 381, p. 122701, Feb. 2020, doi: 10.1016/j.cej.2019.122701.

[65] Z. Zhou *et al.*, “MOF-Derived Co3O4 Polyhedrons as Efficient Polysulfides Barrier on Polyimide Separators for High Temperature Lithium–Sulfur Batteries,” *Nanomaterials*, vol. 9, no. 11, p. 1574, Nov. 2019, doi: 10.3390/nano9111574.

[66] J. Wang *et al.*, “An electrochemical sensor based on MOF-derived NiO@ZnO hollow microspheres for isoniazid determination,” *Microchim. Acta*, vol. 187, no. 7, p. 380, Jun. 2020, doi: 10.1007/s00604-020-04305-8.

[67] G. Jiang *et al.*, “*In-situ* decoration of MOF-derived carbon on nitrogen-doped ultrathin MXene nanosheets to multifunctionalize separators for stable Li-S batteries,” *Chem. Eng. J.*, vol. 373, pp. 1309–1318, Oct. 2019, doi: 10.1016/j.cej.2019.05.119.

[68] “Boosting High-Rate Li–S Batteries by an MOF-Derived Catalytic Electrode with a Layer-by-Layer Structure - Li - 2019 - Advanced Science - Wiley Online Library.” Accessed: Sep. 02, 2025. [Online]. Available: https://advanced.onlinelibrary.wiley.com/doi/full/10.1002/advs.201802362

[69] N. Wu *et al.*, “A flame retardant separator modified by MOFs-derived hybrid for safe and efficient Li-S batteries,” *J. Energy Chem.*, vol. 64, pp. 372–384, Jan. 2022, doi: 10.1016/j.jechem.2021.05.001.

[70] S. Suriyakumar and A. M. Stephan, “Mitigation of Polysulfide Shuttling by Interlayer/Permselective Separators in Lithium–Sulfur Batteries,” *ACS Appl. Energy Mater.*, vol. 3, no. 9, pp. 8095–8129, Sep. 2020, doi: 10.1021/acsaem.0c01354.

[71] M. E. Spahr, D. Goers, A. Leone, S. Stallone, and E. Grivei, “Development of carbon conductive additives for advanced lithium ion batteries,” *J. Power Sources*, vol. 196, no. 7, pp. 3404–3413, Apr. 2011, doi: 10.1016/j.jpowsour.2010.07.002.

[72] X. Lu *et al.*, “Effect of carbon blacks on electrical conduction and conductive binder domain of next-generation lithium-ion batteries,” *J. Power Sources*, vol. 592, p. 233916, Feb. 2024, doi: 10.1016/j.jpowsour.2023.233916.

[73] W. Wang *et al.*, “Comparative Study of Water-Based LA133 and CMC/SBR Binders for Sulfur Cathode in Advanced Lithium–Sulfur Batteries,” *J. Phys. Chem. C*, vol. 123, no. 1, pp. 250–257, Jan. 2019, doi: 10.1021/acs.jpcc.8b10736.

[74] T. Hasell, “Investigating the Role and Scope of Catalysts in Inverse Vulcanization | ACS Catalysis,” *ACS Catal*, vol. 2021, no. 11, p. 4441−4455, 2021.

[75] L. J. Dodd, “Inverse vulcanisation: a new Starter’s guide to an emerging field,” *RSC Appl. Polym.*, vol. 3, no. 1, pp. 10–42, Jan. 2025, doi: 10.1039/D4LP00255E.

[76] C. Lv *et al.*, “Characterization of elemental sulfur in chalcopyrite leach residues using simultaneous thermal analysis,” *Hydrometallurgy*, vol. 188, pp. 22–30, Sep. 2019, doi: 10.1016/j.hydromet.2019.05.020.

[77] L. Xue *et al.*, “In Situ/Operando Raman Techniques in Lithium–Sulfur Batteries,” *Small Struct.*, vol. 3, no. 3, p. 2100170, 2022, doi: 10.1002/sstr.202100170.

[78] W. Zhu *et al.*, “Investigation of the reaction mechanism of lithium sulfur batteries in different electrolyte systems by in situ Raman spectroscopy and in situ X-ray diffraction,” *Sustain. Energy Fuels*, vol. 1, no. 4, pp. 737–747, May 2017, doi: 10.1039/C6SE00104A.

[79] J. Hannauer, J. Scheers, J. Fullenwarth, B. Fraisse, L. Stievano, and P. Johansson, “The Quest for Polysulfides in Lithium–Sulfur Battery Electrolytes: An Operando Confocal Raman Spectroscopy Study,” *ChemPhysChem*, vol. 16, no. 13, pp. 2709–2709, 2015, doi: 10.1002/cphc.201500708.

[80] “Present and Future of Surface-Enhanced Raman Scattering | ACS Nano.” Accessed: Sep. 15, 2025. [Online]. Available: https://pubs.acs.org/doi/10.1021/acsnano.9b04224?src=getftr&utm_source=wiley&getft_integrator=wiley

[81] L. Zhao *et al.*, “A Critical Review on Room-Temperature Sodium-Sulfur Batteries: From Research Advances to Practical Perspectives,” *Adv. Mater.*, vol. 36, no. 25, p. 2402337, 2024, doi: 10.1002/adma.202402337.

[82] S. Wei, H. Zhang, Y. Huang, W. Wang, Y. Xia, and Z. Yu, “Pig bone derived hierarchical porous carbon and its enhanced cycling performance of lithium–sulfur batteries,” *Energy Environ. Sci.*, vol. 4, no. 3, pp. 736–740, Mar. 2011, doi: 10.1039/C0EE00505C.

[83] G. Zheng, Y. Yang, J. J. Cha, S. S. Hong, and Y. Cui, “Hollow Carbon Nanofiber-Encapsulated Sulfur Cathodes for High Specific Capacity Rechargeable Lithium Batteries,” *Nano Lett.*, vol. 11, no. 10, pp. 4462–4467, Oct. 2011, doi: 10.1021/nl2027684.

[84] X. Yao *et al.*, “Metal/Graphene Composites with Strong Metal–S Bondings for Sulfur Immobilization in Li–S Batteries,” *J. Phys. Chem. C*, vol. 122, no. 6, pp. 3263–3272, Feb. 2018, doi: 10.1021/acs.jpcc.7b12063.

[85] T. Ma *et al.*, “A review of organic sulfur applications in lithium-sulfur batteries,” *J. Power Sources*, vol. 625, p. 235717, Jan. 2025, doi: 10.1016/j.jpowsour.2024.235717.

[86] H. Kim *et al.*, “Enhanced reversible capacity of sulfurized polyacrylonitrile cathode for room-temperature Na/S batteries by electrochemical activation,” *Chem. Eng. J.*, vol. 426, p. 130787, Dec. 2021, doi: 10.1016/j.cej.2021.130787.

[87] “A Highly Reversible Room-Temperature Sodium Metal Anode | ACS Central Science.” Accessed: Sep. 30, 2025. [Online]. Available: https://pubs.acs.org/doi/full/10.1021/acscentsci.5b00328

[88] D. Liu *et al.*, “Stable Room-Temperature Sodium–Sulfur Batteries in Ether-Based Electrolytes Enabled by the Fluoroethylene Carbonate Additive,” *ACS Appl. Mater. Interfaces*, vol. 14, no. 5, pp. 6658–6666, Feb. 2022, doi: 10.1021/acsami.1c21059.

[89] S. Murugan, S. V. Klostermann, P. Schützendübe, G. Richter, J. Kästner, and M. R. Buchmeiser, “Stable Cycling of Room-Temperature Sodium-Sulfur Batteries Based on an In Situ Crosslinked Gel Polymer Electrolyte,” *Adv. Funct. Mater.*, vol. 32, no. 32, p. 2201191, 2022, doi: 10.1002/adfm.202201191.

[90] “Construction of Ordered and Fast Lithium Ion Channels in Gel Electrolytes for Li-SPAN Batteries | ACS Applied Materials & Interfaces.” Accessed: Jun. 17, 2025. [Online]. Available: https://pubs.acs.org/doi/full/10.1021/acsami.4c13415

[91] S. Murugan, S. V. Klostermann, W. Frey, J. Kästner, and M. R. Buchmeiser, “A sodium bis(perfluoropinacol) borate-based electrolyte for stable, high-performance room temperature sodium-sulfur batteries based on sulfurized poly(acrylonitrile),” *Electrochem. Commun.*, vol. 132, p. 107137, Nov. 2021, doi: 10.1016/j.elecom.2021.107137.

[92] J. M. Blázquez-Moreno, A. L. Páez Jerez, A. Y. Tesio, A. Benítez, and Á. Caballero, “Stable Long-Term Cycling of Room-Temperature Sodium-Sulfur Batteries Based on Non-Complex Sulfurised Polyacrylonitrile Cathodes,” *Batter. Supercaps*, vol. 8, no. 5, p. e202400640, 2025, doi: 10.1002/batt.202400640.

[93] X. Yu and A. Manthiram, “Room-Temperature Sodium–Sulfur Batteries with Liquid-Phase Sodium Polysulfide Catholytes and Binder-Free Multiwall Carbon Nanotube Fabric Electrodes,” *J. Phys. Chem. C*, vol. 118, no. 40, pp. 22952–22959, Oct. 2014, doi: 10.1021/jp507655u.

[94] H.-L. Wu, L. A. Huff, and A. A. Gewirth, “In Situ Raman Spectroscopy of Sulfur Speciation in Lithium–Sulfur Batteries,” *ACS Appl. Mater. Interfaces*, vol. 7, no. 3, pp. 1709–1719, Jan. 2015, doi: 10.1021/am5072942.

[95] M. Hagen *et al.*, “In-Situ Raman Investigation of Polysulfide Formation in Li-S Cells,” *J. Electrochem. Soc.*, vol. 160, no. 8, p. A1205, May 2013, doi: 10.1149/2.045308jes.

[96] X. Qu *et al.*, “Structural regulations of biomass-derived hard carbon for high-performance sodium-ion batteries,” *J. Power Sources*, vol. 654, p. 237786, Oct. 2025, doi: 10.1016/j.jpowsour.2025.237786.

[97] J. Liu *et al.*, “Formation Mechanism and Molecular Structure of Sulfurized Polyacrylonitrile,” *Adv. Mater.*, vol. 37, no. 29, p. 2503534, 2025, doi: 10.1002/adma.202503534.

[98] K. N. Wood *et al.*, “Dendrites and Pits: Untangling the Complex Behavior of Lithium Metal Anodes through Operando Video Microscopy,” *ACS Cent. Sci.*, vol. 2, no. 11, pp. 790–801, Nov. 2016, doi: 10.1021/acscentsci.6b00260.

[99] G. Li, S. Wang, Y. Zhang, M. Li, Z. Chen, and J. Lu, “Revisiting the Role of Polysulfides in Lithium–Sulfur Batteries,” *Adv. Mater.*, vol. 30, no. 22, p. 1705590, 2018, doi: 10.1002/adma.201705590.

[100] A. N. Mistry and P. P. Mukherjee, “‘Shuttle’ in Polysulfide Shuttle: Friend or Foe?,” *J. Phys. Chem. C*, vol. 122, no. 42, pp. 23845–23851, Oct. 2018, doi: 10.1021/acs.jpcc.8b06077.

[101] A. D. Pathak, E. Cha, and W. Choi, “Towards the commercialization of Li-S battery: From lab to industry,” *Energy Storage Mater.*, vol. 72, p. 103711, Sep. 2024, doi: 10.1016/j.ensm.2024.103711.

[102] L. Yin, J. Wang, F. Lin, J. Yang, and Y. Nuli, “Polyacrylonitrile/graphene composite as a precursor to a sulfur-based cathode material for high-rate rechargeable Li–S batteries,” *Energy Environ. Sci.*, vol. 5, no. 5, pp. 6966–6972, Apr. 2012, doi: 10.1039/C2EE03495F.

[103] Y. He, S. Bi, C. Jiang, and J. Song, “Recent progress of sulfur cathodes and other components for flexible lithium–sulfur batteries,” *Mater. Today Sustain.*, vol. 19, p. 100181, Nov. 2022, doi: 10.1016/j.mtsust.2022.100181.

[104] A. Xu *et al.*, “Unraveling the mechanism on improved kinetics performance of sulfurized polyacrylonitrile with defective conductive carbon matrix,” *Chem. Eng. J.*, vol. 484, p. 149558, Mar. 2024, doi: 10.1016/j.cej.2024.149558.

[105] M. A. Weret *et al.*, “Mechanistic understanding of the Sulfurized-Poly(acrylonitrile) cathode for lithium-sulfur batteries,” *Energy Storage Mater.*, vol. 26, pp. 483–493, Apr. 2020, doi: 10.1016/j.ensm.2019.11.022.

[106] X. Yu and A. Manthiram, “Capacity Enhancement and Discharge Mechanisms of Room-Temperature Sodium–Sulfur Batteries,” *ChemElectroChem*, vol. 1, no. 8, pp. 1275–1280, 2014, doi: 10.1002/celc.201402112.

[107] L. Fang *et al.*, “Suppressing the Shuttle Effects with FeCo/SPAN Cathodes and High-Concentration Electrolytes for High-Performance Lithium–Sulfur Batteries,” *ACS Appl. Energy Mater.*, vol. 6, no. 2, pp. 795–801, Jan. 2023, doi: 10.1021/acsaem.2c03017.

[108] R. Li *et al.*, “Mechanism and Solution of Overcharge Effect in Lithium–Sulfur Batteries,” *Small*, vol. 20, no. 2, p. 2305283, 2024, doi: 10.1002/smll.202305283.

[109] H. Peng *et al.*, “Reducing polarization of lithium-sulfur batteries *via* ZnS/reduced graphene oxide accelerated lithium polysulfide conversion,” *Mater. Today Energy*, vol. 18, p. 100519, Dec. 2020, doi: 10.1016/j.mtener.2020.100519.

[110] Y. Wu *et al.*, “A highly conductive conjugated coordination polymer for fast-charge sodium-ion batteries: reconsidering its structures,” *Chem. Commun.*, vol. 55, no. 73, pp. 10856–10859, Sep. 2019, doi: 10.1039/C9CC05679C.

[111] “Easily Accessible, Textile Fiber-Based Sulfurized Poly(acrylonitrile) as Li/S Cathode Material: Correlating Electrochemical Performance with Morphology and Structure | ACS Energy Letters.” Accessed: Aug. 12, 2025. [Online]. Available: https://pubs.acs.org/doi/10.1021/acsenergylett.7b00009?src=getftr&utm_source=sciencedirect_contenthosting&getft_integrator=sciencedirect_contenthosting

[112] Y. Liu *et al.*, “Sulfur nanocomposite as a positive electrode material for rechargeable potassium–sulfur batteries,” *Chem. Commun.*, vol. 54, no. 18, pp. 2288–2291, Feb. 2018, doi: 10.1039/C7CC09913D.

[113] M. Jiang *et al.*, “Selenium as Extra Binding Site for Sulfur Species in Sulfurized Polyacrylonitrile Cathodes for High Capacity Lithium-Sulfur Batteries,” *ChemElectroChem*, vol. 6, no. 5, pp. 1365–1370, 2019, doi: 10.1002/celc.201801816.

[114] “Metal–Sulfur Battery Cathodes Based on PAN–Sulfur Composites | Journal of the American Chemical Society.” Accessed: Aug. 12, 2025. [Online]. Available: https://pubs.acs.org/doi/10.1021/jacs.5b08113?src=getftr&utm_source=sciencedirect_contenthosting&getft_integrator=sciencedirect_contenthosting

[115] Y. Sun *et al.*, “Functional separator with a lightweight carbon-coating for stable, high-capacity organic lithium batteries,” *Chem. Eng. J.*, vol. 418, p. 129404, Aug. 2021, doi: 10.1016/j.cej.2021.129404.

[116] J. Balach, T. Jaumann, M. Klose, S. Oswald, J. Eckert, and L. Giebeler, “Functional Mesoporous Carbon-Coated Separator for Long-Life, High-Energy Lithium–Sulfur Batteries,” *Adv. Funct. Mater.*, vol. 25, no. 33, pp. 5285–5291, 2015, doi: 10.1002/adfm.201502251.

[117] H. Li *et al.*, “A functional carbon decorated separator for the confinement and redox conversion of lithium polysulfides in high sulfur-loading lithium sulfur batteries,” *Electrochimica Acta*, vol. 469, p. 143276, Nov. 2023, doi: 10.1016/j.electacta.2023.143276.

[118] S. Yao *et al.*, “Enhanced polysulfides conversion with hybrid bipolar membrane composed of CoSe2 and amide-functionalized CNTs composites for lithium sulfur batteries,” *J. Energy Storage*, vol. 78, p. 110087, Feb. 2024, doi: 10.1016/j.est.2023.110087.

[119] J. Feng *et al.*, “A three-dimensional crosslinked chitosan sulfate network binder for high-performance Li–S batteries,” *J. Energy Chem.*, vol. 56, pp. 171–178, May 2021, doi: 10.1016/j.jechem.2020.07.060.

[120] Y.-L. Wan, L. Wang, and L. Wen, “Amide-functionalized organic cationic polymers toward enhanced catalytic performance for conversion of CO2 into cyclic carbonates,” *J. CO2 Util.*, vol. 64, p. 102174, Oct. 2022, doi: 10.1016/j.jcou.2022.102174.

[121] M. S. Rahman, I. M. Al-Marhubi, and A. Al-Mahrouqi, “Measurement of glass transition temperature by mechanical (DMTA), thermal (DSC and MDSC), water diffusion and density methods: A comparison study,” *Chem. Phys. Lett.*, vol. 440, no. 4, pp. 372–377, Jun. 2007, doi: 10.1016/j.cplett.2007.04.067.

[122] L. Han, K. Zhang, H. Ishida, and P. Froimowicz, “Study of the Effects of Intramolecular and Intermolecular Hydrogen-Bonding Systems on the Polymerization of Amide-Containing Benzoxazines,” *Macromol. Chem. Phys.*, vol. 218, no. 18, p. 1600562, 2017, doi: 10.1002/macp.201600562.

[123] N. Soszka *et al.*, “The impact of the length of alkyl chain on the behavior of benzyl alcohol homologues – the interplay between dispersive and hydrogen bond interactions,”

*Phys. Chem. Chem. Phys.*, vol. 23, no. 41, pp. 23796–23807, Oct. 2021, doi: 10.1039/D1CP02802B.

[124] Z.-C. Su, S.-J. Lin, Y.-H. Chang, W.-L. Yeh, and I.-M. Chu, "Synthesis, characterization, and cytotoxicity of PCL–PEG–PCL diacrylate and agarose interpenetrating network hydrogels for cartilage tissue engineering," *J. Appl. Polym. Sci.*, vol. 137, no. 45, p. 49409, 2020, doi: 10.1002/app.49409.

[125] B. Dhandayuthapani, R. Mallampati, D. Sriramulu, R. F. Dsouza, and S. Valiyaveettil, "PVA/Gluten Hybrid Nanofibers for Removal of Nanoparticles from Water," *ACS Sustain. Chem. Eng.*, vol. 2, no. 4, pp. 1014–1021, Apr. 2014, doi: 10.1021/sc500003k.

[126] M. S. Demyan, F. Rasche, E. Schulz, M. Breulmann, T. Müller, and G. Cadisch, "Use of specific peaks obtained by diffuse reflectance Fourier transform mid-infrared spectroscopy to study the composition of organic matter in a Haplic Chernozem," *Eur. J. Soil Sci.*, vol. 63, no. 2, pp. 189–199, 2012, doi: 10.1111/j.1365-2389.2011.01420.x.

[127] J. W. Mitchell and A. Addagada, "Chemistry of proton track registration in cellulose nitrate polymers," *Radiat. Phys. Chem.*, vol. 76, no. 4, pp. 691–698, Apr. 2007, doi: 10.1016/j.radphyschem.2006.05.012.

[128] P. Ghasemiahangarani, G. Farhan, D. del Mundo, and T. Schoetz, "Charge Storage Mechanisms in Batteries and Capacitors: A Perspective of the Electrochemical Interface," *Adv. Energy Mater.*, vol. 15, no. 12, p. 2404704, 2025, doi: 10.1002/aenm.202404704.

[129] J. Wu *et al.*, "Ultralight Layer-by-Layer Self-Assembled MoS2-Polymer Modified Separator for Simultaneously Trapping Polysulfides and Suppressing Lithium Dendrites," *Adv. Energy Mater.*, vol. 8, no. 35, p. 1802430, 2018, doi: 10.1002/aenm.201802430.

[130] Y. C. Jeong *et al.*, "Rational design of exfoliated 1T MoS2@CNT-based bifunctional separators for lithium sulfur batteries," *J. Mater. Chem. A*, vol. 5, no. 45, pp. 23909–23918, Nov. 2017, doi: 10.1039/C7TA08153G.

[131] J. Wu *et al.*, “Fast electrochemical kinetics and strong polysulfide adsorption by a highly oriented MoS2 nanosheet@N-doped carbon interlayer for lithium–sulfur batteries,” *J. Mater. Chem. A*, vol. 7, no. 13, pp. 7897–7906, Mar. 2019, doi: 10.1039/C9TA00458K.

[132] P. Cao *et al.*, “Tuning the Composition and Structure of Amorphous Molybdenum Sulfide/Carbon Black Nanocomposites by Radiation Technique for Highly Efficient Hydrogen Evolution,” *Sci. Rep.*, vol. 7, no. 1, p. 16048, Nov. 2017, doi: 10.1038/s41598-017-16015-y.

[133] “Surface-enhanced redox chemistry of polysulphides on a metallic and polar host for lithium-sulphur batteries | Nature Communications.” Accessed: Apr. 15, 2025. [Online]. Available: https://www.nature.com/articles/ncomms5759?utm_medium=apac_metadata&utm_source=xmol&utm_campaign=CONR_JRNLS_AWA1_CN_CNPL_00AX4_JXMOL

[134] D. S. Wu *et al.*, “Quantitative investigation of polysulfide adsorption capability of candidate materials for Li-S batteries,” *Energy Storage Mater.*, vol. 13, pp. 241–246, Jul. 2018, doi: 10.1016/j.ensm.2018.01.020.

[135] Y. Li *et al.*, “Covalent Coupled Sulfur-Deficient MoS2 Nanosheets on Carbon Nanotubes toward Polysulfide Catalytic Conversion in a Lithium Sulfur Battery,” *ACS Sustain. Chem. Eng.*, vol. 11, no. 3, pp. 1019–1026, Jan. 2023, doi: 10.1021/acssuschemeng.2c05699.

[136] Z. A. Ghazi *et al.*, “MoS2/Celgard Separator as Efficient Polysulfide Barrier for Long-Life Lithium–Sulfur Batteries,” *Adv. Mater.*, vol. 29, no. 21, p. 1606817, 2017, doi: 10.1002/adma.201606817.

[137] S. Liu, Z. Zhou, and D. Liu, “MoS2 coated separator as an efficient barrier for inhibiting shuttle effect of polysulfide,” *Ceram. Int.*, vol. 45, no. 11, pp. 14415–14419, Aug. 2019, doi: 10.1016/j.ceramint.2019.04.160.

[138] A. C. Pundir and A. Sil, “Synergetic effect of 2D-MoS2 nanoflakes functionalised separator supported by hierarchical porous carbon/sulfur nanoparticle composite cathode for improved polysulfide conversion in Li-S battery,” *J. Energy Storage*, vol. 112, p. 115594, Mar. 2025, doi: 10.1016/j.est.2025.115594.

[139] M. Gaberšček, “Understanding Li-based battery materials via electrochemical impedance spectroscopy,” *Nat. Commun.*, vol. 12, no. 1, p. 6513, Nov. 2021, doi: 10.1038/s41467-021-26894-5.

[140] J.-A. Choi, S. H. Kim, and D.-W. Kim, “Enhancement of thermal stability and cycling performance in lithium-ion cells through the use of ceramic-coated separators,” *J. Power Sources*, vol. 195, no. 18, pp. 6192–6196, Sep. 2010, doi: 10.1016/j.jpowsour.2009.11.020.

[141] S. Xia, Y. Huang, J. Tang, and L. Wang, “Preparation of various thiol-functionalized carbon-based materials for enhanced removal of mercury from aqueous solution,” *Environ. Sci. Pollut. Res.*, vol. 26, no. 9, pp. 8709–8720, Mar. 2019, doi: 10.1007/s11356-019-04320-0.

[142] “Direct-Laser-Writing of Metal Sulfide-Graphene Nanocomposite Photoelectrode toward Sensitive Photoelectrochemical Sensing - Ge - 2019 - Advanced Functional Materials - Wiley Online Library.” Accessed: Sep. 15, 2025. [Online]. Available: https://advanced.onlinelibrary.wiley.com/doi/10.1002/adfm.201904000

[143] C. Varodi *et al.*, “Nitrogen and Sulfur Co-Doped Graphene as Efficient Electrode Material for L-Cysteine Detection,” *Chemosensors*, vol. 9, no. 6, p. 146, Jun. 2021, doi: 10.3390/chemosensors9060146.

[144] X. Wang *et al.*, “Nitrogen Defects and Interfacial Chemical Bonds in Fe Single-Site Mediated C3N4 With Rod-Like Fe2O3 Enhanced the S-Scheme Heterojunction for Efficient Energy Conversion,” *Adv. Funct. Mater.*, vol. n/a, no. n/a, p. 2421847, doi: 10.1002/adfm.202421847.

[145] L. Su, P. Wang, X. Ma, J. Wang, and S. Zhan, “Regulating Local Electron Density of Iron Single Sites by Introducing Nitrogen Vacancies for Efficient Photo-Fenton Process,” *Angew. Chem. Int. Ed.*, vol. 60, no. 39, pp. 21261–21266, 2021, doi: 10.1002/anie.202108937.

[146] R. Elazari, G. Salitra, A. Garsuch, A. Panchenko, and D. Aurbach, “Sulfur-Impregnated Activated Carbon Fiber Cloth as a Binder-Free Cathode for Rechargeable Li-S Batteries,” *Adv. Mater.*, vol. 23, no. 47, pp. 5641–5644, 2011, doi: 10.1002/adma.201103274.

[147] L. Ji, M. Rao, S. Aloni, L. Wang, E. J. Cairns, and Y. Zhang, “Porous carbon nanofiber–sulfur composite electrodes for lithium/sulfur cells,” *Energy Environ. Sci.*, vol. 4, no. 12, pp. 5053–5059, Nov. 2011, doi: 10.1039/C1EE02256C.

[148] Y.-T. Weng *et al.*, “Efficient synthesis of high-sulfur-content cathodes for high-performance Li–S batteries based on solvothermal polysulfide chemistry,” *J. Power Sources*, vol. 450, p. 227676, Feb. 2020, doi: 10.1016/j.jpowsour.2019.227676.

[149] Z. Yan, L. Zhao, Y. Wang, Z. Zhu, and S.-L. Chou, “The Future for Room-Temperature Sodium–Sulfur Batteries: From Persisting Issues to Promising Solutions and Practical Applications,” *Adv. Funct. Mater.*, vol. 32, no. 36, p. 2205622, 2022, doi: 10.1002/adfm.202205622.

[150] Y. Liu *et al.*, “Recent Advances in Transition-Metal-Based Catalytic Material for Room-Temperature Sodium–Sulfur Batteries,” *Adv. Funct. Mater.*, vol. 34, no. 5, p. 2302626, 2024, doi: 10.1002/adfm.202302626.

[151] E. L. Gray, J.-I. Lee, Z. Li, J. Moloney, Z. J. Yang, and M. Chhowalla, “Mapping Polysulfides in Sodium–Sulfur Batteries,” *ACS Nano*, vol. 19, no. 9, pp. 8939–8947, Mar. 2025, doi: 10.1021/acsnano.4c16941.

[152] “Optical Microscopy Reveals the Ambient Sodium–Sulfur Discharge Mechanism | ACS Sustainable Chemistry & Engineering.” Accessed: Sep. 18, 2025. [Online]. Available: https://pubs.acs.org/doi/10.1021/acssuschemeng.0c07180

[153] X. Ji, K. T. Lee, and L. F. Nazar, “A highly ordered nanostructured carbon–sulphur cathode for lithium–sulphur batteries,” *Nat. Mater.*, vol. 8, no. 6, pp. 500–506, Jun. 2009, doi: 10.1038/nmat2460.

[154] H. Al Salem, G. Babu, C. V. Rao, and L. M. R. Arava, “Electrocatalytic Polysulfide Traps for Controlling Redox Shuttle Process of Li–S Batteries,” *J. Am. Chem. Soc.*, vol. 137, no. 36, pp. 11542–11545, Sep. 2015, doi: 10.1021/jacs.5b04472.

[155] T. Zhao *et al.*, “Modifying Separators with a Multistrategy-Constructed (ZnCo)3S4–MoS2 Heterostructure for High-Performance Lithium–Sulfur Batteries,” *ACS Appl. Nano Mater.*, vol. 8, no. 16, pp. 8220–8230, Apr. 2025, doi: 10.1021/acsanm.5c00747.

[156] J. Cho *et al.*, “Nitrogen-doped MoS2 as a catalytic sulfur host for lithium-sulfur batteries,” *Chem. Eng. J.*, vol. 439, p. 135568, Jul. 2022, doi: 10.1016/j.cej.2022.135568.

[157] D. R. Lobato-Peralta, M. J. Lázaro, and C. Alegre, “Carbon-based materials in metal-ion hybrid supercapacitors: Advances, challenges, and future directions,” *J. Energy Storage*, vol. 131, p. 117568, Sep. 2025, doi: 10.1016/j.est.2025.117568.

# Publication

**Publication during PhD study:**

[1] Liwen Yang, Angelina Sarapulova, Bercis Pektas, Rong Li, Hatice Mutlu, Sonia Dsoke. Depth-of-Discharge-Dependent Chemical Evolution in Sulfurized Polyacrylonitrile Cathodes for Ether-Based Room-Temperature Sodium–Sulfur Batteries (Accepted by ***Advanced Energy Materials***)

[2] Liwen Yang, Bercis Pektas, Samar Hajjar-Garreau, Angelina Sarapulova, Hatice Mutlu, Sonia Dsoke. Failure Mechanisms of Nitrogen-Rich Sulfurized Polyamides as Cathodes for Room-Temperature Na-S Batteries (Prepared for submission)

# Declaration

Die vorliegende Arbeit wurde im Zeitraum vom Oktober 2022 bis Oktober 2026 am Institut für am Institut für Angewandte Materialien und der Anorganischen Chemie der Fakultät für Chemie und Biowissenschaften am Karlsruher Institut für Technologie (KIT) unter der Leitung von Prof. Dr. Helmut Ehrenberg angefertigt.

Hiermit versichere ich, die vorliegende Arbeit selbstständig verfasst und keine anderen als die angegebenen Quellen und Hilfsmittel verwendet sowie Zitate kenntlich gemacht zu haben. Die Dissertation wurde bisher an keiner anderen Hochschule oder Universität eingereicht.

M. Sc. Liwen Yang